A Study of Localized Momentum Forcing in the Thermosphere

Steven Wayne Lehr

AFIT Student Attending: University of Michigan   AFIT/CI/CIA- 90-130

AFIT/CI
Wright-Patterson AFB OH 45433-6583

DTIC
ELECTE
FEB 0 7 1991
S B D

101
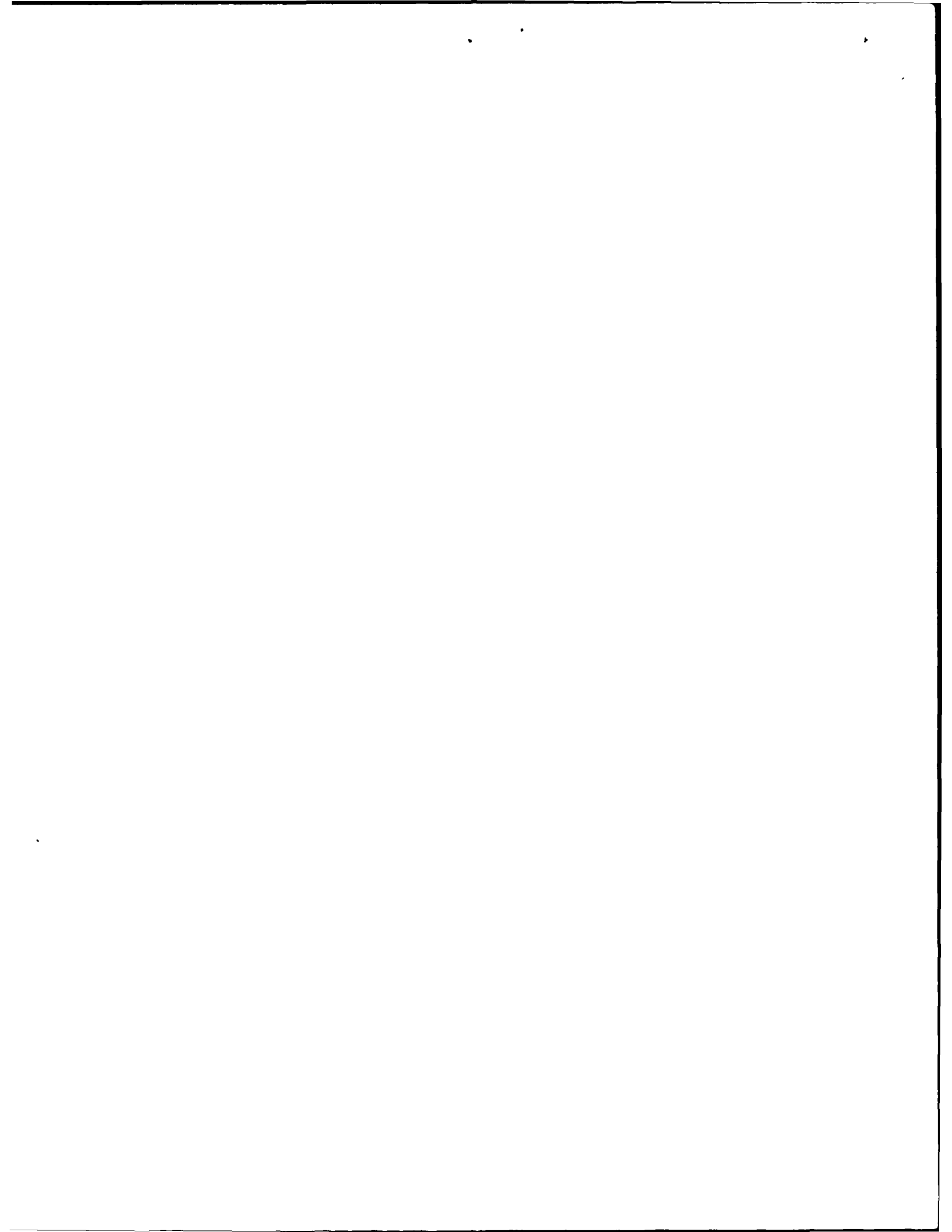
A STUDY OF LOCALIZED MOMENTUM FORCING IN THE THERMOSPHERE

by

Steven Wayne Lehr

A thesis submitted in partial fulfillment
of the requirements for the degree of
Master of Science
(Atmosphere and Space Sciences)
in The University of Michigan

Advisor:

Associate Professor, Timothy L. Killeen

Abstract

The response of the neutral atmosphere to momentum forcing at F-region heights (about 400 km) is investigated. The appropriate form of the momentum equation as it pertains to the observed local acceleration of the wind at a specified location is developed. Experiments were performed using data generated by a National Center for Atmospheric Research (NCAR) thermospheric general circulation model (TGCM) The acceleration of the neutral wind at several locations and times were compared with the sum of the forcing terms of the momentum equation. The appropriate forms of the equation for stationary as well as moving observers were used, the latter being applied to satellites orbiting at thermospheric altitudes. The momentum equation was analyzed to determine which forces could be calculated solely from the data typically gathered by the Dynamics Explorer (DE-2) satellite Both synthesized and actual satellite data were used in the various experiments.

Techniques and software were developed to assist in the data handling and subsequent analysis. The results ranged from excellent agreement between the observed acceleration and total forcing for the case of a fixed observer when archived TGCM data was used, to virtually no correlation between measured momentum forcing and observed acceleration in the case of the satellite-borne measurements. It was found that the best results were obtained when the effect of ion drag on the neutral wind was at a minimum. This occurred during the evening hours (when ion densities were lowest) and at low latitudes (away from polar electric fields). A detailed analysis on measurement uncertainty and its potential effect on the results is also presented.

Table of Contents

Table of Contents - (continued)

Acknowledgements

I would first like to thank my loving wife, Becky, for her never-ending support in this venture of mine. I doubt that I would have been able to get it done in the required time if not for her encouragement and those many "double-sized" lunches she packed for me every day.

A great deal of thanks is of course due to my advisor, Dr Tim Killeen. His reputation of demanding the best work out of his graduate students is certainly well deserved and presented a formidable challenge. I would do well to emulate this standard of excellence in all my future endeavors.

Many thanks also goes to Dr Alan Burns, who gave me many hours of his valuable time to provide me with the model data that was so crucial to my research.

The United States Air Force should not be left out of this thank you list, since this organization provided me the opportunity to obtain this graduate degree. I extend my personal thanks to every American taxpayer who helped put me through graduate school. I will make it a priority of mine to see that your tax dollars are not wasted.

Chapter 1 Introduction

1.1 Statement of Problem

The objective of this thesis is to study the response of the neutral thermosphere to momentum forcing inputs and verfy that the measured response is consistent with the momentum equation.

To accomplish this object I have made extensive use of the output of a thermospheric general circulation model (TGCM) to simulate the evolution of the neutral winds at thermospheric heights. This data has been examined extensively, and detailed comparisons were made between the forces acting at specific locations and the observed accelerations at those locations.

1.2 Thesis Format

This thesis consists of five chapters and four appendices. Chapter 2 is a brief review of the momentum equation as it pertains to the thermosphere. The lagrangian and eularian forms of the momentum equation are presented as is the application of the latter form to the present problem. The ion drag and viscous drag terms are described as being the respective major and minor driving forces in this atmospheric region.

Chapter 3 describes the major tools that were used for this study. The TGCM and VSH models are briefly described and several examples of their output are presented. The working data base from which the majority of the computations was made is also described here. Finally, a description of the Dynamics Explorer (DE) on line data base at the University of Michigan is presented along with some information as to how it was specifically applied.

The main core of the work is presented in chapter 4. It is in this chapter where the momentum equation is broken down into its component parts and detailed comparisons between the forcing and acceleration are made. The process begins by looking at archived TGCM output and comparing the acceleration of the neutral wind to the sum total of all the forces acting at one specific location over a 24 hour period. Next, the same analysis is performed for this and other locations using the data from the working data base. Following the fixed location study the same sort of analysis was performed for the case of -

1

a simulated polar orbiting satellite. The chapter ends with a study of thermospheric forcing based on observerations made by a polar orbiting satellite using actual data from the DE data base. Results and conclusions are presented in chapter 5.

The appendices contain useful information that was not necessarily appropriate for inclusion in the main body. Appendix A is a detailed look at the concept of the total derivative and its applicability to the present problem. As a thorough understanding of this concept is crucial to this study, I would strongly recommend reading Appendix A before beginning chapter 2. Appendix B contains the techniques and formulas used to compute the uncertainties in the various computations. Appendices C and D contain tables and graphs of the simulated and actual satellite data that, though important for computational purposes, was not crucial for the discussion in the main body of the thesis.

Chapter 2 The Momentum Equation

The evolution of the motion of any portion of the atmosphere is ultimately governed by the fundamental equations of motion. For any individual control volume (or parcel) of air the motion can be described by the following equation as presented by *Holton* [1979]:

$$\frac{d\mathbf{U}}{dt} = -2\,\Omega \times \mathbf{U} - \frac{1}{\rho}\nabla P + \mathbf{g} + \mathbf{F}_r \qquad (2\text{-}1)$$

In the above expression the term on the left hand side is the acceleration of the control volume following the motion of the fluid (the airstream in this case). The first term on the right hand side is the Coriolis force that arises because of the accelerated nature of the earth's rotating reference frame. The second term on the right is the pressure gradient force common to all fluid motions. The third term is the acceleration due to gravity and always acts downward (toward the origin in an earth-centered coordinate system). The last term on the right hand side ($\mathbf{F}_r$) is the sum of forces due to friction with adjacent flows. It is expressed in generic form here because its specific form is unique to the portion of the atmosphere under consideration. The form of this term appropriate for this study will be discussed shortly. During this study we consider the two-dimensional form of the momentum equation (2-1) for neutral species. Thus, the eastward (u) and northward (v) horizontal components of the neutral wind will alone be considered; so the **g** term in (2-1) does not come into play.

The coordinate system used in this study is the one most commonly used to describe locations and motions in the geocentered system; namely, the spherical coordinate system. The form of (2-1) appropriate for a rotating spherical coordinate system is presented by *Holton* [1979]as follows:

$$\frac{d\mathbf{U}}{dt} = \left(\frac{du}{dt} - \frac{uv\,\tan\phi}{r}\right)\mathbf{i} + \left(\frac{dv}{dt} + \frac{u^2\tan\phi}{r}\right)\mathbf{j} \qquad (2\text{-}2)$$

where: ϕ = latitude

λ = longitude (below)

r = radius of earth plus altitude

du/dt = instantaneous zonal acceleration

dv/dt = instantaneous meridional acceleration

The curvature terms in (2-2) arise because of the positional dependence of the unit vectors **i** and **j**. The individual component momentum equations then become:

$$\frac{du}{dt} = - \frac{1}{\rho r \cos \phi} \frac{\partial P}{\partial \lambda} + fv + F_x + \frac{uv \tan \phi}{r} \qquad (2\text{-}3a)$$

$$\frac{dv}{dt} = - \frac{1}{\rho r} \frac{\partial P}{\partial \phi} - fu + F_y - \frac{u^2 \tan \phi}{r} \qquad (2\text{-}3b)$$

2.1 Thermospheric Form of the Momentum Equation

The form of the momentum equation for the region of interest (ionospheric F-Layer) is found by substituting the appropriate frictional forces into (2-2). These frictional forces include the viscous drag force and the ion drag force.

2.1.1 Viscous Drag Force

The viscous force is due to the action of vertical diffusion in the presence of vertical velocity shears. The expression describing the magnitude of the viscous drag force is also described by *Holton*:

$$F_x = \frac{\eta}{\rho} \frac{\partial^2 u}{\partial z^2} \qquad (2\text{-}4a)$$

$$F_y = \frac{\eta}{\rho} \frac{\partial^2 v}{\partial z^2} \qquad (2\text{-}4b)$$

where: η = coefficient of dynamic viscosity

ρ = mass density of neutral atmosphere

In the above expression the η term is a slowly varying function of temperature, while the mass density varies significantly with altitude. The ratio η/ρ is often called the kinematic viscosity, and also has a marked altitude dependence. Thus, we would expect the viscous drag to work efficiently at the F-region altitudes. Ironically, this efficiency quickly removes the second derivative in the velocity profiles and subsequently reduces the magnitude of the viscous drag force. As a result the viscous drag force has a relatively

4

minor role in the horizontal momentum equation. The next chapter quantitatively compares the viscous drag with the other terms.

2.1.2 Ion Drag Force

The F-region of the ionosphere contains a high density of positively charged ions mostly in the form of singly ionized atomic oxygen. Because of the net charge on the ions they can be accelerated in the presence of electric fields. This acceleration is completely independent of the motion of the surrounding neutral gas, and a velocity shear between the two constituents is almost always present. As ions collide with the neutral particles a frictional drag force is imparted to the neutrals according to the following:

$$ID_x = \bar{V}_{ni}(u_i - u_n) = \bar{V}_{in}(u_i - u_n)\frac{n_i}{n_n} \tag{2-5a}$$

$$ID_y = \bar{V}_{ni}(v_i - v_n) = \bar{V}_{in}(v_i - v_n)\frac{n_i}{n_n} \tag{2-5b}$$

As can be seen from (2-5) the magnitude of the ion drag force depends not only on the velocity shear, but on the relative density between the ions and neutrals as well. This fact creates a local time dependence in the ion drag as the ion population goes through a pronounced diurnal variation. The momentum transfer collision frequency can be computed, and the techniques for doing so are included in Appendix B. As we will see in the next section, the ion drag force is a major player in determining the neutral gas circulation.

2.2 Momentum Equation in Eulerian Form

Upon substituting the viscous and ion drag forces into (2-3) the momentum equations following the motion of the air (the so-called *lagrangian* form) become:

$$\frac{du}{dt} = -\frac{1}{\rho r \cos\phi}\frac{\partial P}{\partial \lambda} + fv + \frac{\eta}{\rho}\frac{\partial^2 u}{\partial z^2} + \bar{V}_{ni}(u_i - u_n) + \frac{uv\tan\phi}{r} \tag{2-6a}$$

$$\frac{dv}{dt} = -\frac{1}{\rho r}\frac{\partial P}{\partial \phi} - fu + \frac{\eta}{\rho}\frac{\partial^2 v}{\partial z^2} + \bar{V}_{ni}(v_i - v_n) - \frac{u^2\tan\phi}{r} \tag{2-6b}$$

An alternative to the lagrangian form above is the *eulerian* representation, which relates accelerations following the motion to those observed at a fixed location as follows:

$$\frac{dQ}{dt} = \frac{\partial Q}{\partial t} + \mathbf{V} \cdot \nabla Q \tag{2-7}$$

5

Using this expression for the total derivative we can express the momentum equations in the following eulerian form:

$$\frac{\partial u}{\partial t} = -\frac{1}{\rho r \cos\phi}\frac{\partial P}{\partial \lambda} + fv + \frac{\eta}{\rho}\frac{\partial^2 u}{\partial z^2} + \bar{\nu}_{ni}(u_i - u_n) + \frac{uv\tan\phi}{r} - \mathbf{V}\cdot\nabla u \qquad (2\text{-}8a)$$

$$\frac{\partial v}{\partial t} = -\frac{1}{\rho r}\frac{\partial P}{\partial \phi} - fu + \frac{\eta}{\rho}\frac{\partial^2 v}{\partial z^2} + \bar{\nu}_{ni}(v_i - v_n) - \frac{u^2\tan\phi}{r} - \mathbf{V}\cdot\nabla v \qquad (2\text{-}8b)$$

We will make extensive use of this form of the momentum equation both in the case of a fixed observer and in the case of an observational platform that is moving with respect to the established coordinate system (ie an orbiting satellite). A complete development of the physical meaning of the total derivative and how it relates to stationary as well as moving observers is presented in Appendix A.

As it stands the momentum equation gives a complete description of the forces acting at a specified location, but it gives no information as to which of the forcing terms are the most significant. Figure 2.1 is a stacked breakdown of the individual forcing terms during a 24 hour period at location (47.5, 0). From this figure one can see that the pressure gradient and the ion drag are clearly the most important contributors to the local forcing. The forces depicted on the diagram were computed using a thermospheric general circulation model described in the next chapter.
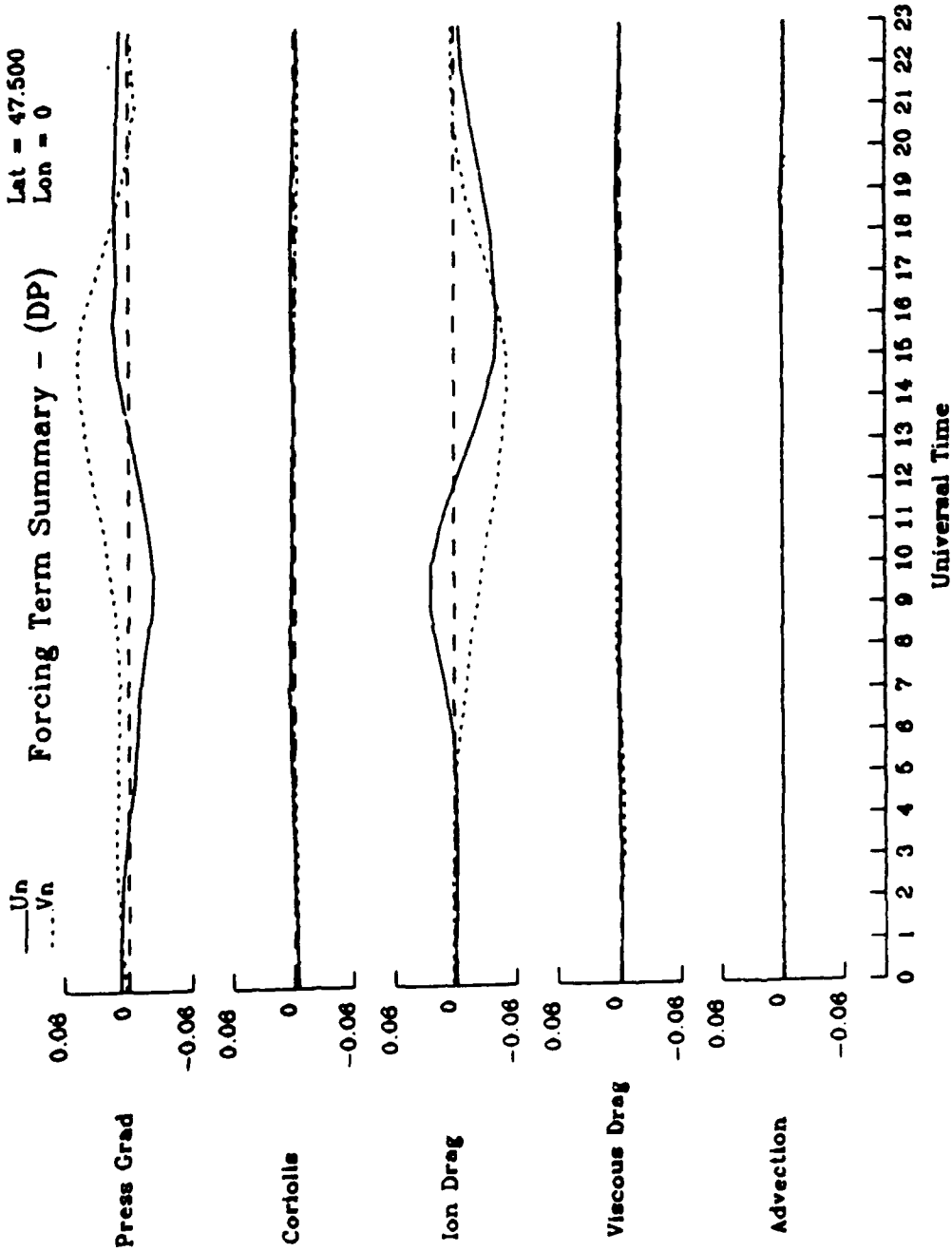
Figure 2.1 Stack plot comparison of the momentum equation forcing terms at the specified location. Forces were computed by the TGCM and diagnostics processor.

Chapter 3   Tools used for this Study

This study was largely computer based, both in the area of modeling and in data retrieval and analysis. The modeling was accomplished primarily with the National Center for Atmospheric Research (NCAR) thermospheric general circulation model (TGCM). The TGCM and its diagnostics processor was used to build a large working data base from which momentum forcing calculations could be made. In addition to the TGCM a vector spherical harmonic (VSH) decomposition model was used to supplement TGCM data. Finally, a large data base of actual measurements from the Dynamics Explorer 2 (DE-2) was available and used for comparative study. This chapter briefly summarizes the models and the content of the working data base.

3.1   Thermospheric General Circulation Model (TGCM)

The momentum forcing aspects of the TGCM as well as a description of the diagnostics processor.is discussed by *Killeen and Roble* [1984]. This model si nultaneously solves the continuity, momentum, and energy equations to compute the wind, temperature, and composition for all model grid points at each hour of universal time. The grid is defined horizontally by the 5 degree latitude and longitude points and vertically by 24 constant-pressure surfaces with 1/2 scale height separation. The model can accept several geophysical parameters as input and is thus very useful for studying the evolution of the thermosphere under a variety of conditions. The model is typically run until a steady state is reached and a diurnally reproducible history file is created. The history file used in this study was created using the following geophysical parameters as inputs:

Hemispheric power:	11 GW
Cross Cap Potential:	60 kV
F10.7:	243
Equivalent Day:	79355

The diagnostics processor was developed to provide a means for making detailed analysis of the individual forcing terms of momentum equation for each location and at each universal time. The processor reads the TGCM history file as its primary input, but also accepts some of the same inputs that were used in the model run. Earlier TGCM versions [*Dickinson, et al.*, 1981] include (among other things) the ion drag tensors used to compute the ion drag force. Later versions of the model (including the one used here) computed the ion drag tensors within the code itself. The processor was run on the history file described above to create the working data base.

3.2 The Working Data Base

For each horizontal grid point the working data base initially included the neutral and ion winds, neutral and ion temperatures, neutral and electron densities, height of the pressure level, ion drag tensors, and the mass mixing ratios of molecular and atomic oxygen. Later the individual forcing terms were also added, which includes the ion drag, pressure gradient, Coriolis, viscous drag, the momentum advection, and the sum total of the individuals. Only one pressure level (Z=2) was considered for this study, the pressure levels being defined by the following simple expression:

$$Z = \log_e(P_0/P) \qquad (3\text{-}1)$$

where P_0 is equal to the reference pressure of 50 μPa. From this expression we see that integral values of Z are separated by a factor or $1/e$ (ie one scale height). The altitude of the Z=2 pressure level was approximately 375 km for this study. Even though only one pressure level was considered, the volume of the retrieved data all but filled all allocated disk storage space. To make a more manageable working data base, only the grid points corresponding to latitudes greater than or equal 37.5 degrees (north) were retained for this study. The intact data base was transferred to magnetic tape for future availability.

Each variable in the data base was contained in its own data file and each had identical file structure. The files were dimensioned according to longitude (73), latitude (11), and universal time (24). Thus U_n (0, 0, 0) corresponds to the zonal neutral wind component at ±180 degree longitude, 37.5 degree latitude, and 0 UT. Each data file thus contained 19,272 data points.

The data analysis and plotting was accomplished almost exclusively by the IDL utility. Figures 3.1 through 3.7 display polar plots of the neutral and ion winds and the forcing terms for 0, 6, 12, and 18 UT. The relative contributions of each of the forces is apparent by inspection from these figures. As was the case in figure 2.1, the ion drag and

9

pressure gradient forces are clearly the most important, while the viscous drag is of lesser significance.

3.3 The VSH Model

The VSH model [*Killeen, et al.*, 1987] was developed to provide a more "portable" version of the TGCM. The VSH is essentially a decomposition of the history file of a specific TGCM run. It breaks the history file down into a set of spherical harmonic coefficients. These coefficients can then be applied to the appropriate polynomial expansion to return the value of the desired data. There are two features of the VSH which make it especially attractive to this study. First and foremost is the fact that it is extremely easy to use, as one need only specify a short set of parameters in a FORTRAN subroutine call statement. The parameters include the latitude, longitude, altitude, time, and other geophysical parameters. This flexibility gives the VSH its second attractive feature, as it makes it very easy to interpolate between the grid points (both spatial and temporal). Thus, simulations involving a satellite orbiting the earth in virtually any orbit are very easy to perform. The output of the VSH includes many (but not yet all) of the outputs of the TGCM. A polar plot of the neutral wind as computed by the VSH (including a short list of the geophysical parameters used as input).is shown in figure 3.8. The inputs were chosen to duplicate the working data base as closely as possible. A comparison of this figure to figure 3.1 shows that the VSH output is acceptably close to the original TGCM data.

3.5 Dynamics Explorer (DE-2) Data Base

The SPRL library at the University of Michigan contains an on-line data base of DE-2 measurements for over 8,000 orbits of the satellite. The variety of data available is summarized in the examples contained in Appendix D. The data coverage is far from being continuous, since much of the data was measured *in situ* and could be only be taken during the perigee of the orbit. In addition, not all the satellite's instruments were activated at all times. It is quite often the case that a particular measurement for a specific location at a specific time is not available. To facilitate orbit selection there is an on-line catalog available which lists the instrument status for each orbit. For this particular study, the only real orbit selection criteria were that the satellite provide continuous coverage for the same latitude band on three consecutive orbits. Despite this apparently lean specification requirement, the data base could provide only one set of three such orbits.

The availability of the DE data base makes possible direct comparisons of model output to satellite observations. Figure 3.9 displays the neutral winds along two segments of DE orbit 7217 along with simulated TGCM output. The satellite's parameterized orbit

10

was used as an input to the model along with two different levels of geomagnetic activity. As is evident from the figure, the model outputs using the storm level inputs show generally good agreement with the satellite data. Thus we can be reasonably assured that the TGCM provides a realistic picture of the evolving atmosphere.

TIGCM Neutral Winds
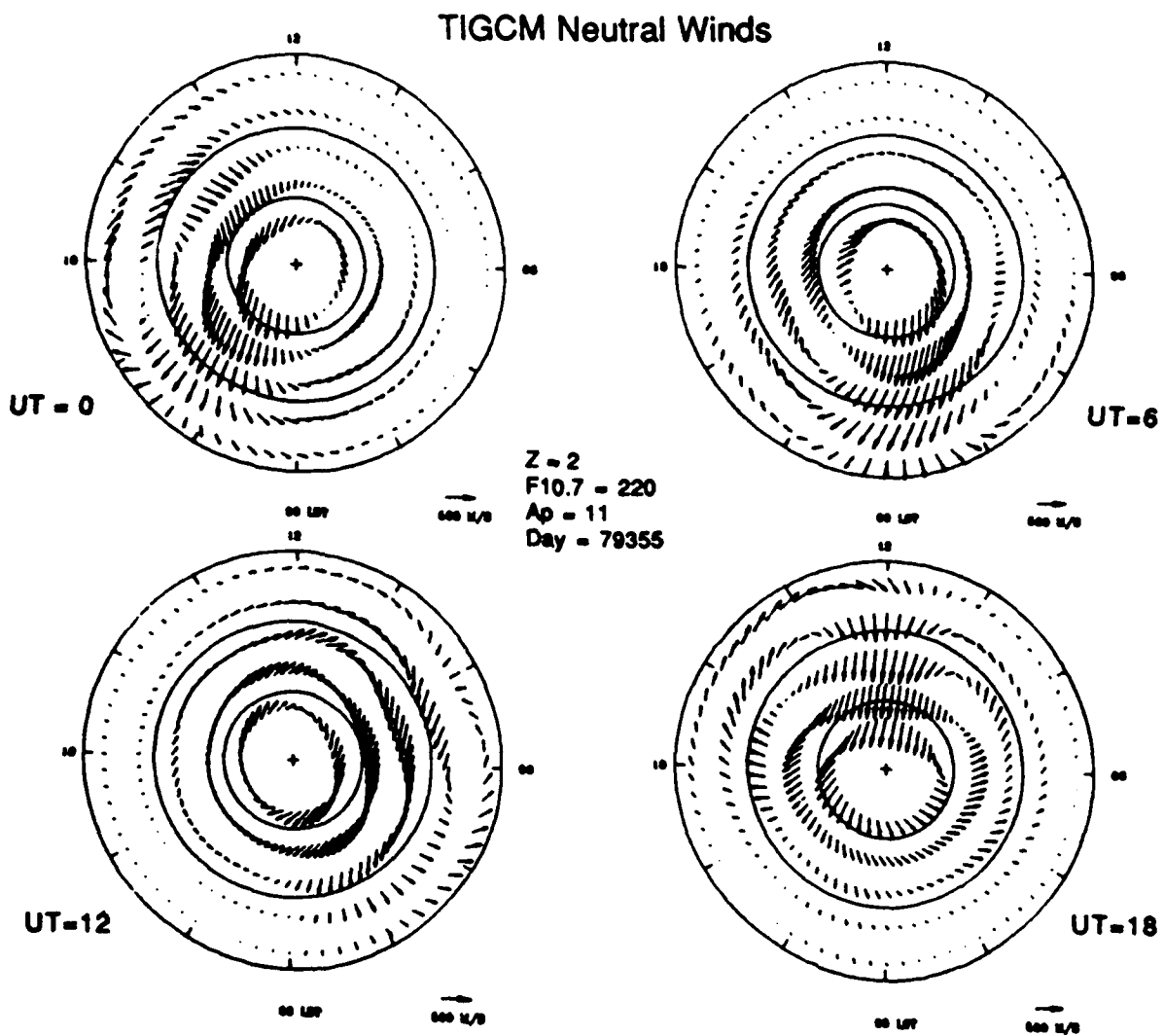
Figure 3.1 Polar dial plot of TGCM produced neutral winds for the four times shown. Geophysical parameters for model input are also shown.

Ion Wind

0 UT

12

18   06

00 LST   ⟶
          1100.3 m/s

6 UT

12

18   06

00 LST   ⟶
          1110.3 m/s

12 UT

18

18   06

00 LST   ⟶
          1100.8 m/s

18 UT

12

18   06

00 LST   ⟶
          1100.8 m/s
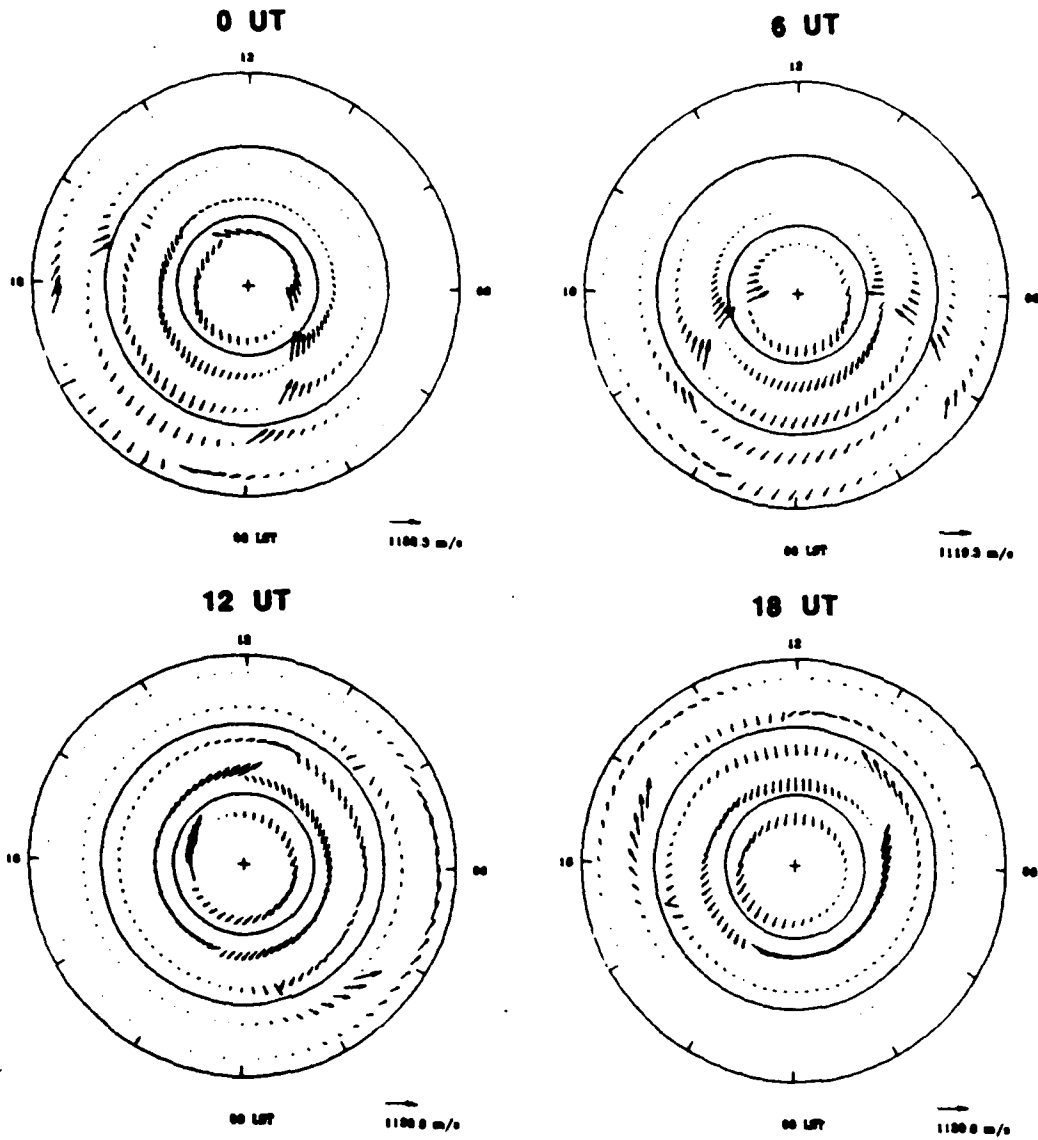
Figure 3.2 Polar dial plot of the TGCM ion drift velocities at the four indicated times.

Ion Drag
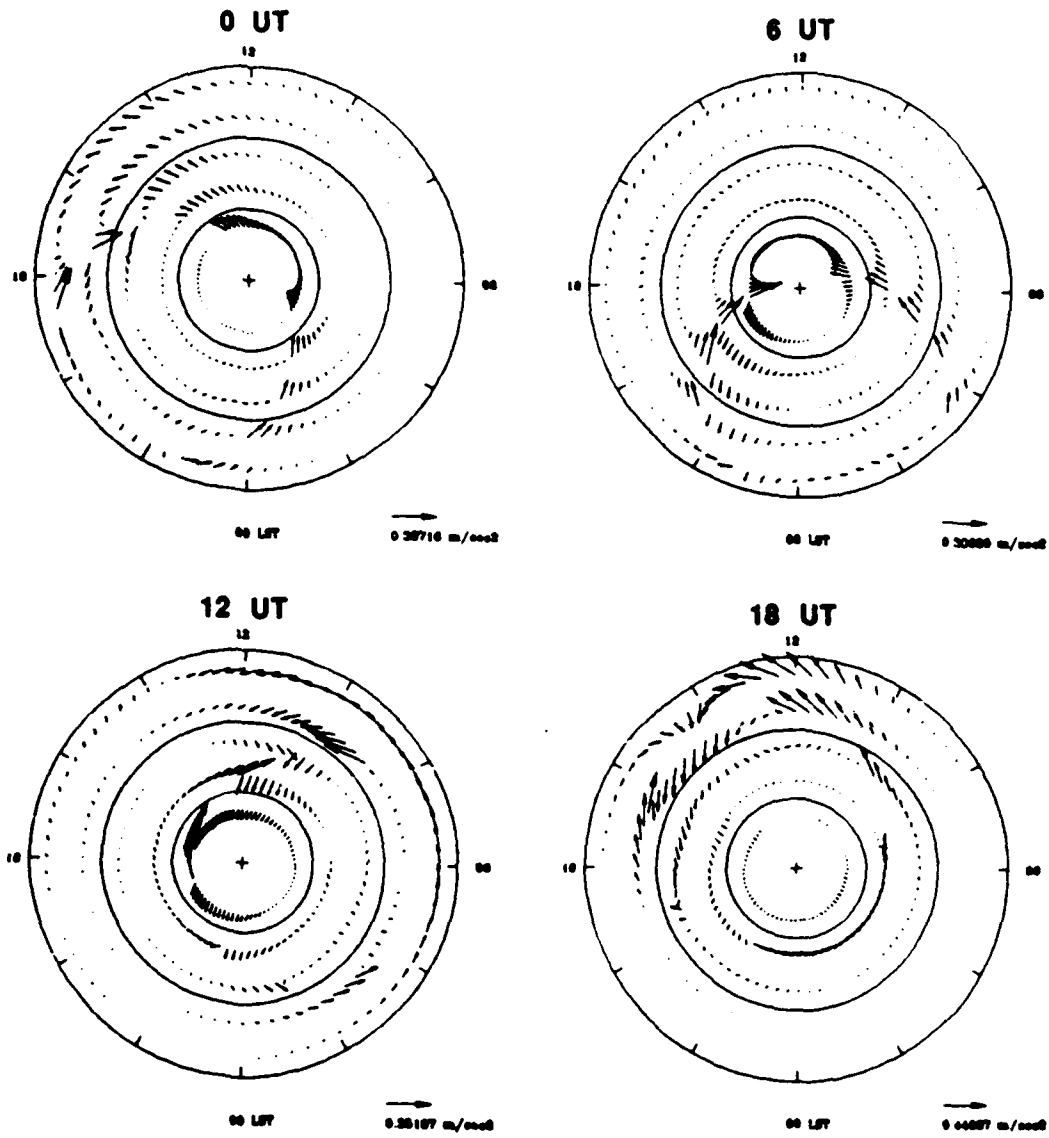
Figure 3.3 Polar dial plot of TGCM ion drag force. Direction of force is the same as the ion wind.

Pressure Gradient

0 UT

6 UT

12 UT

18 UT
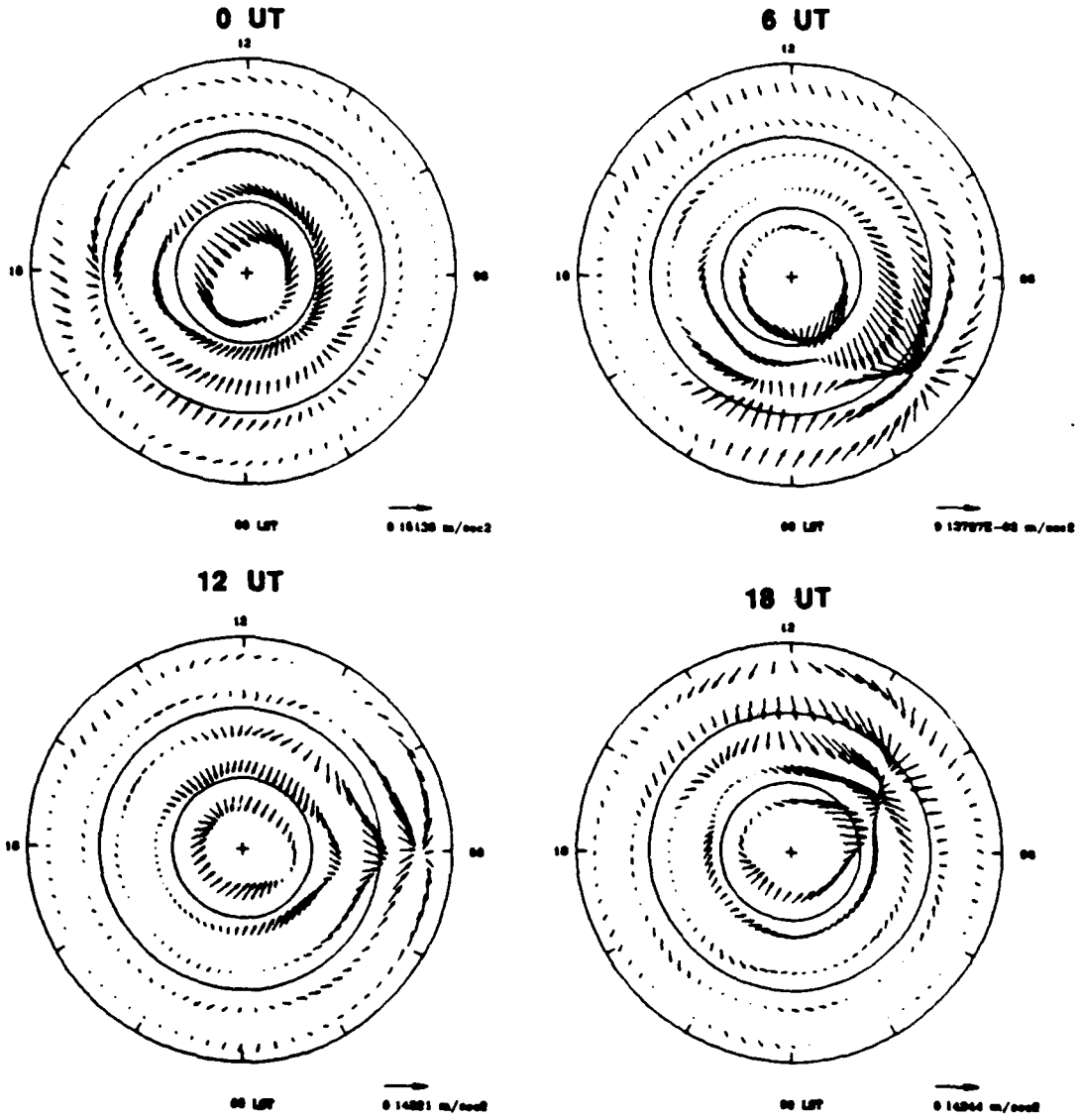
Figure 3.4 Polar dial plot of the TGCM pressure gradient force. Vectors converge in centers of low pressure and diverge in centers of highs.

Coriolis

0 UT

6 UT

12 UT

18 UT
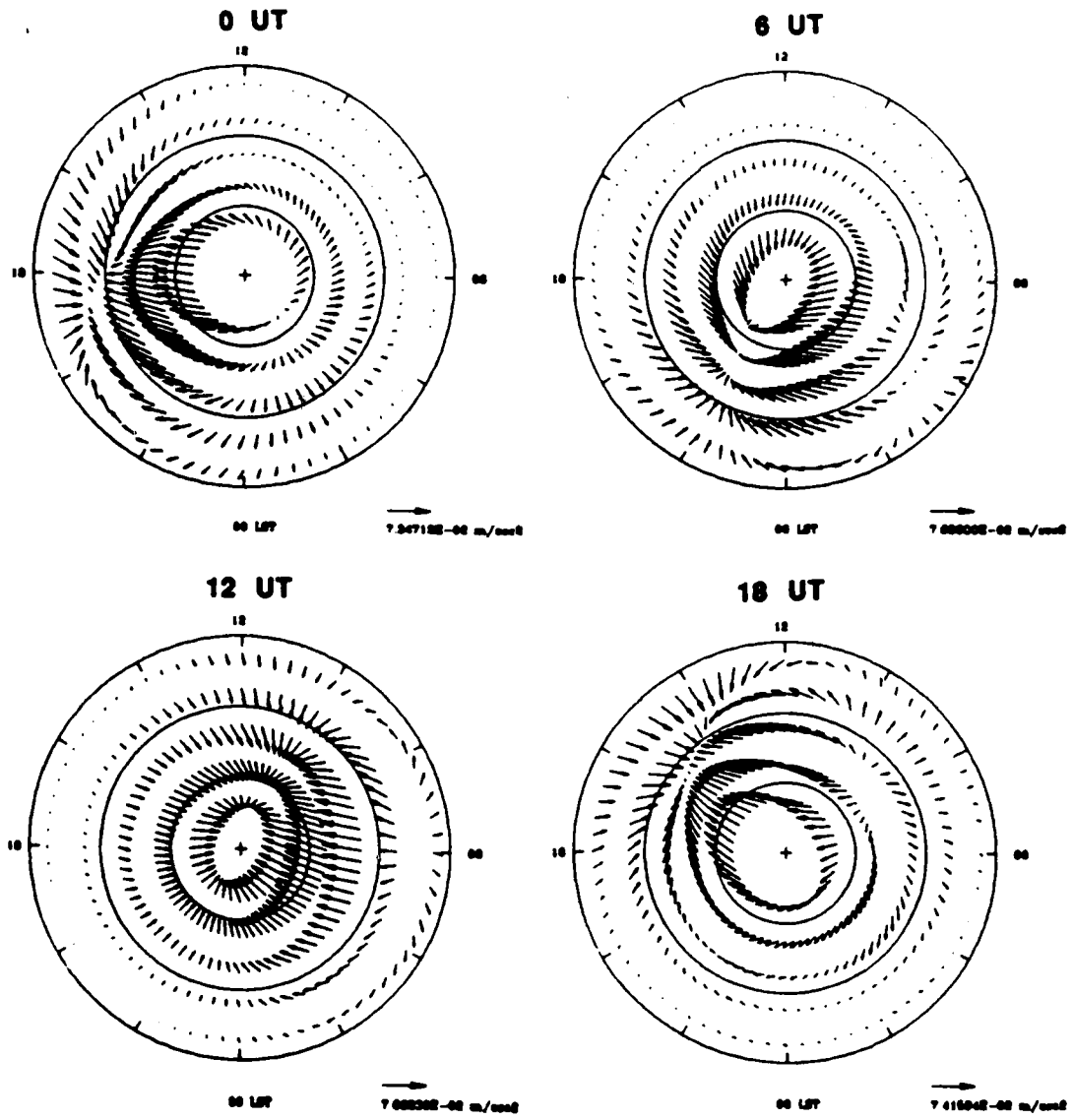
Figure 3.5 Polar dial plot of the Coriolis force. Force vectors converge toward centers of anticyclonic circulation and diverge from centers of cyclonic circulation.

Viscous Drag

0 UT

6 UT

12 UT

18 UT
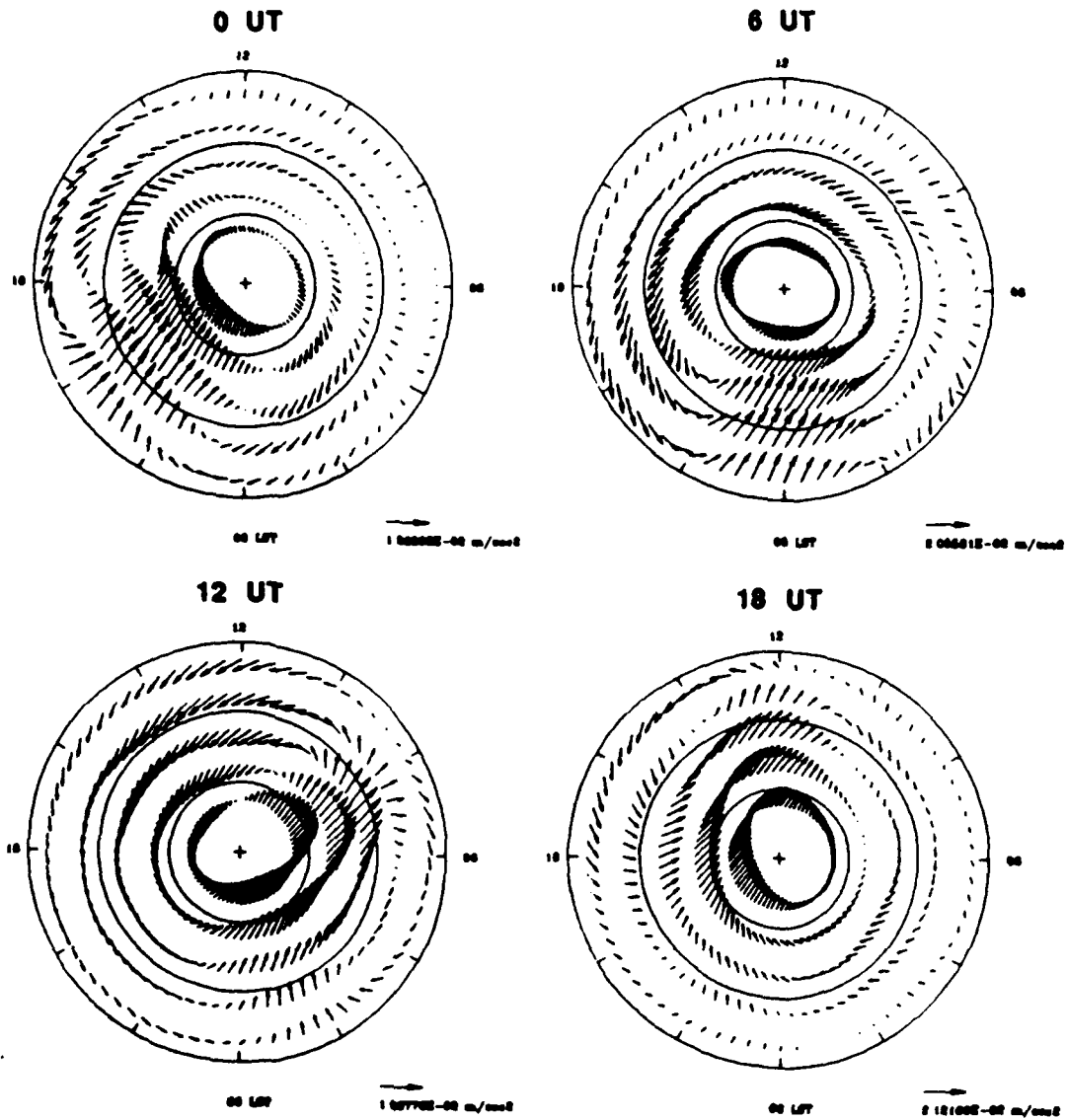
Figure 3.6 Polar dial plot of TGCM viscous drag force. Forcing patterns are well defined but magnitude of force is relatively low.

Momentum Advection
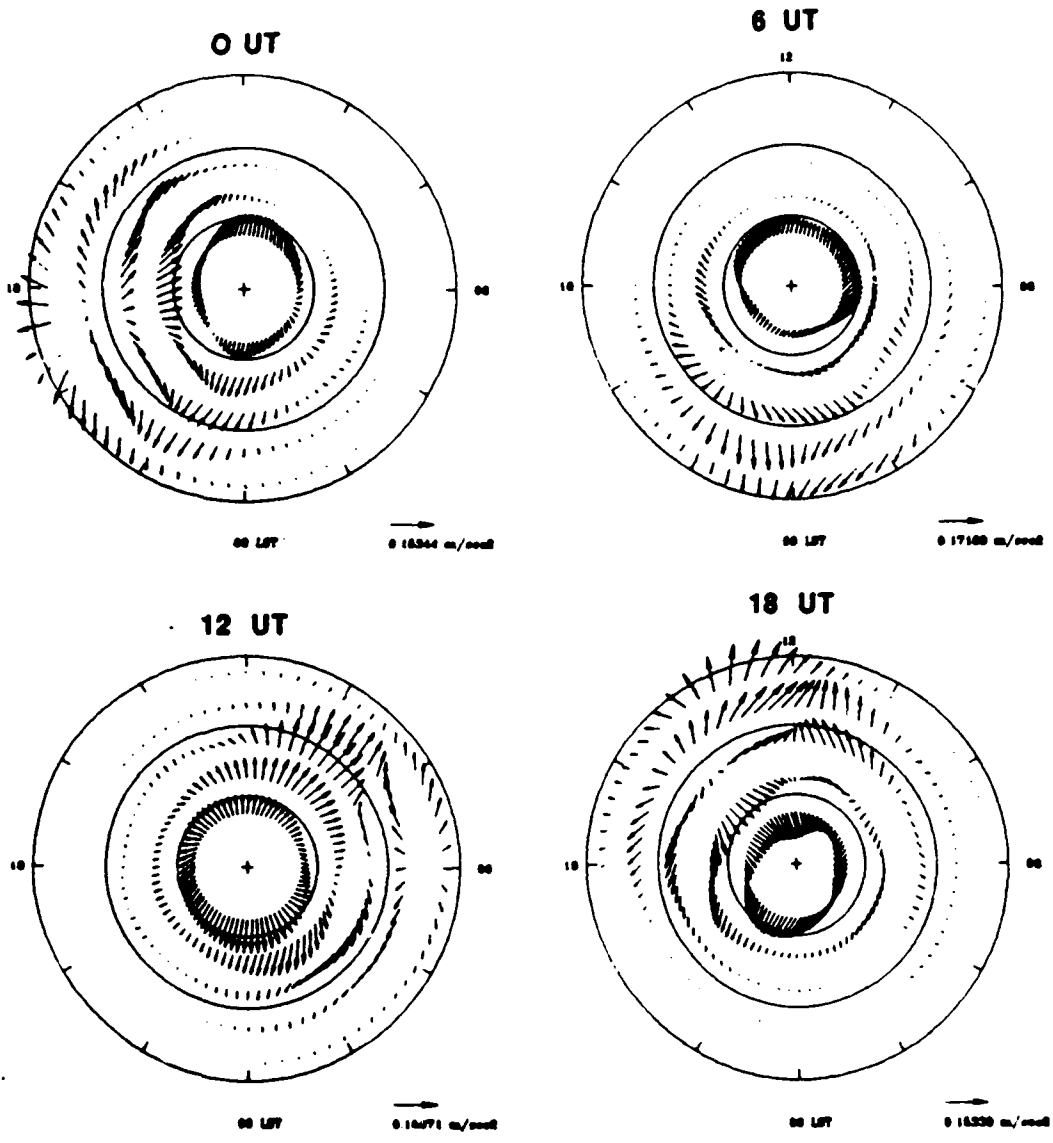
Figure 3.7 Polar dial plot of TGCM momentum advection term.

VSH Neutral Wind

O UT

6 UT

12 UT

18 UT
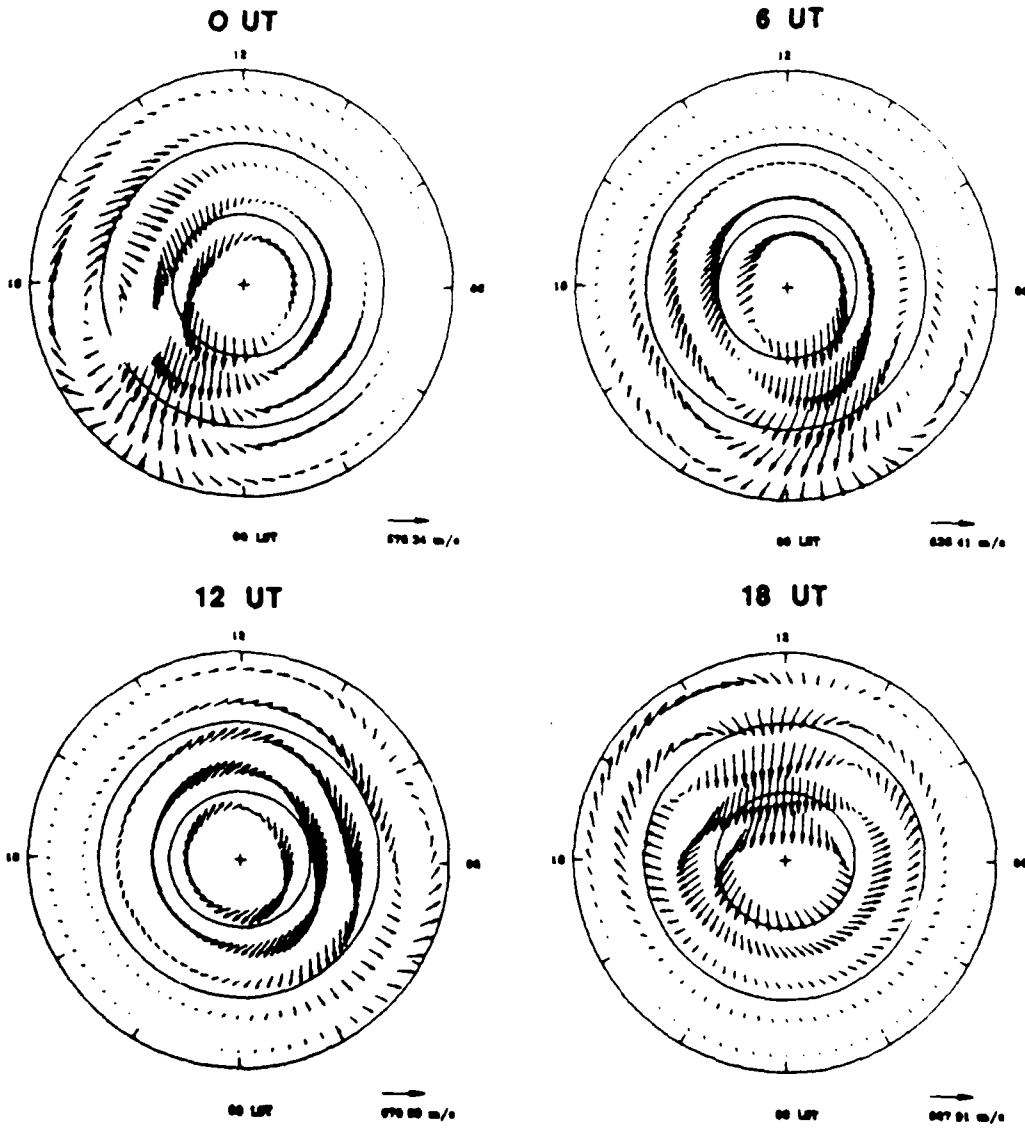
Figure 3.8 Polar dial plot of neutral wind computed by VSH model. Descriptive
parameters used in the calling sequence are also shown

Neutral Winds Orbit: 7217
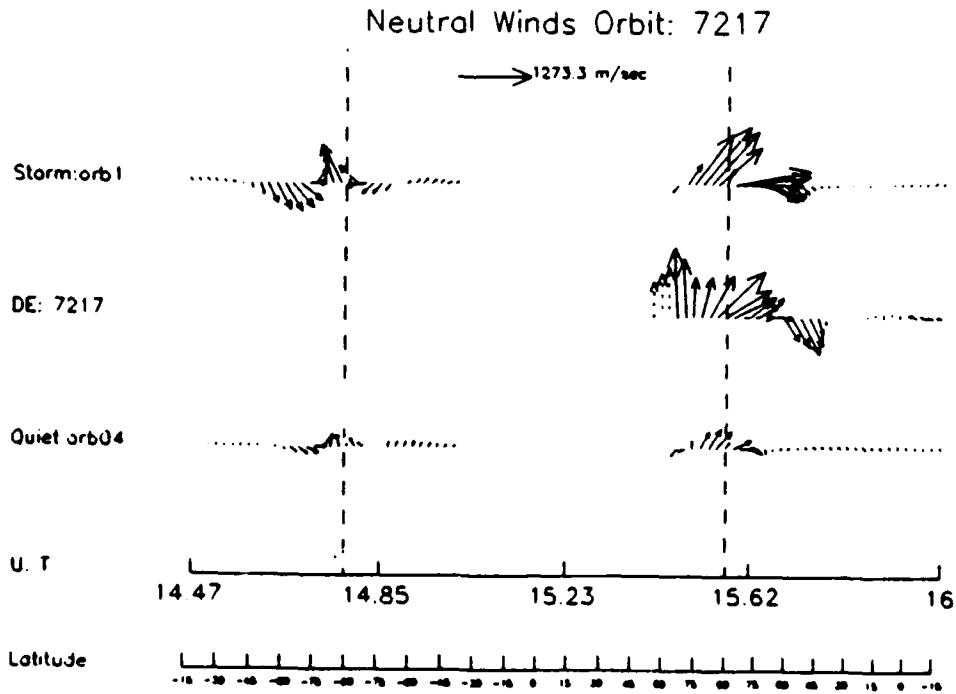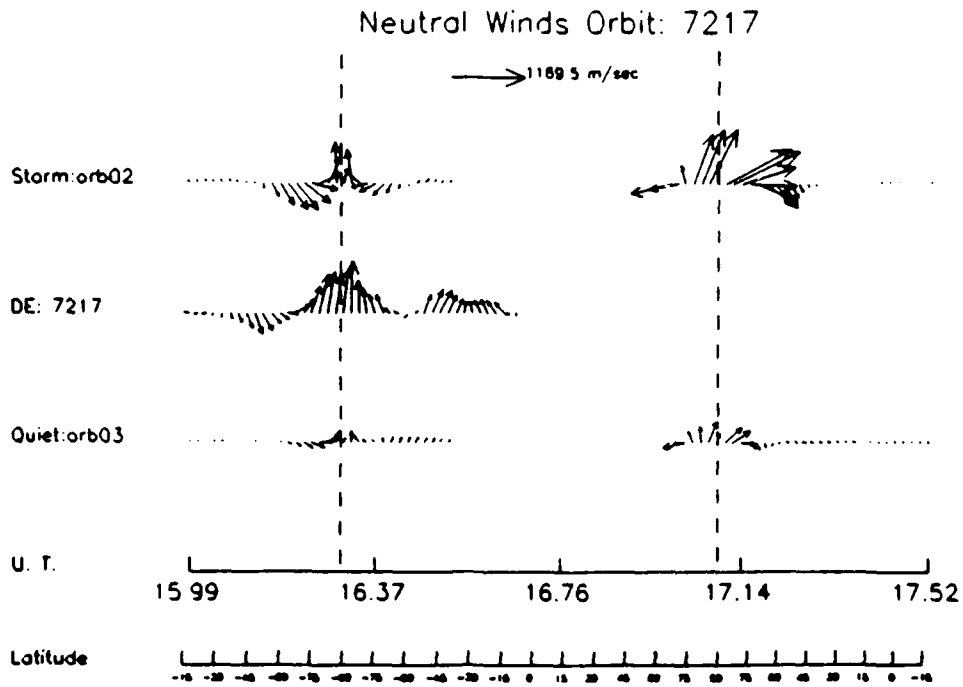
Figure 3.9 DE satellite observed neutral winds compared with TGCM predicted winds
using two different levels of geomagnetic activity as input. Storm input case agrees
well with observed winds.

20

Chapter 4 Experiments with the Momentum Equation

The chapter contains the bulk of the actual work in this project. It involves using the available tools to try to experimentally verify the momentum equation at thermospheric altitudes. The first section we consider the case of an observer fixed at some specified location. With the working data base and archived data available, we compare the measured acceleration of the winds and compare it to the simultaneous forces acting there. In section 4.2 we do much the same thing for the case of a special class of moving observers by simulating the observations of polar orbiting satellites. Finally, in section 4.3 we perform the same analysis on a set of archived DE2 satellite data.

4.1 Fixed Observer Simulation

In this section we seek to experimentally verify the momentum equation using computer generated data from the TIGCM. The momentum equation can be represented in schematic form as follows:

$$\frac{\partial u}{\partial t} = \Sigma F_x - V_r \cdot \nabla u$$

$$\frac{\partial v}{\partial t} = \Sigma F_y - V_r \cdot \nabla v$$

(4-1)

Where ΣF_x and ΣF_y represent the sum of all real or apparent forces acting at a particular location. These forces include all those that were first mentioned in the second chapter; namely, ion drag, pressure gradient, Coriolis, and viscous drag. The second term on the right hand side in (4-1) is the advection term where V_r is the relative wind and is defined as the difference between the observer's velocity and the wind velocity (see Apendix A). Our first experiments involve fixed locations, which is equivalent to a stationary observer, so the value of V_r is simply the local wind velocity. Quite often the summation of the individual force terms is combined with the advection term and is simply referred to as the *total force*. Appendix A explains that the advection term is not a real force in the same sense that the other terms are, but is necessary to account for relative motion between the observer and the medium being measured.

If all the forces acting on the neutral atmosphere are accounted for in (4-1), then we have a true equality between the observed local acceleration (the left hand side) and the total

force term (right hand side). We note, however, that we have equality only in the infinitesimal limit of space and time. Thus, if we wish to experimentally verify the momentum equation, we must realize that the best we can hope for is an *approximate* equality. We will proceed in a fashion similar to that described in Appendix A and approximate the left hand side of (4.1) by calculating the slope of the wind component evolution curves for a fixed location and comparing this value with the total force computed by the model.

Figure 4.1 depicts a set of microfiche-based TGCM data. The top two diagrams describe a 24 hour evolution of the neutral wind components at the location shown (42.5, - 85) corresponding to the approximate location of Ann Arbor. This data set was obtained for the Z=1 pressure level, which corresponds to approximately 300 km in altitude. We observe from these curves that the neutral wind evolves smoothly over time. We should therefore expect a smooth curve drawn through the discrete data points to be a good representation of a continuous set of data. We should also expect to be able to calculate very reasonable approximations to the time derivative of the neutral wind components.

The bottom two diagrams show the time evolution of all the forces acting at this location. The breakdown of the curves is shown at the top of each diagram and reads as follows: A = Ion Drag; B = Coriolis; C = Pressure Gradient; D = Viscous Drag; and E = Advection. There is also a curve labelled F and conveniently represents the sum of the A thru E curves. We observe from this pair of diagrams is that the pressure gradient curve (C) and the ion drag curve (A) are clearly the dominating forces. We also note that these forces tend to act in opposition to each other, so that the total force curve (F) is usually small in magnitude and does not venture far from the zero force line.

The values for the neutral wind and total force curves can be taken directly from the diagrams and the results are shown in figure 4.2(a,c). Data points were taken for every hour and the points connected using a natural cubic spline function. The observed acceleration of the wind components (figure 4.2(b)) was taken to be the slope of the wind evolution curves and was computed using interpolated values from the same spline function. The momentum equation implies that the total force curve for each component should be very similar to its corresponding observed acceleration curve.

A qualitative comparison of figures 4.2(b) and 4.2(c) shows that the curves are indeed very similar. We can get a feel for their degree of similarity by integrating the total force curve with respect to time and comparing the result to the wind evolution curves. To this end we can use a simple Simpson's rule numerical integration on an odd number of the discrete values for the total force. The accuracy of this method can be tested by first performing it on the values of the observed acceleration. The results in figure 4.3(a) show

22

that the integrated values (symbols) fall exactly on the wind component curves (smooth lines) . This shouldn't be surprising, since Simpson's rule is exact for cubic functions, which is basically what a spline function is.

The result of integrating the total force curve is shown in figure 4.3(b); as before, the symbols are integrated values and the curves are the actual wind components. While in this case the points don't lie exactly on their respective curves, the general trends are acceptably close to the acceleration curve. The fact that there isn't exact agreement could (in this particular case) be the result of errors in manually digitizing the data points, errors in using the cubic spline to interpolate the actual wind and forcing evolutions, or even inaccuracies in the graphs of the archived data. The numerical integration procedure shouldn't be considered as a major source of discrepancy, since it was shown to be exact for the cubic spline.

This experiment can be repeated for virtually any location using the working data base generated by the TIGCM, but one natural location to consider is the one used with the archived data. A summary of the evolution of the individual forcing terms for the zonal and meridional neutral wind components is shown in figure 4.4. The breakdown of the curves is exactly the same as it was in the case of the archived data. We note once again that the pressure gradient and ion drag terms dominate and have a pronounced tendency to oppose each other. Summing of all the individual forces produces a net force curve (6) that is small in comparison with either the ion drag or pressure gradient force.

The evolution of the wind components for the $Z=2$ pressure level above the (42.5, -85) grid point.is shown in figure 4.5(a). We observe once again the very smooth nature of the changing wind components and claim that a cubic spline fit to the data will provide a reasonably accurate approximation to a continuous data set. The derivative calculations are again made using interpolated values and the results are shown in figure 4.5(b), and they attest to the relatively inactive nature of the atmosphere at this location. Accelerations change smoothly and the magnitudes are small (on the order of .005 m/sec^2). Based on the observed accelerations we should expect the total force curve to exhibit similar characteristics; namely, small magnitudes varying smoothly with time.

The total forcing curve was reproduced in figure 4.5(c) using the same scale as that of figure 4.5(b). It is immediately apparent that the two figures don't match to the same degree as those in the archived case. A careful comparison of the two figures; however, shows that the zonal and meridional forcing curves actually agree quite well with the observed acceleration curves between 4 and 12 UT (-2 and 6 SLT). Beyond that time range the zonal forcing curve grows considerably until 16 UT, where it is several times the magnitude of the observed acceleration. It then drops off rapidly until it shows a large

acceleration in the opposite direction. Since we are dealing with a diurnally reproducible data set, the net effect of the total force over the 24 hour period ideally should be zero. The large overshoot of the total force after 12 UT would therefore be accompanied by a large undershoot prior to 4 UT, (where the total force curve is reasonable). So in this loose sense the total force curve is consistent, but it doesn't explain or account for the discrepancies; the two curves should be similar.

To check whether this discrepancy is a general condition or merely a local phenomenon, the analysis was repeated for three latitudes along the zero degree meridian. The results are in figures 4.6 through 4.8, and they indicate the same sort of response. During the eight hour period prior to 6 SLT the forcing curves for both components are in good agreement with the observed acceleration; the meridional component generally being the better of the two. Beyond 6 SLT the forcing curve tends to show greater acceleration than is observed. The conclusion is that the apparent imbalance between the measured forces and the observed acceleration is not limited to a single location.

We can begin to get a feel for what the source of the discrepancy is by looking again at figure 4.4 and noting that the total force curve (6) rises and falls in concert with the ion drag curve (1) both in the overshoot of region excessive force (6 to 13 SLT) and in the undershoot region (14 to -2 SLT). It is the period from 6 to -2 SLT when the ion drag force becomes significant. It may therefore be reasonable to assume a problem with the measurement of the ion drag contribution to the total force. To explore this possibility, it is instructive to define a new value dubbed the "residual." The residual is the value the ion drag force would have to assume to provide a perfect force balance. Expressed numerically it is the difference between the observed acceleration and the sum of all the other forcing terms as follows:

$$\text{Res}_x = \frac{\partial u}{\partial t} - (\Sigma F_x - ID_x)$$

$$\text{Res}_y = \frac{\partial v}{\partial t} - (\Sigma F_y - ID_y)$$

(4-2)

It is clear from these equations that if the residual were used in place of the ion drag force, then the total force and local acceleration curves will exactly coincide. Plotting the residual and ion drag forces together gives immediate indication as to how far off the ion drag term really is (assuming that is the problem).

The ion drag and the residual curves are plotted together in figures 4.9 through 4.12. Where the residual and ion drag curves are close together, the total force is in close balance with the observed acceleration. When the two curves separate, the imbalance

grows. A quick comparison between these plots and those of the ion density in figure 4.13 shows that the regions of force imbalance strongly coincide with the periods of increased ion density, which is one of the determiners of the strength of the ion drag force.

The result for the case depicted in figure 4.9 (42.5,-85) shows that the zonal ion drag force is about 56% greater than what it should be at both the overshoot and undershoot extremes. In fact, this zonal ion drag curve appears more or less proportional to the residual curve. The meridional case, on the other hand, shows that the ion drag is actually smaller in magnitude than the residual. This means that if the ion drag force were slightly stronger (about 20%), then the meridional total force would balance reasonably well with the observed acceleration.

Examination of the same figures for the zero degree meridian (figs 4.10 - 4.12) reveals a similar story. Both the zonal ion drag term and its residual exhibit a sinusoidal variation between 6 and 0 UT. The zonal ion drag appears too strong at the extremes of positive and negative acceleration, and appears roughly proportional to the residual value especially in the overshoot region where ion drag is greater. It would also appear that the phase of the ion drag consistently leads the residual by slightly less than one hour, though it is unknown what significance if any this may have.

In contrast to the zonal ion drag's sinusoidal pattern the meridional ion drag exhibits a quasi-symmetric behavior about local noon. The figures show that the ion drag exceeds the residual in magnitude between 6 and 15 UT with maximum discrepancy occurring near 11 UT, where ion drag is about 30% too strong. That the residual and ion drag curves converge at 15 UT is somewhat of a surprise, since figure 4.13 shows that at 15 UT the ion density is still more than half its daytime maximum. Another interesting feature is found in the curves for 47.5 degree latitude (figure 4.12). In this case the ion drag and residual curves appear to agree slightly better than for the lower latitudes, whereas the the zonal drag case clearly got worse with increasing latitude.

To try explain why the ion drag force (as calculated by the diagnostics processor) is anything other than what it should be (there should be no residual); we have to consider a subtlety in the TIGCM model. We recall that the archived data case exhibited good force-acceleration balance for the entire period and no problem with ion drag was evident. However, the particular version of the TGCM that created that data used previously archived values for the ion drag tensors used in the momentum equation. Since the same tensor values used in generating the global wind field were used to recover the ion drag forces, there was little observed discrepancy. The later version of the TIGCM computed its own values of the ion drag tensors. The tensor values recovered by the diagnostics processor could conceivably differ slightly from those used during the model run. If this is

the case, then the ion drag force thus computed will be different enough to produce a discrepancy in the force balance equation as was noted. How or why the ion drag tensors should differ between the model run and diagnostics package is an elusive question to date.

We have shown in this section that the momentum equation can in principle be experimentally verified for a fixed location when the total force curve is known to be accurate. We have also shown that the TIGCM data has definite but limited value in demonstrating this balance. We must, therefore, exercise caution in using calculations from this data where the ion drag force is dominant. When the magnitude of the ion drag force is on the same order as the rest of the terms in the momentum equation, the observed acceleration tends to agree with the total force. We will therefore try to restrict future computations to periods when the ion drag term is at a minimum. The next section describes similar experiments for the case of a moving observer.

4.2   Simulated Satellite Observations

The previous section considered a stationary observer at a fixed location in space. The results showed that when the ion drag force is small, the agreement between the local time derivative and the total forces is actually quite good. Problems begin when ion drag force becomes dominant as the ion density grows rapidly after local sunrise. This section repeats the experiment for the case of a special moving observer: a satellite orbiting the earth.

The basic problem of computing the total derivative of a measured quantity for a moving observer is discussed in great detail in Appendix A. The problem states that for an observer moving with a known velocity V_m, he will observe a time rate of change in that measured quantity according to the following equation:

$$\frac{dQ}{dt} = \frac{dQ_b}{dt} - V_r \cdot \nabla Q \quad \{ V_r \equiv V_w - V_m \} \tag{4-3}$$

The first term on the left hand side represents the rate at which the measured quantity is changing within the medium itself. This is often also described as the changes observed while following the motion of the air. It is instructive to think of this term as the rate that of change within the airstream at the observer's location and at a specific time. To avoid any unnecessary confusion regarding different frames of reference we will restrict this discussion to a single reference frame (coordinate system); namely, the spherical coordinate system of the earth.

The second term on the right hand side (including the minus sign) is the advective term. Its function is to relate observed changes to the actual changes within the air that result from physical processes. Note that the advective term includes both the wind velocity (V_w) and the observer's velocity (V_m), and both are measured in terms of the well defined coordinate system of the earth. The spatial gradient of Q is likewise computed within the earth's coordinate system.

The measurable quantities of interest in this study are, of course, the neutral wind components **u** and . The physical processes responsible for changes to these quantities within the medium (the airstream) are merely the forcing terms appearing in the momentum equation. The form of the momentum equation appropriate for the earth's rotating reference frame was presented in chapter 2. Replacing the first term on the right hand side of (4-3) with these forcing terms, we come up with the following equations:

$$\frac{du}{dt} = -\frac{1}{\rho r \cos\phi}\frac{\partial P}{\partial\lambda} + \frac{\eta}{\rho}\frac{\partial^2 u}{\partial z^2} + fv + \bar{v}_{ni}(u_i - u_n) + \frac{uv\tan\phi}{r} - (V_w - V_m)\cdot\nabla u$$

(4-4a)

$$\frac{dv}{dt} = -\frac{1}{\rho r}\frac{\partial P}{\partial\phi} + \frac{\eta}{\rho}\frac{\partial^2 v}{\partial z^2} - fu + \bar{v}_{ni}(v_i - v_n) - \frac{u^2\tan\phi}{r} - (V_w - V_m)\cdot\nabla v$$

(4-4b)

Since the goal of this section is to demonstrate force balance from satellite observations, we must consider only the terms that are calculable from satellite observations. The first term on the right hand side of equations (4-4) involves the pressure gradient force. We recall from the previous section that the pressure gradient force was largely responsible for balancing the ion drag force, and thus it is an important contributor to the total force. We also note that to compute a pressure gradient (or any gradient) requires simultaneous measurements that are separated spatially. In the case of a polar orbiting satellite (such as Dynamics Explorer 2), it is impossible to compute a zonal pressure gradient, since measurements are only available along the track of the satellite. It is therefore unlikely that equation (4-4a) can be useful in demonstrating force balance, so calculations involving the acceleration of the zonal component (u) of the neutral wind will not be considered.

The major forcing terms of the meridional component () equation (4-4b), on the other hand, can be calculated (or closely approximated) from satellite observations. The pressure gradient term in (4-4b) is calculated along a line of constant longitude. Typical polar orbiting satellites travel at speeds of about 8 km/sec along a line of nearly constant longitude. It should be possible in principle to measure the pressure along the satellite track and compute the meridional pressure gradient from these measurements. Of course, the

27

measurements won't actually be simultaneous, but the actual time involved is small compared to local accelerations and we would expect this to be a reasonable approximation to the actual pressure gradient.

There are still some remaining terms which cannot be calculated from satellite observations. The viscous drag term contains a vertical spatial (second) derivative and cannot be computed. The viscous drag term was shown in chapter 3 to be a very small contributor to the total force. Failing to include this term should therefore have minimal impact on momentum equation calculations. The advection term in (4-4b) can be expanded to reveal another non-calculable term:

$$- (\mathbf{V}_w - \mathbf{V}_m) \cdot \nabla v = - \left[(u - V_x) \frac{1}{r \cos\phi} \frac{\partial v}{\partial \lambda} + (v - V_y) \frac{1}{r} \frac{\partial v}{\partial \phi} \right] \qquad (4\text{-}5)$$

In the above expression, the quantities V_x and V_y are the eastward and northward components of the satellite's velocity with respect to the earth's rotating coordinate system. For a satellite whose orbital inclination is exactly 90 degrees, V_y is merely the satellite's orbital speed. The value of V_x is the earth corotational speed at the radius of the orbit. The first term in the brackets on the right hand side is the zonal advection of the meridional component and clearly cannot be calculated. The second term is the meridional advection of the meridional term (MAv) and can be approximated in much the same manner as the pressure gradient force. Whereas the viscous drag term could be confidently ignored, it remains to be seen what the effect of neglecting the zonal advection term will be. Yet in spite of these few non-calculable terms, the meridional component equation would seem to be well-suited for this experiment.

Collecting all the terms that can be calculated yields the working form of the meridional momentum equation:

$$\frac{dv}{dt} \cong - \frac{1}{\rho r} \frac{\partial P}{\partial \phi} - fu + \bar{v}_{ni}(v_i - v_n) - \frac{u^2 \tan\phi}{r} - (v - V_y) \frac{1}{r} \frac{\partial v}{\partial \phi} \qquad (4\text{-}6)$$

This expression would at first appear to be restricted to meridional motion only, but it can be suitably adapted to represent the approximate changes observed to a *westward* moving observer (satellite) as well.

Consider the diagram depicted in figure 4.13. This diagram depicts three successive orbits of a satellite with a 90 degree inclined orbit and a 90 minute orbital period. The satellite will move northward along lines of nearly constant longitude during any short time interval of a given orbit, yet progresses 22.5 degrees (15 deg/hr x 1.5 hrs) westward after one complete orbit. Thus, in addition to the obvious case of a northbound

observer taking continuous observations, there is an analogous case of a westward moving observer recording observations every 90 minutes. To apply this analogy, though, it will be necessary to modify (4-6) by removing the northward component of the satellite's velocity. We thus now have the following two forms of the meridional equation to work with:

$$\left(\frac{dv}{dt}\right)_\phi \cong -\frac{1}{\rho r}\frac{\partial P}{\partial \phi} - fu + \bar{v}_{ni}(v_i - v_n) - \frac{u^2\tan\phi}{r} - \frac{v}{r}\frac{\partial v}{\partial \phi} \qquad (4\text{-}7a)$$

$$\left(\frac{dv}{dt}\right)_\lambda \cong -\frac{1}{\rho r}\frac{\partial P}{\partial \phi} - fu + \bar{v}_{ni}(v_i - v_n) - \frac{u^2\tan\phi}{r} - (v - V_y)\frac{1}{r}\frac{\partial v}{\partial \phi} \qquad (4\text{-}7b)$$

The first expression describes the observed rate of change of component v along a line of constant latitude, while the second refers to the rate of change along a meridian. It cannot be emphasized enough that the velocity components appearing in these expressions are measured relative to the earth's coordinate system and not to the observer. Thus, in the last term of (4-7a) v is the wind's actual meridional component. So with two working equations in hand, it is now possible to define the experiment.

4.2.1 Simulation 1 Constant Longitude

This experiment examines both of the working equations by simulating an orbiting satellite collecting data along its track. The first simulation involves a satellite moving along a meridian recording quasi-continuous data. The second simulation tests the constant latitude momentum equation by looking at data from three successive orbits.

The first experiment demonstrates the effects of trying to apply the constant longitude equation to a short orbit segment. This is accomplished by parameterizing an ideal orbit along a single meridian. For this simulation the hypothetical satellite proceeds northbound along the zero degree meridian and records data every .5 degrees of latitude between 37.5 and 87.5 degrees. This corresponds to a satellite with a 96 minute orbital period and recording data every 8 seconds, which closely approximates the performance of the DE-2 satellite. Data was recorded by performing time interpolations on the working TIGCM data base at 5 degree latitude increments from 37.5 to 87.5 degrees. A cubic spline routine was then used to interpolate between these knot points at .5 degree intervals. Simulated data was thus obtained for U_n, V_n, Vdrag, P_y, VCor, Geom (curvature), and MAv. The orbit parameterization and recorded data are summarized in table C.1 (see Appendix C).

A graph of the recored values of V_n for the second orbit is shown in figure 4.15(a). Each symbol represents a single data point along the satellite's track as data is recorded every 8 seconds. The graph shows that it took the satellite only 800 seconds to travel from 37.5 to 87.5 degrees in latitude, so this trace should be a close approximation to the "snapshot" of a meridional distribution of V_n along the zero degree meridian. This is illustrated in figure 4.15(b), which shows the distribution of V_n along the zero degree meridian at the three hourly times indicated. Clearly, the profiles don't change drastically from one hour to the next, so no significant change should occur along the meridian during one pass. While this fact makes meridional advection calculations possible, it has dire consequences as far as the momentum equation experiment is concerned.

The total derivative term in the constant longitude equation is calculated by computing the slope along the V_n trace curve at each point of interest. This is easily done using finite centered differences, and the results are shown in figure 4.16(a). This result is then compared to the summary of the momentum equation terms shown in figure 4.16(b). The most striking feature of these figures is that the total time derivative curve from 4.16(a) is virtually identical to the meridional advection term of 4.16(b). The reason for this is that the satellite's orbital speed of some 8,000 m/sec is figured in the momentum advection calculation, thus resulting in a dominating term. But this is just being consistent with what was stated earlier; namely, that the meridional wind profile isn't going to change very much in the 800 seconds it takes for the satellite to complete its pass. This being the case, it is doubtful that the forcing effects of the acceleration on the airstream can be detected even if the known effects of the advection are subtracted out. In practise, there will be a certain amount of uncertainty involved with the wind measurements, which will carry over into the advection calculations. It is likely that the uncertainty in the advection term alone will be greater that the magnitude of the instantaneous acceleration of the airstream. More on the effects of uncertainty is discussed in the next section. In summary, it would appear that the meridional component equation isn't well-suited for force balance analysis.

4.2.2 Simulation 2 Constant Latitude

The next phase of the experiment involves the constant latitude momentum equation. Recall that this equation is analogous to a westbound observer recording wind data every 90 minutes. There are two inherent limitations in trying to experimentally verify the constant latitude momentum equation. As was previously mentioned, there is no practical way to measure the zonal gradient of V_n; hence, the zonal advection term cannot be included. In addition, observations of wind velocity are necessarily limited to one per orbit for any given latitude. The total time derivative of the wind speed must be

30

approximated using a centered difference with a time step on the order of 100 minutes. By making appropriate use of the working data base and VSH model, it is possible to estimate the likely consequences of these limitations.

The latter limitation is usually classified as a *limited sampling rate* problem, and it can introduce adverse effects in at least two ways. Obviously, the sampling rate must be sufficient to detect changes in the quantity being measured. This is achieved if the sampling rate frequency is several times the frequency of the time dependent quantity being measured. In addition to the sampling rate limitation, there are going to be uncertainties in measurements. If these measurements will be used to compute derivatives (as in this case), then the uncertainties will carry over into the calculations of the derivatives. Both these effects can be demonstrated rather easily with the VSH model.

To demonstrate the sampling rate limitation, a simulated observational platform was allowed to "orbit" the earth in a westerly direction along a line of constant latitude and with a circumnavigational period of 24 hours. The starting point was the 180 degree meridian at 0 UT at an altitude of 395 km. The observer's longitude changed at a rate of 15 degrees per hour for this single excursion around the earth. The VSH subroutine was called at 130 equally spaced points along the track with the appropriate UT for each point. This was done for several different latitudes two of which are shown in figures 4.17(a) and 4.18(a). The continous line in the diagrams represents the 130 observations of V_n, and the diamonds highlight the data points that are 1.5 hours apart. By inspection of these figures it would appear that a smooth curve drawn through the highlighted points would closely resemble the continuous trace curve. The sampling rate frequency of 1.5 hours is apparently sufficient to detect changes in the winds. The next step is to determine how accurate an estimate to the total time derivative can be achieved with these data points.

The error bars on figures 4.17(a) and 4.18(a) describe a simple 5 percent relative error in the measurement of V_n. This value was arbitrarily chosen as a worst case uncertainty to examine the effects and doesn't represent an actual estimate of the error likely to be encountered in the model values or in satellite measurements. The computations of the total derivative (dV_n/dt) are shown in figures 4.17(b) and 4.18(b). Again, the solid line is the "actual" time derivative taken from the continuous data values, and the diamonds are the approximations to the derivative computed from the sampled points. The error bars in this case result from the 5 percent relative error assumption for the neutral wind measurement. It is clear from these figures that the sampling rate limitation precludes exact measurement of the total time derivative, but the resulting uncertainties are not so large as to preclude a reasonable estimate of the observed total time derivative. The errors from the

limited sampling rate are on the same order as those arising from the uncertainties in the measurements.

The effect of neglecting the zonal advection and viscous drag terms can be demonstrated on a trial basis using the working data base. This was done by selecting a fixed location and comparing the total forces present during a 24 hour period with the result obtained by subtracting the viscous drag force and zonal advection. Figures 4.19 and 4.20 show these results for two locations. It should be noted here that even though fixed locations were selected, the zonal advection appropriate for a westward drifting satellite was used. In this comparison, little was to be gained by allowing the location to change with time.

In each case, the solid line represents the total forces present at the specified location at each time. The dashed lines are the result of subtracting the zonal advection and viscous drag terms. The situation presented in figure 4.19(a) is for a high latitude case and shows the effect of large variations in the zonal wind. The summary of the zonal wind component for this location is shown in figure 4.19(b), which also depicts the satellite drift velocity (V_{mx}). Since the zonal advection term of (4-5) involves the difference in the zonal wind and drift velocity, the effect of this term will become less as the zonal wind speed approaches that of the satellite. From figure 4.19(b) it can be seen that this happens between 10 and 13 UT. It is during this same period that the difference between the two curves from figure 4.19(a) is small.

The first four hours in this case represent the other extreme, where the zonal wind adds to the effect of advection. This enhancement effect is reflected in figure 4.19(b). where there is a noticeable maximum in the difference between the two curves. This same effect is demonstrated in figures 4.20 for the case of a lower latitude and weaker winds. In this case the effect of the zonal wind, though evident, is not as significant because the zonal wind magnitude is much smaller than the drift velocity. It is also evident from the last six hours of the low latitude case that the wind speed is not the only determining factor. Here the difference between the two curves is at a minimum for the 24 hour period, yet the zonal wind is not significantly different than in earlier periods. The magnitude of the gradient of the meridional component must be contributing as well, but as was previously mentioned, cannot be measured from satellite data. The conclusion to draw from these figures is that the zonal advection term can be effectively neglected when the zonal wind speed is close to the drift velocity of the satellite. When working with actual satellite data, it is not always possible to be very selective about which locations to consider.

The procedure for this phase of the experiment was to parametrize the orbits depicted figure 4.14 and use appropriate interpolations between the grid points of the

working data base to create a set of observations for this hypothetical satellite. The parametrization was arbitrarily chosen so that the satellite passed through (42.5N, 0W) at precisely 6 UT, and the 90 minute orbital period defined the rest of the coordinate pairs. The reference starting point on each orbital pass was taken to be 30 degrees north, and data was recorded every 8 seconds after the satellite's latitude first exceeded 37.5 degrees (the southern limit of the working data base). Data values were linearly interpolated from the data base at latitudes 37.5, 42.5, 47.5, 52.5, 57.5, and 62.5; the values for longitude and UT being consistent with the orbit parameterization. These data values were then inserted into a cubic spline routine to interpolate data values for each of the latitudes where data was recorded. The orbital parameterization along with retrieved values of U_n, V_n, Vdrag, Vcor, P_y, Geom (curvature), and MAv are shown in table C.2.

The measurements of V_n from these three orbits are shown in figure 4.21(a). The dotted line in this figure is the middle orbit and is the one along which the momentum calculations are made. Note that the poleward gradient of V_n increases with time. This is to be expected, since the starting time is close to 6 UT, and we recall from the fixed observer case that the ion drag force increased substantially after 6 UT. It is also evident from the figure that the time rate of change of V_n increases substantially with latitude as time goes on. This effect is not seen at low latitudes, where the latest orbit actually showed weaker meridional winds during the third orbit.

The sum total of the measurable forces (and advection) are shown in figure 4.21(b). Also shown in this figure is the curve representing the total time derivative of V_n. Ideally, the solid curve and dashed curves should be close together because each curve represents opposite sides to the constant latitude momentum equation. The solid line is the left hand side and is computed at each latitude by taking centered differences in the meridional wind. The dashed curve is the right hand side and is the sum of all the available force terms including advection. Since the two curves bear only superficial resemblance, it might be proposed that the zonal advection of the meridional wind is significant here. To explore that possibility a third curve was added to the figure, and is the sum of the available forces and the zonal advection term. Again, the two curves bear only superficial resemblance and defy explanation.

The values of the measurable forces during the second orbit are plotted together in figure 4.22(a). The importance of the pressure gradient and ion drag force terms is clearly evident. From the earlier work with the fixed location momentum equation, it was noted that the ion drag and pressure gradient forces tend to oppose each other. From the figure it would at first appear that this is not quite the case, as both forces tend to grow in the

33

positive sense north of 50 degrees latitude. However, if the entire zero degree meridian is shown (as in figure 4.22(b)), the opposing nature of the forces is evident.

As in the case of the fixed observer, verifying the momentum equation experimentally remains an elusive goal. At least in the former case it was shown to work in the absence of strong ion drag force. In this case it doesn't seem to verify at all. In the present case, the total forces present at 40 degrees latitude, for example, would predict an instantaneous acceleration of the wind of about .002 m/sec^2. In actual fact, the wind showed a slight deceleration between the first and third orbits. Even if advection is fully accounted for, the total forces tend to exceed the predicted acceleration. An unusual twist to the present case is that it is the pressure gradient force and not the ion drag that is causing the apparent problem, since the total force is skewed in the positive sense relative to the observed acceleration. The last experiment involves actual satellite data; so if there is a problem with using model-generated data to perform momentum equation experiments, then perhaps the satellite data could yield more favorable results.

4.3 Momentum Equation Calculations from Satellite Data

In the preceding sections the momentum equation calculations were based entirely on model-generated data. In these section we perform essentially the same computations with the data taken from the DE-2 data base. The first problem one encounters when trying to do any experiment with this data is to find a satisfactory set of orbits. By satisfactory we mean orbits that contain enough of the data you need, in the right locations in the orbit for your application, and contains enough suitable orbits to make time studies possible. For this experiment we required zonal neutral winds, meridional neutral and ion winds, ion and neutral temperatures, electron, atomic oxygen and molecular nitrogen densities. To avoid problems with high latitude forcing, it was preferable to have data at low to mid latitudes. Finally, to make time derivative computations as accurately as possible, we required three consecutive orbits' worth of this data. Almost miraculously, this stringent set of requirements was filled.

Out of a data base consisting of thousands of orbits, there was only one set of three that contained full data coverage over a desirable latitude band. Orbits 8025 through 8027 filled the requirements perfectly. They contained all the required data, where it was needed, and for as long as it was needed. Figure 4.23 shows a schematic diagram of the track of these three orbits over the south geographic pole. The vectors along the satellite track represent the neutral wind. Note that is representation of the south pole is as viewed from the north pole. Thus, east is in a counterclockwise direction (the direction of increasing local time). Note also that the neutral wind vectors show a strong westerly

component in the 55 to 70 degree latitude range. As was previously mentioned, this would tend to reduce the effect of zonal advection and improve the results.

The procedure for this experiment is very similar to that of the previous section. The lower portion of figure 4.23 shows the track of the three orbits between latitudes -40 and -60. As before, the change in the meridional wind from orbit 8025 to 8027 is compared to the total forces acting along the track of orbit 8026. The only real difference between this experiment and the simulation (aside from no longer needing to parameterize the orbits) is that all the forces must be computed from the satellite data rather than interpolated from the working data base. A summary table of all the DE-2 satellite data within this 20 degree latitude band of interest as well as plots of the data listed in the first paragraph can be found in Appendix D. Descriptions of the force computations and plots of the forces along the track will be found in the paragraphs to follow.

4.3.1 Ion Drag Force

The ion drag force is calculated using the following formula taken from the momentum equation:

$$V_{drag} = \bar{v}_{ni}(v_i - v_n) = \bar{v}_{in}(v_i - v_n)\frac{n_e}{n_n} \tag{4-8}$$

Equation (4-8) looks deceptively simple, but this apparent simplicity belies the complex nature of computing the momentum transfer collision frequency, v_{in}. The ion-neutral collision frequency is actually a combination of the collision frequencies between the oxygen ion and the two dominant neutral species listed above. The formulas for these two collision frequencies are:

$$\bar{v}_{iN2} = C_3 \, nN_2 \tag{4-9a}$$

$$\bar{v}_{iO} = C_1 \, nO \, T_r^{1/2}[\,1 - C_2 \log_{10} T_r]^2 \tag{4-9b}$$

where:

v_{iN2}	=	ion - nitrogen collision frequency
v_{iO}	=	ion - oxygen collision frequency
nN_2	=	nitrogen number density
nO	=	oxygen number density
n_e	=	election (ion) density
T_r	=	$(T_i + T_n)/2$

3 5

C_1	=	Resonant collision frequency coefficient
C_2	=	Oxygen collision frequency constant
C_3	=	Non-resonant collision frequency coefficient

In the above equations the constants C_1, C_2, and C_3 are taken from *Banks and Kockarts* [1973] and are $1.7 \times 3.67 \times 10^{-11}$, 0.064, and 6.82×10^{-10}, respectively. A detailed analysis on the effect of uncertainties in the measured quantities is presented in Appendix B. The result of the error analysis shows that if a 1 percent relative error is assumed for each of the quantities going into the computation of the ion drag, the resulting error in the calculation is less than 10 percent. This would probably represent a best case estimate of the ion drag.

4.3.2 Pressure Gradient Force

The pressure gradient force is in principle very easy to calculate. At each point along the track of the satellite measurements are taken of the neutral densities and the neutral temperature. Thus all the ingredients are there to calculate a pressure along each 1/2 degree of latitude as long as data is being recorded. If the satellite moved along at a constant altitude, then the pressure gradient force could be calculated with the following formula:

$$P_y = -\frac{1}{\rho}\left(\frac{\partial P}{\partial y}\right)_z \tag{4-10}$$

where ρ is the mass density of the gas. In practise the satellite's altitude usually changes as it moves along its track. To correct for the changing altitude we use the barostatic relation:

$$P_{cor} = P(z)\exp[-(z-z_0)/H] \tag{4-11}$$

where:	P_{cor}	=	Pressure corrected to reference altitude
	$P(z)$	=	Pressure at satellite altitude
	z_0	=	Reference altitude
	H	=	Mean scale height along track

The mean altitude along the track between -40 and -60 was taken to be the reference altitude. After correcting the pressure values, a single application of a 3-point smoothing routine was applied to dampen small scale variations between successive data points. The smoothed corrected pressure along the track of orbit 8026 is shown in figure 4.24(a). The

36

figure shows a definite trend toward higher pressure as one moves poleward, but there are also shorter scale undulations in pressure along the track.

Computing the pressure gradient involves little more than simply performing finite difference methods along the track, but there is a potential problem involved when measurement uncertainties are involved. If we assume as before that measurements are accurate to a relative error of 1 percent, then the error involved in computing the pressure is shown by the error bars in figure 4.24(a). The error appears to be small, but close examination reveals the error to exceed the amount of pressure change between adjacent data points. This condition has severe consequences when it comes to using centered differencing in computing the pressure gradient, as can be seen in figures 4.24(b). The error bars in this figure result from the uncertainties in the pressure values and the distance between the data points. The latter quantity appears in the denominator of the expression for the absolute error of the pressure gradient formula (see Appendix B). One could halve the calculation error if instead of using every point to compute the pressure gradient, every other point were used instead. There is a practical limit, of course, to how many points you can skip and still have a representative derivative calculation.

The actual uncertainty in this particular pressure gradient calculation is probably considerably less than what is shown in figure 4.24(b). One of the advantages in having a nearly continuous set of data points is that it allows you to perform smoothing operations and thus improve upon the uncertainty of individual data points. Thus, the errors shown in figure 4.24 may tend to be on the high side.

4.3.3 Time Derivative Computation

Computing the total time derivative of the meridional wind component is basically as simple as differencing the wind measurements from orbits 8027 and 8025 and dividing by the time difference. That, along with some enhancements, is just what was done. To make sure that wind values from identical latitudes were differenced, the raw wind data was input into a cubic spline routine and interpolated values for each 1/2 degree latitude increment were obtained. Three point smoothing was performed on the resulting wind values and the differencing calculations were performed. The values of the interpolated winds are shown in table 4-1, as are the force calculations along the second orbit. A plot of the time derivative is shown in figure 4.25(a). The error bars once again result from the assumption of a 1 percent relative error in the velocity measurements.

37

4.3.4 Force Comparison

A comparison plot of the calculated forces is shown in figure 4.25(b). The uncertainty in the pressure gradient force calculation dominates the picture as a whole. The ion drag force curve appears to be well-behaved, which lends itself to a certain amount of credibility. The undulations in the pressure gradient force are not reflected in the ion drag force, which is what one would come to expect based on previous results. There is, however, an encouraging rise in the pressure gradient force at about -57 degrees which roughly corresponds to an opposite move in the ion drag force. It would have been better, of course, had it been more closely in phase to its ion drag counterpart, especially in light of the comparison of the total force to the observed acceleration of the wind.

4.3.5 Force Balance Analysis

The somewhat disappointing results of this experiment are summarized in figure 4.25(c). The scale of the graph, so chosen to keep the total force curve within its boundaries, effectively kills the curve for the observed acceleration. Actually, the acceleration curve wrongly suggests that nothing was happening with the neutral wind during this period when, in fact, it had gone up and then down between orbits 8025 and 8026, nearly returning to the same values and yielding the small values for acceleration. The obvious conclusion from this experiment is that no conclusion is possible, at least not within the level of detail presented here.

Archived TGCM DATA

Zonal Wind

Meridional Wind

(a)

(b)

Zonal Forcing (A=ID,B=C,C=P,D=V,E=A)   Meridional Forcing (A=ID,B=C,C=P,D=V,E=A)

(c)

(d)
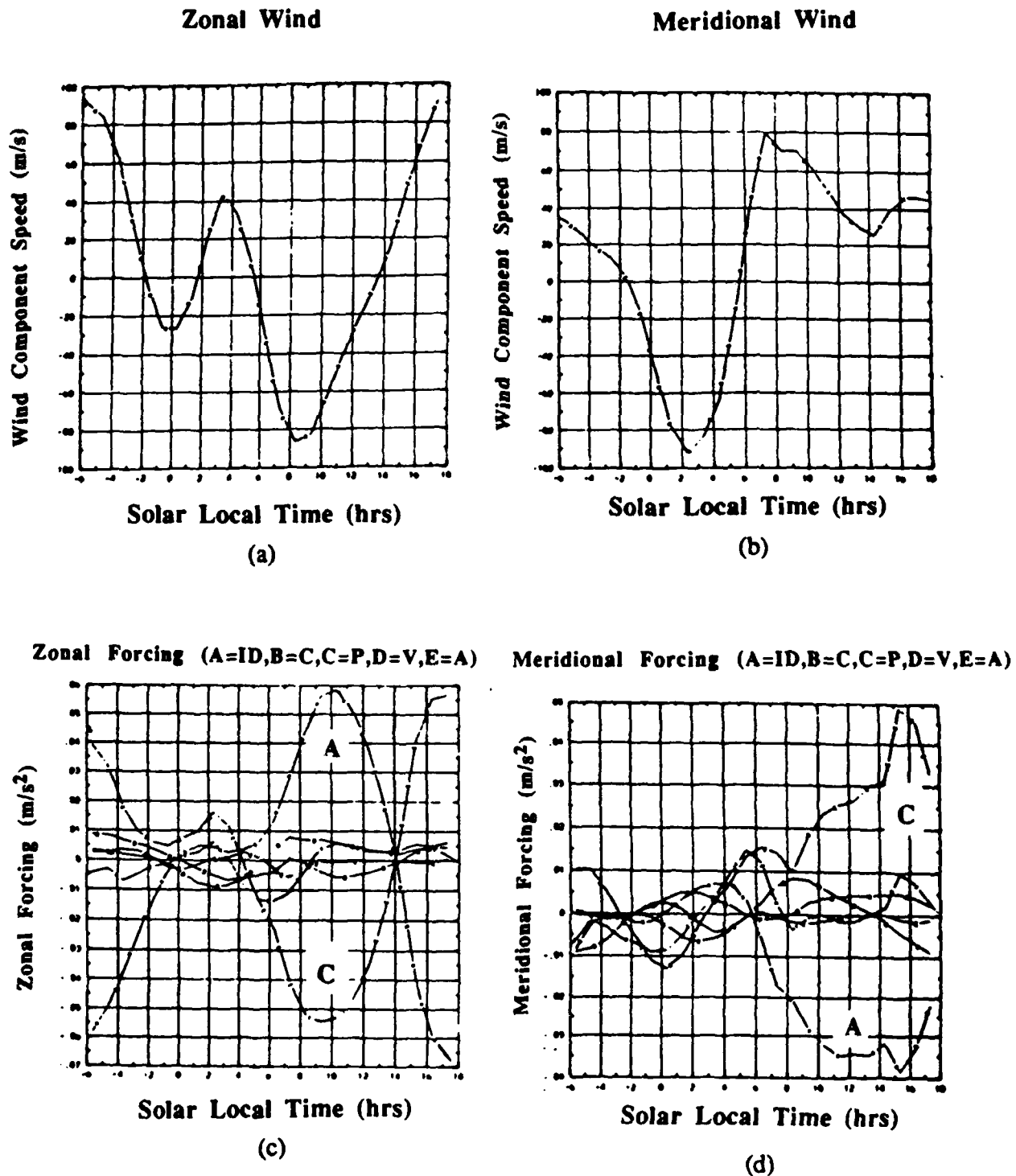
Figure 4.1 Archived TGCM data showing diurnal evolution of the zonal(a) and
meridional (b) neutral wind, and the zonal (c) and meridional (d) force
components.

39
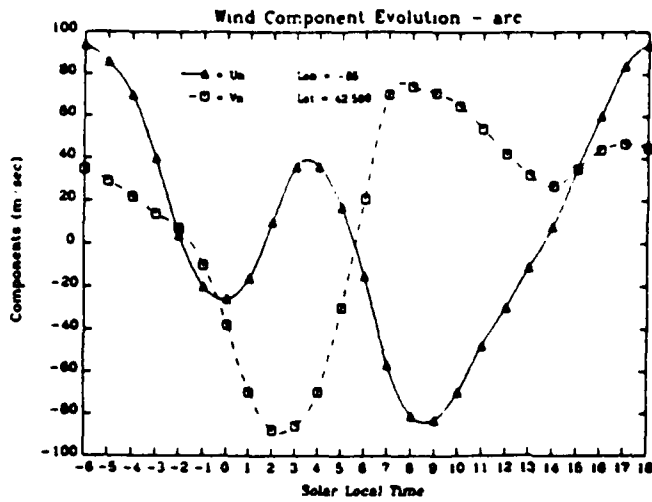
Figure 4.2(a) Evolution of neutral wind
components as appearing in archived
TGCM data.
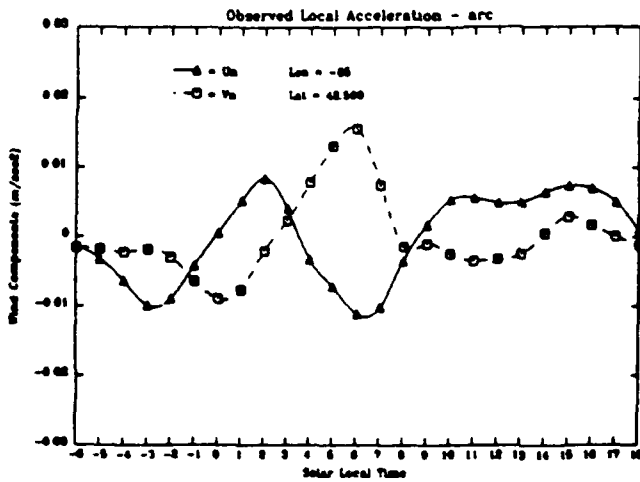
Figure 4.2(b) Observed acceleration of
neutral winds as calculated from
curves above.
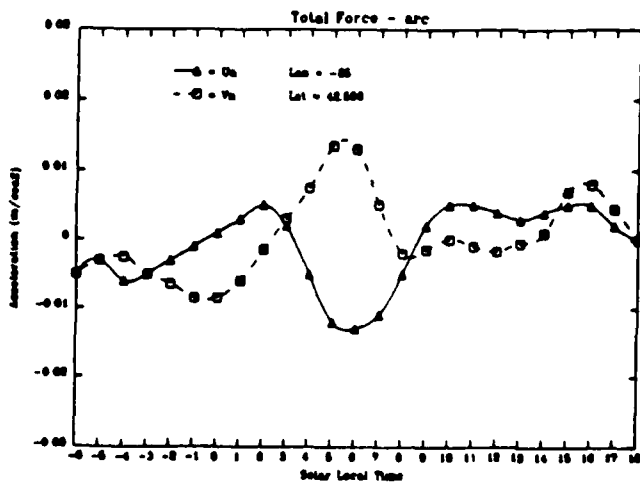
Figure 4.2(c) Total force data taken directly
from archived TGCM data. The
curves should resemble those of fig
4.2(b) above.

Figure 4.2

40
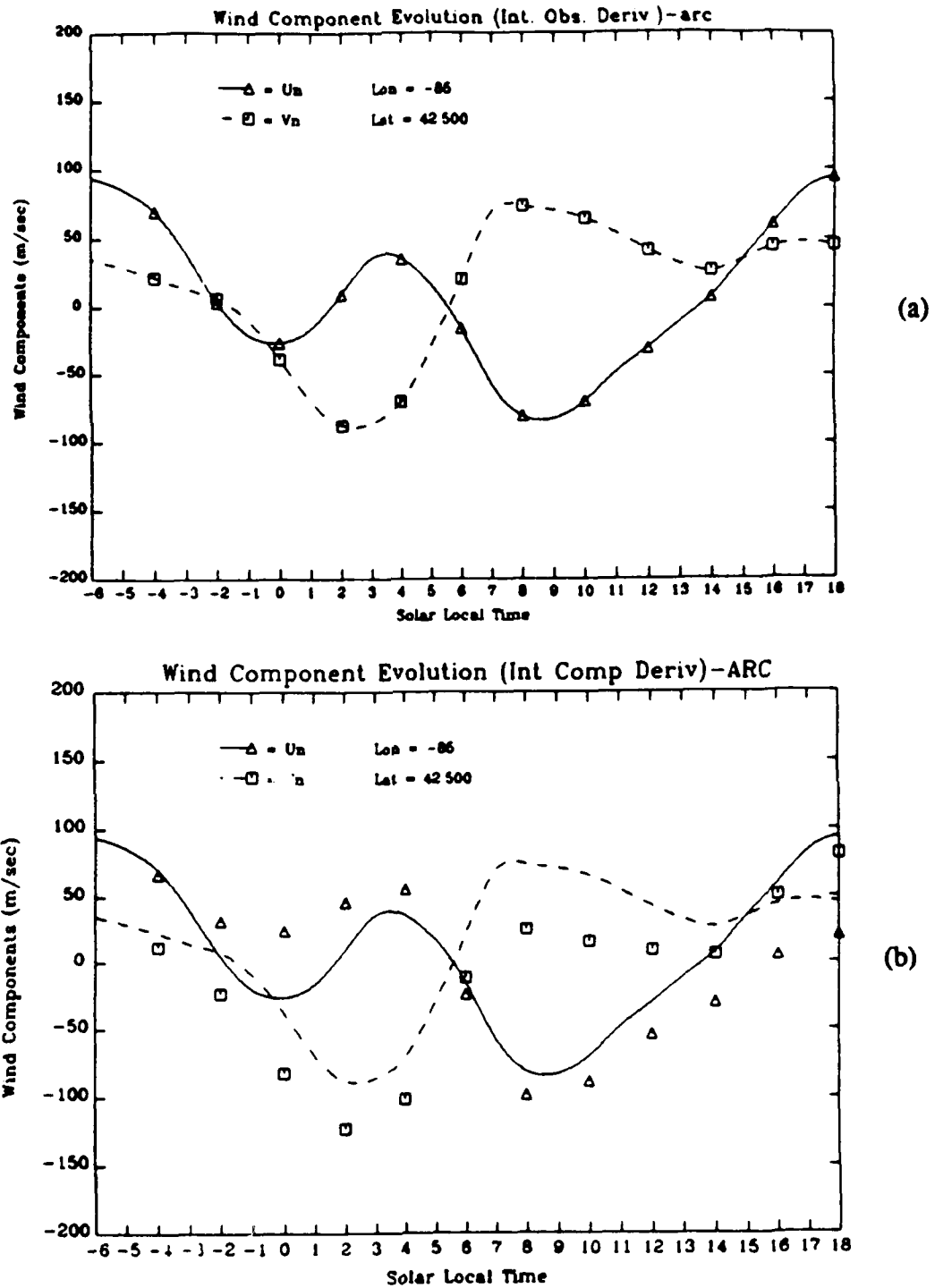
Figure 4.3 Results of performing numerical integration on the observed acceleration (a) and on the total force values (b). Observed winds are plotted with smooth lines, while integrated values are plotted with symbols.

41
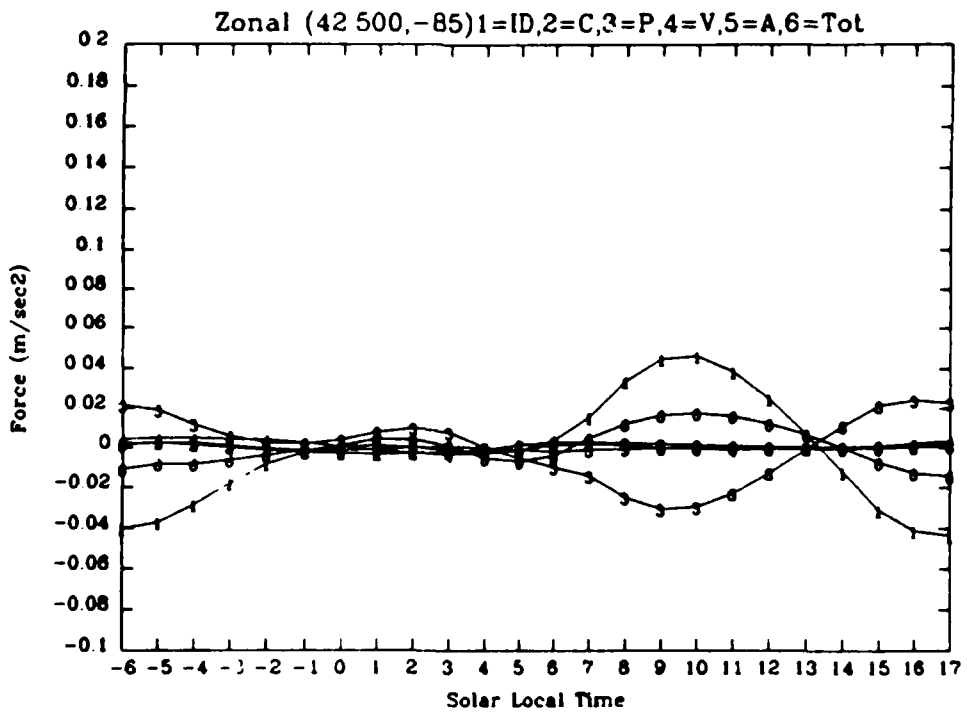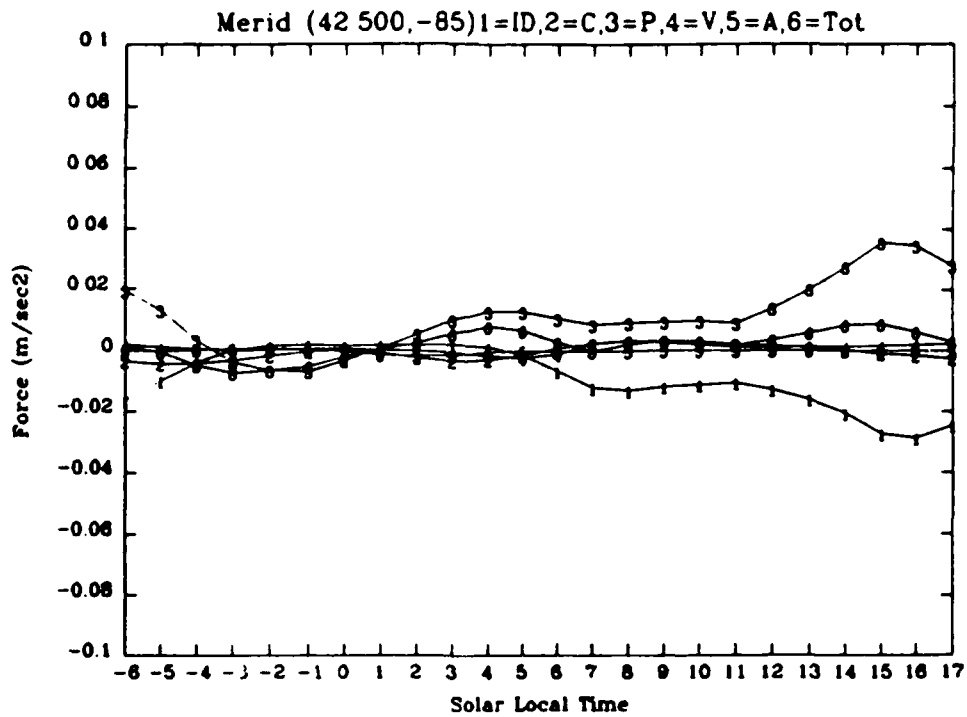
Figure 4.4   Forcing summary for same location as in archived case, but using data
from the TIGCM working data base.
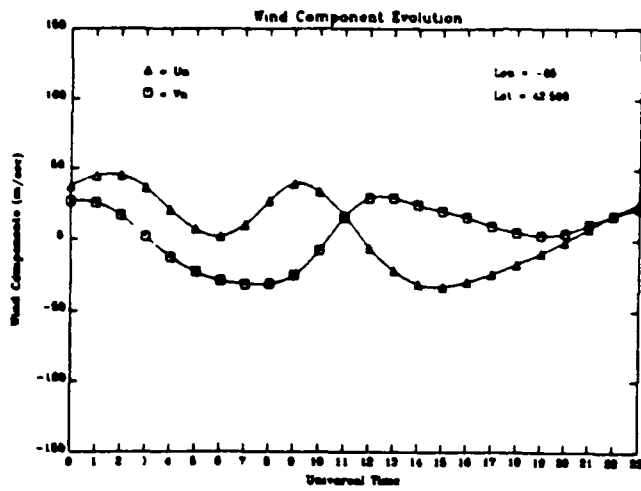
Figure 4.5(a) Diurnal evoultion of neutral
              wind as taken from TIGCM working
              data base (42.5, -85).
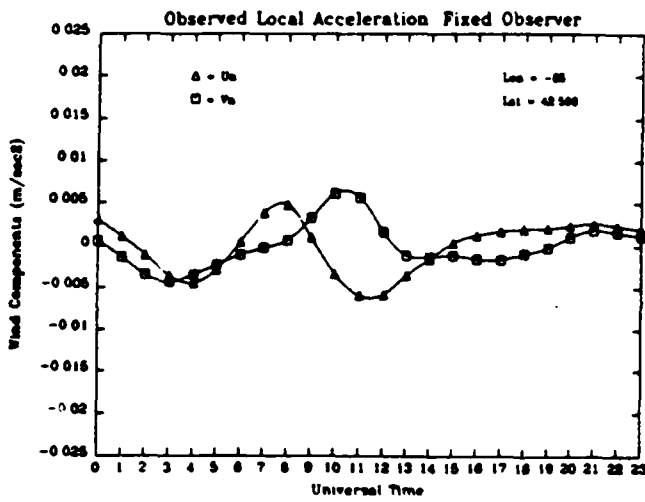
Figure 4.5(b) Measured acceleration of the
              neutral wind depicted above.
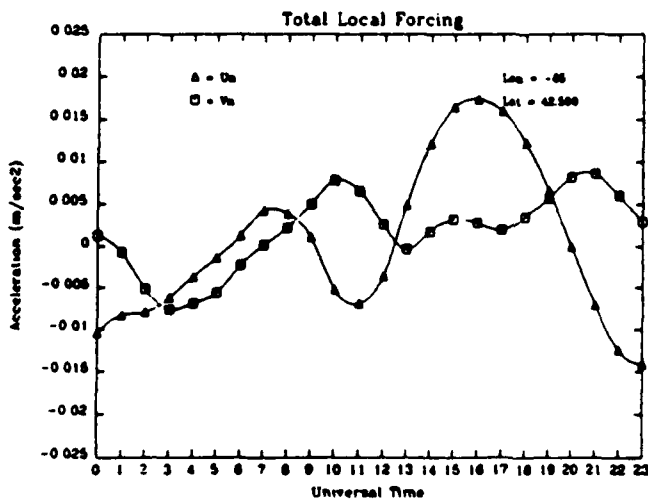
Figure 4.5(c) Total forces acting at same
               locauon as above figures.

Figure 4.5

Wind Component Evolution
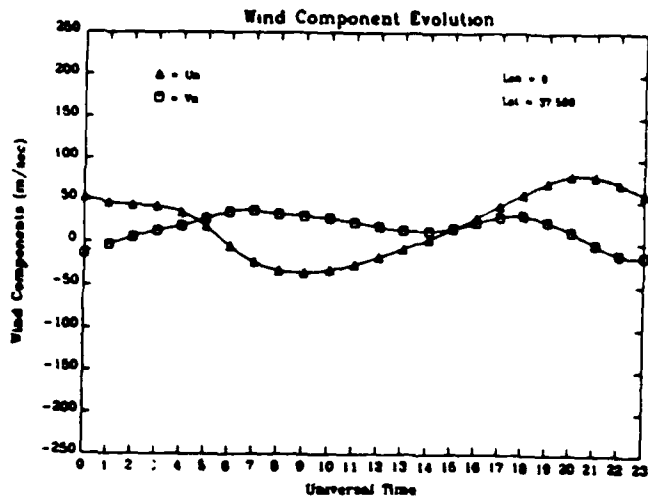
Figure 4.6(a) Diurnal evoultion of neutral
wind as taken from TIGCM working
data base (37.5, 0).

Observed Local Acceleration Fixed Observer
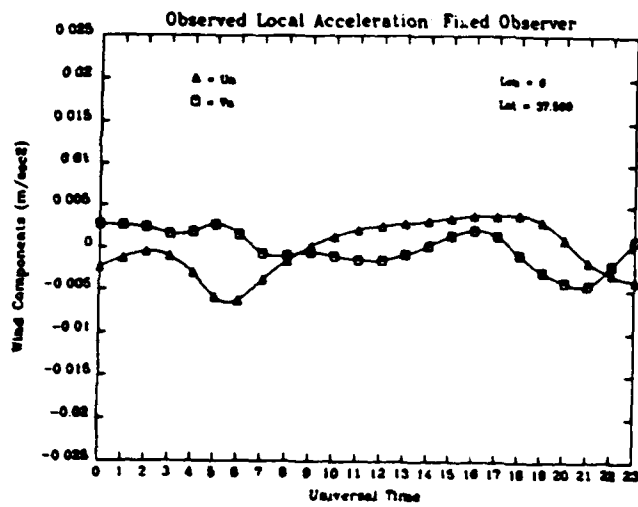
Figure 4.6(b) Measured acceleration of the
neutral wind depicted above.

Total Local Forcing
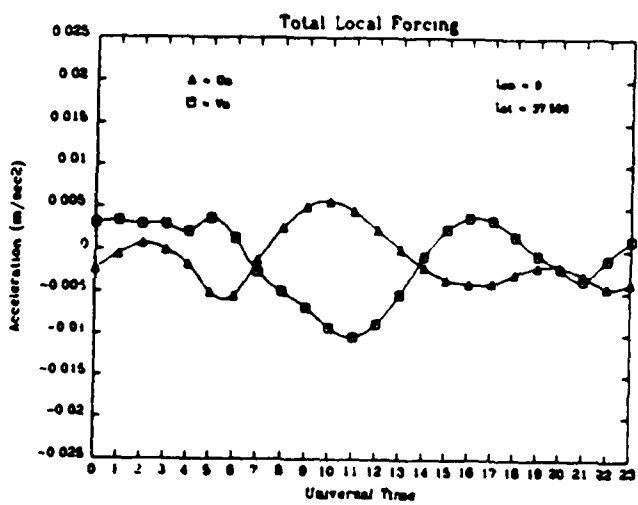
Figure 4.6(c) Total forces acting at same
location as above figures.

Figure 4.6

44
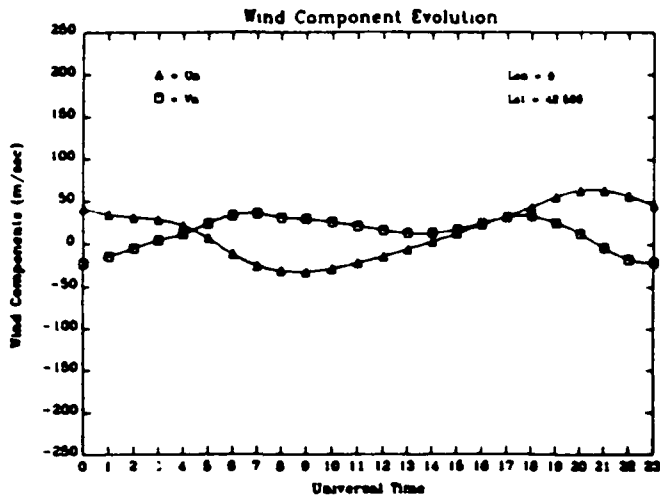
Figure 4.7(a) Diurnal evoultion of neutral
wind as taken from TIGCM working
data base (42.5, 0).
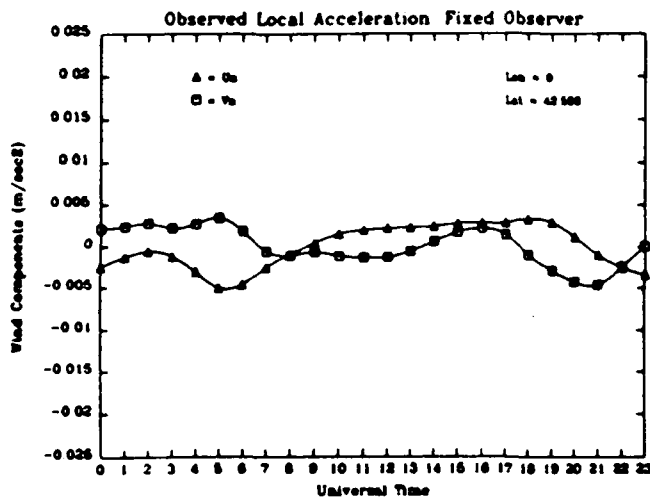
Figure 4.7(b) Measured acceleration of the
neutral wind depicted above.
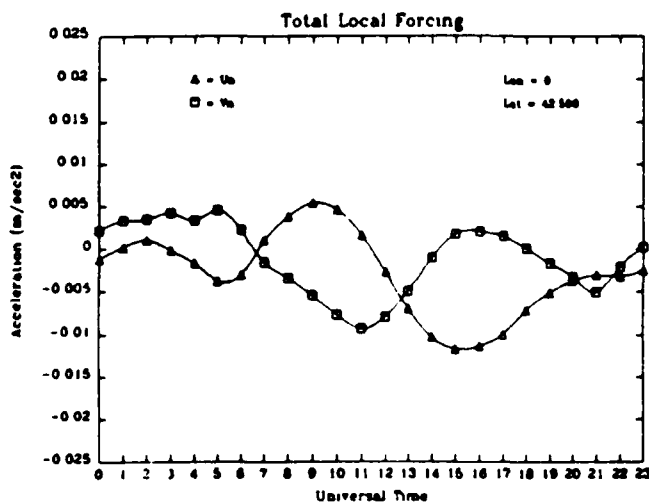
Figure 4.7(c) Total forces acting at same
location as above figures.

Figure 4.7

45
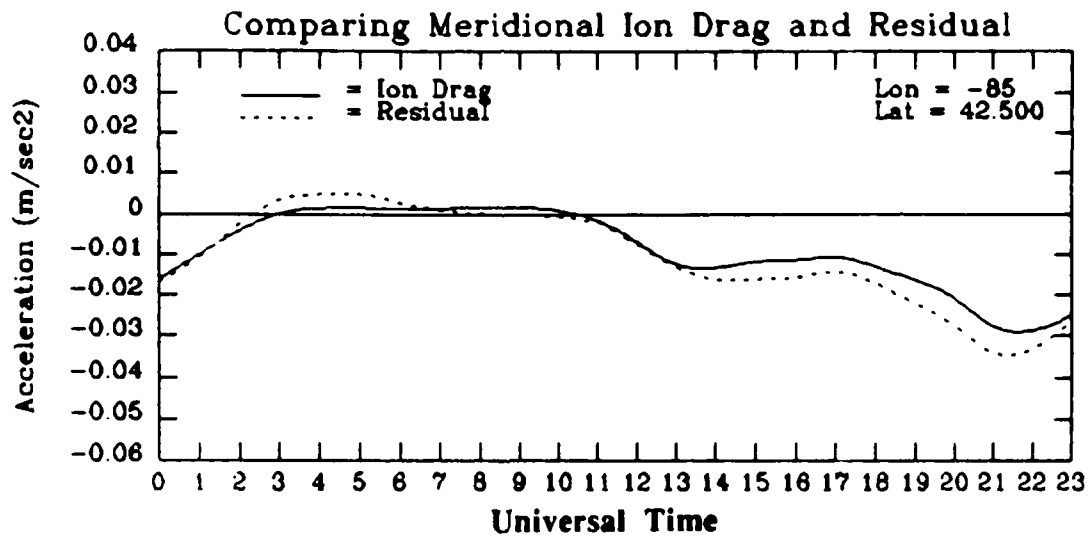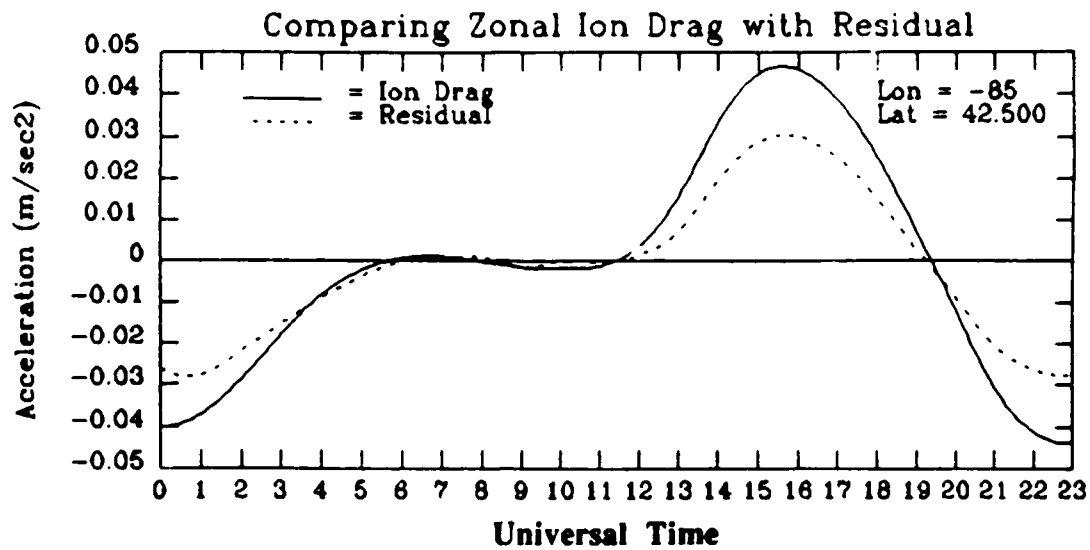
Figure 4.9 Measured ion drag force compared with the ion drag that would provide perfect balance of forces (ie the "residual") for location (-42.5, -85).

46
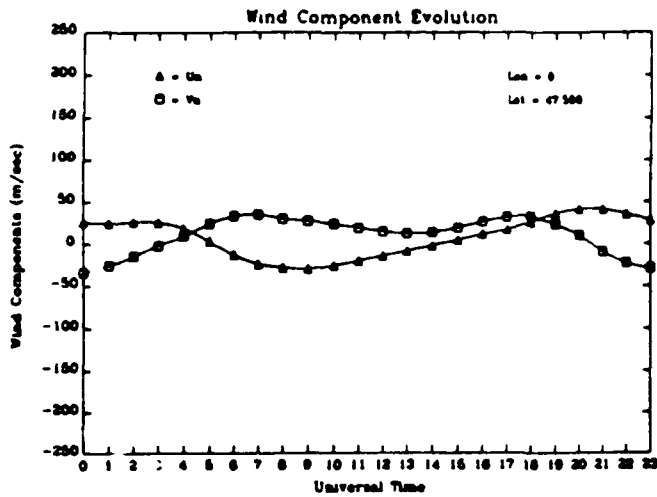
Figure 4.8(a) Diurnal evoultion of neutral wind as taken from TIGCM working data base (47.5, 0).
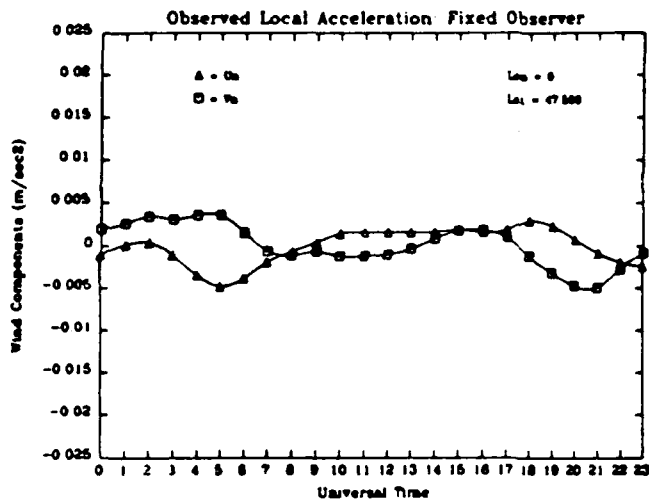
Figure 4.8(b) Measured acceleration of the neutral wind depicted above.
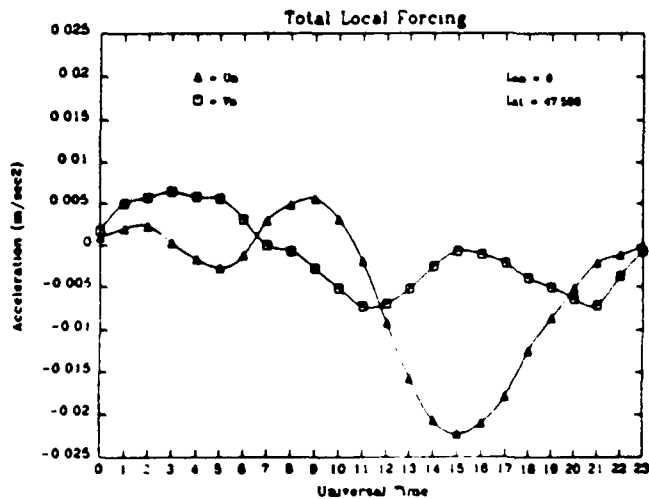
Figure 4.8(c) Total forces acting at same location as above figures.

Figure 4.8

46
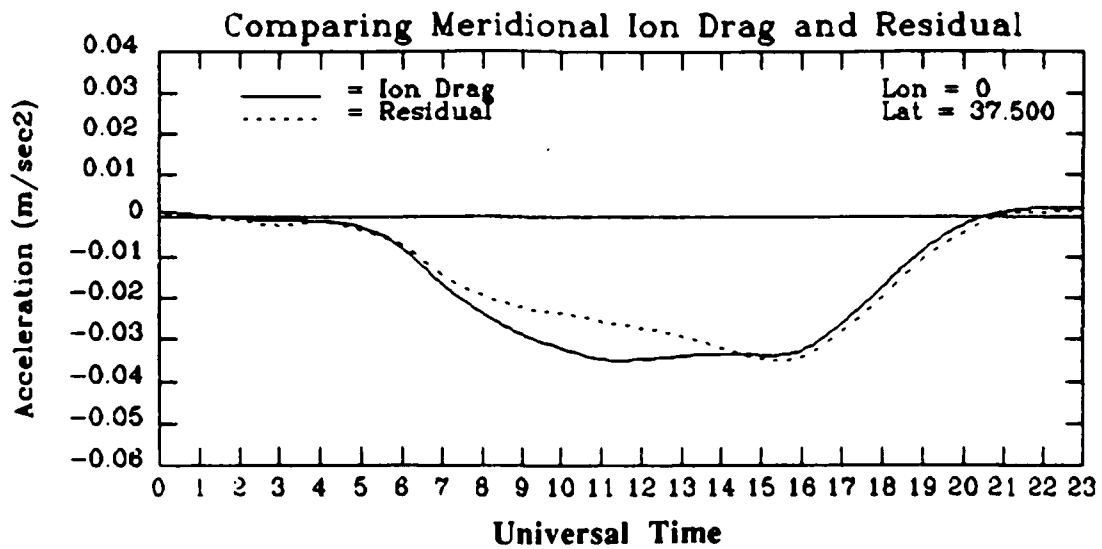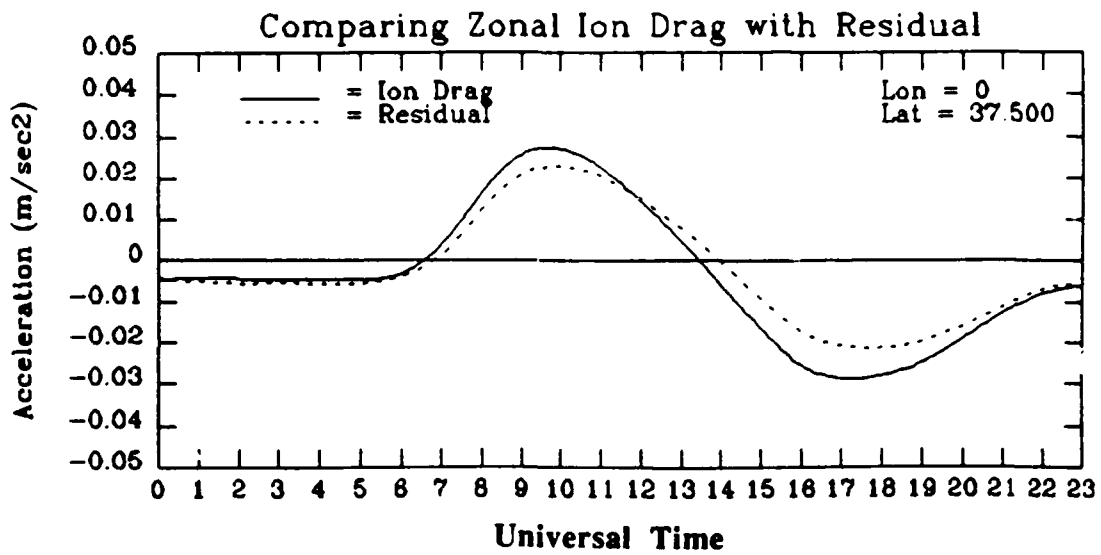
Figure 4.10 Measured ion drag term compared with the residual for location (37.5, 0). Meridional residual is greatest during the sunlit hours.
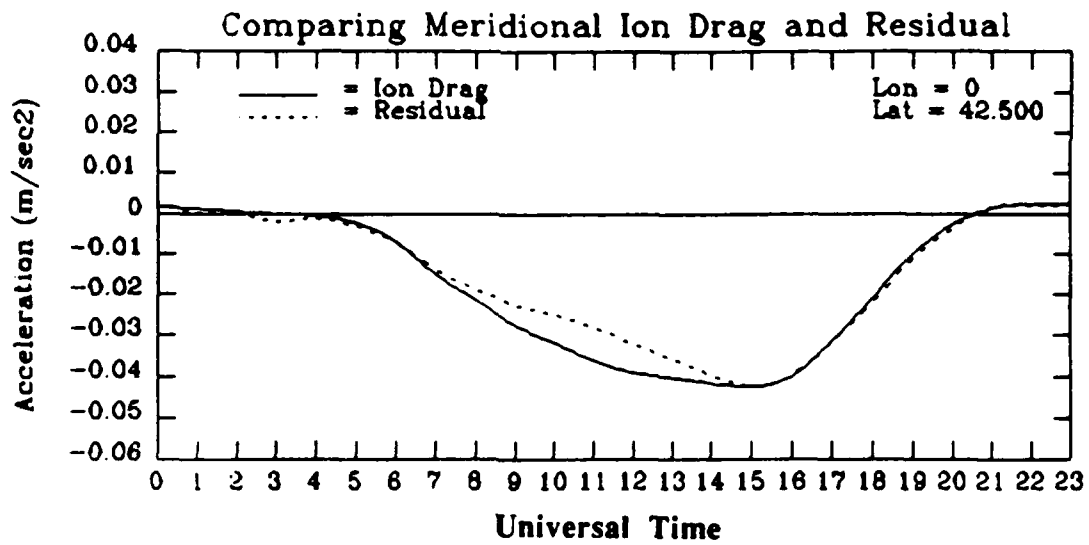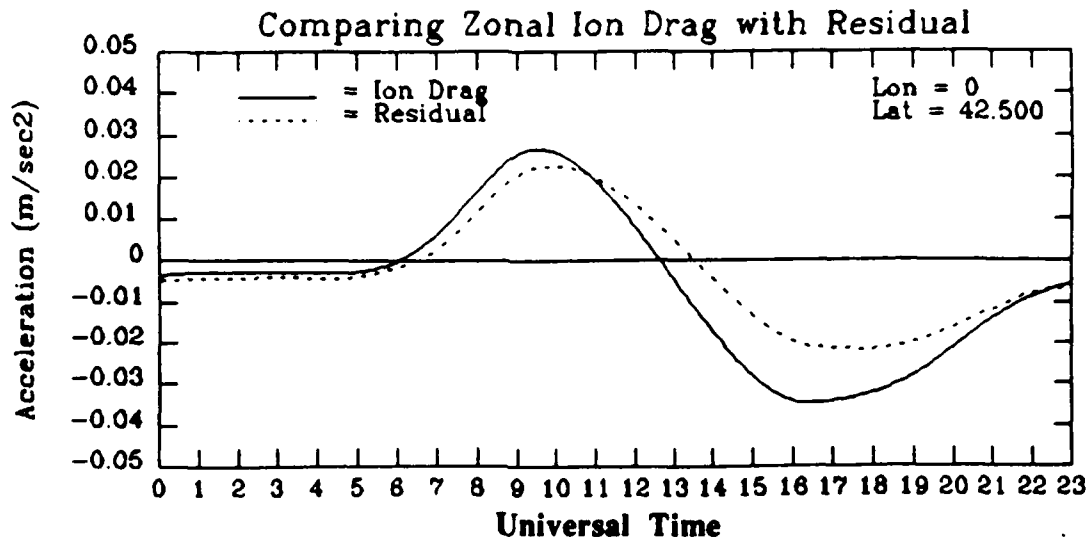
Figure 4.11 Ion drag and residual term compared at (42.5, 0) shows the zonal term with increasing residual magnitude after local noon.
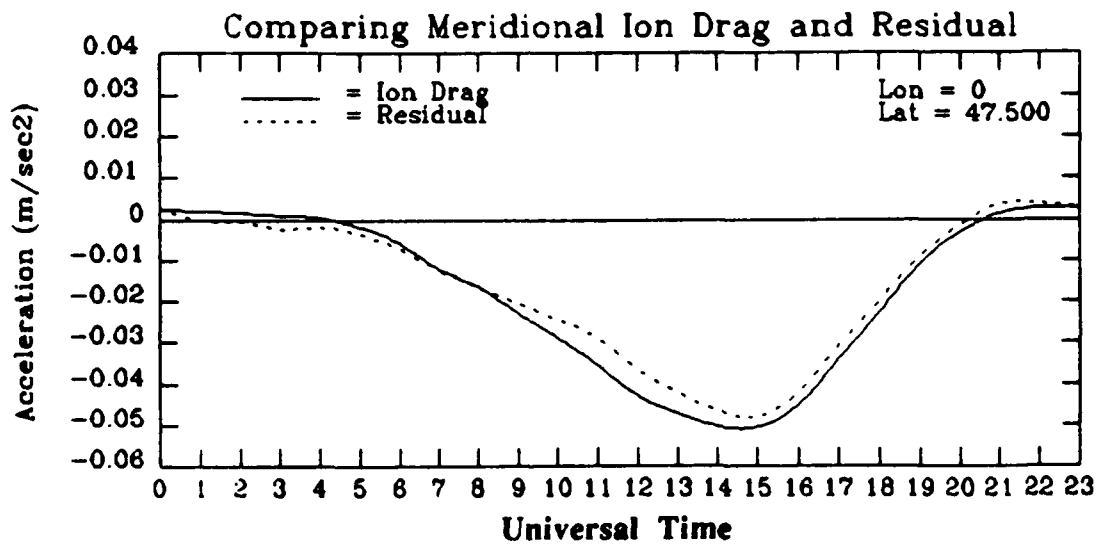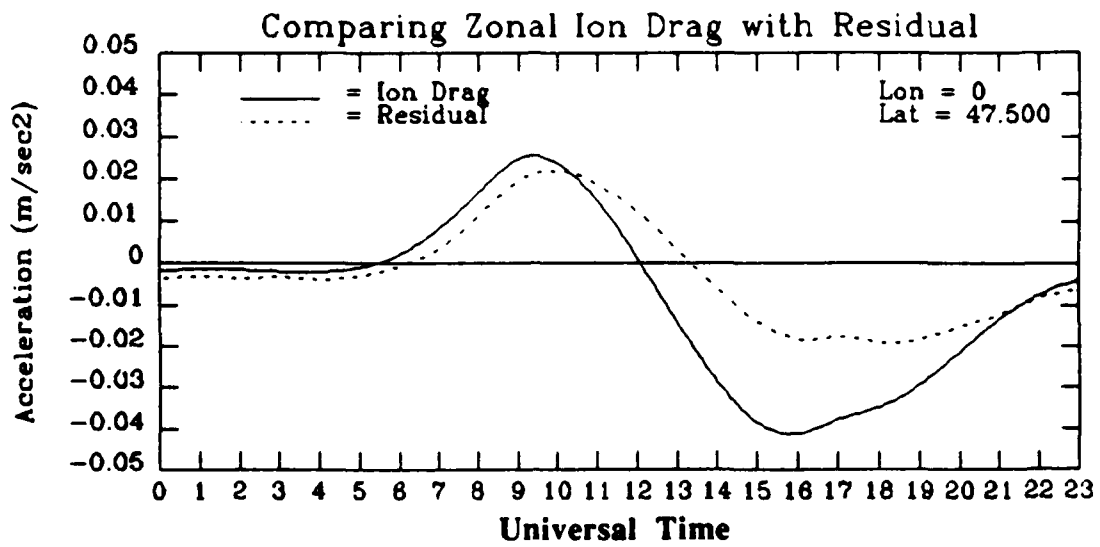
Figure 4.12 Ion drag and residual at (0,47.5) shows the ion drag has at least twice the magnitude of the residual term in the late afternoon. Meridional term as much closer by comparison.
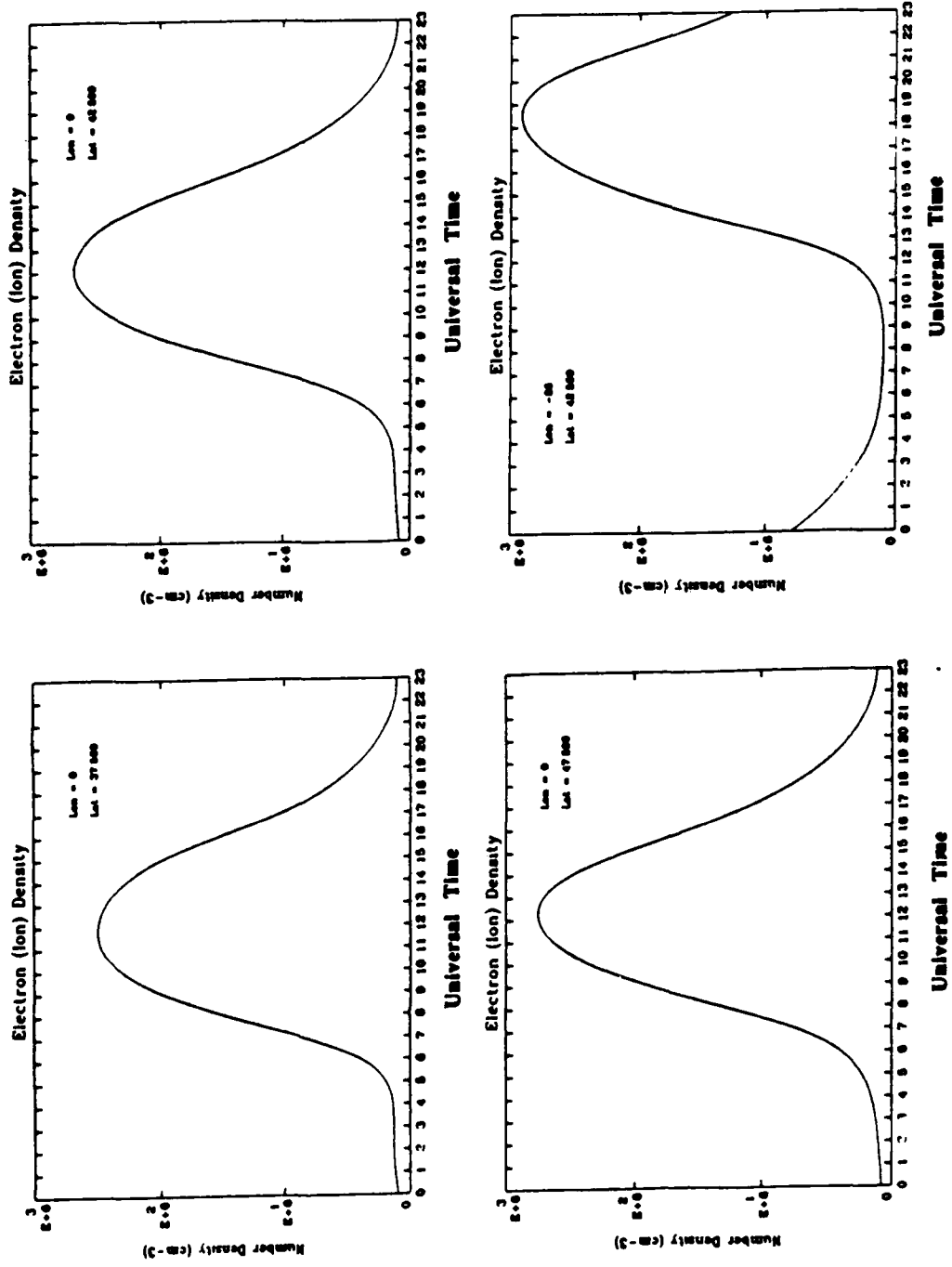
Figure 4.13 Ion density temporal evolution for locations of previous four figures. Ion density increase corresponds separation of residuals from ion drag force in meridional forcing curves.

Simulated Satellite Ground Track

UT = 45

UT = 60

UT = 75

Longitude

Latitude
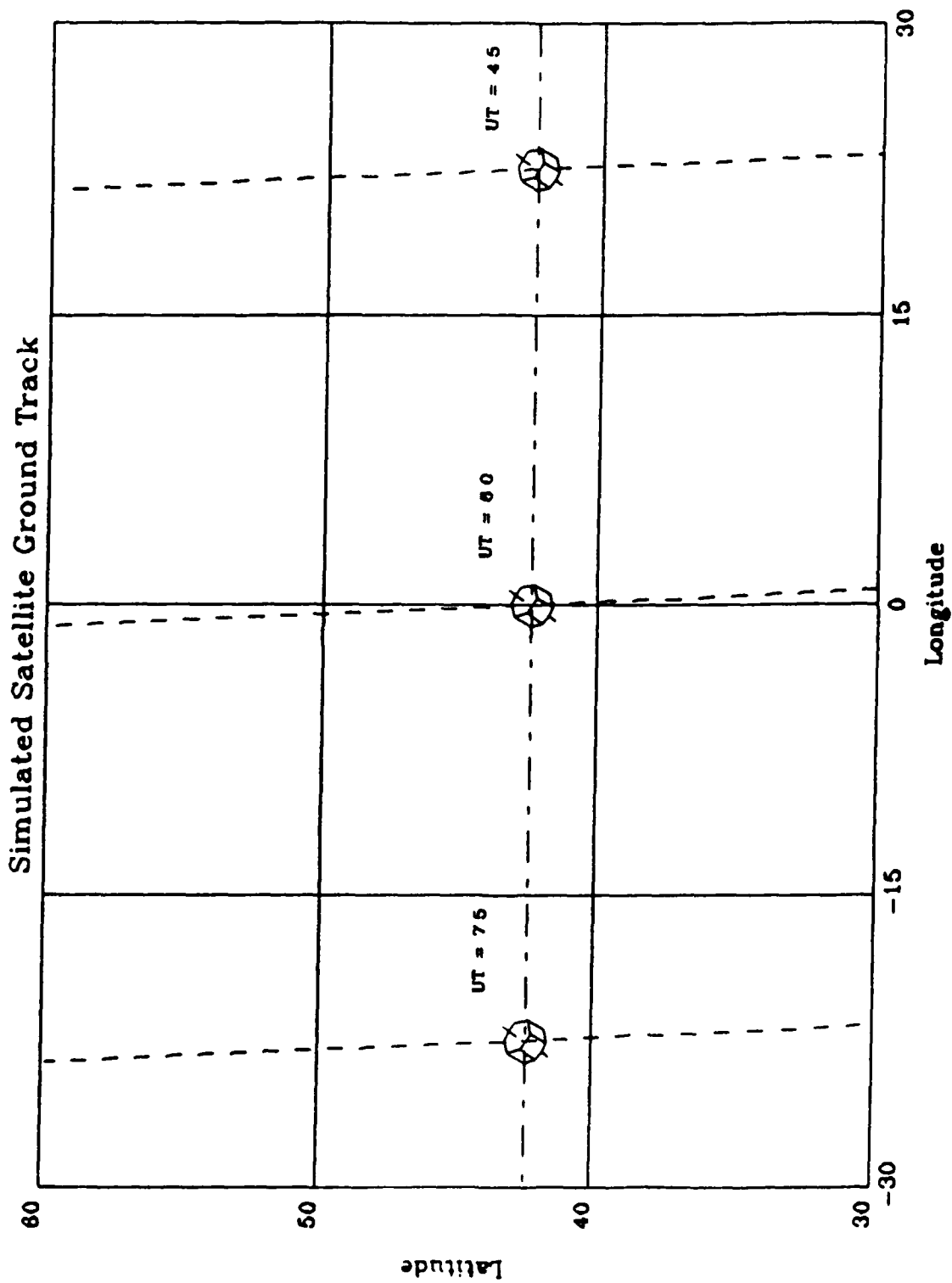
Figure 4.14 Track of three successive orbits of simulated satellite. Movement is from south to north, but includes a westward drift of 22.5° per orbit.
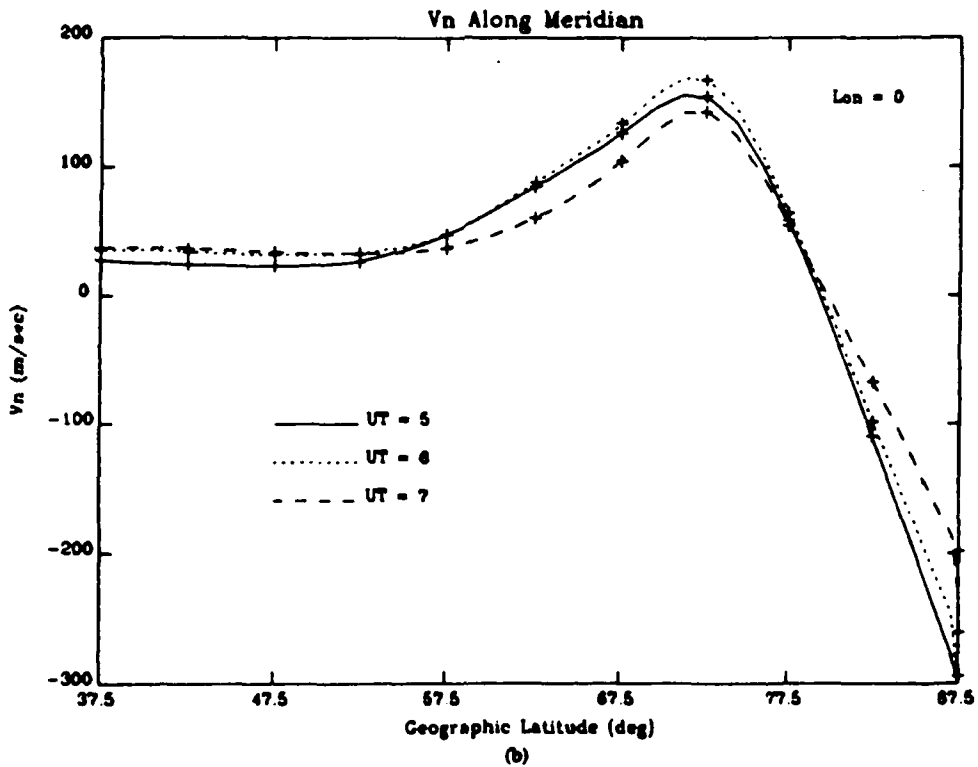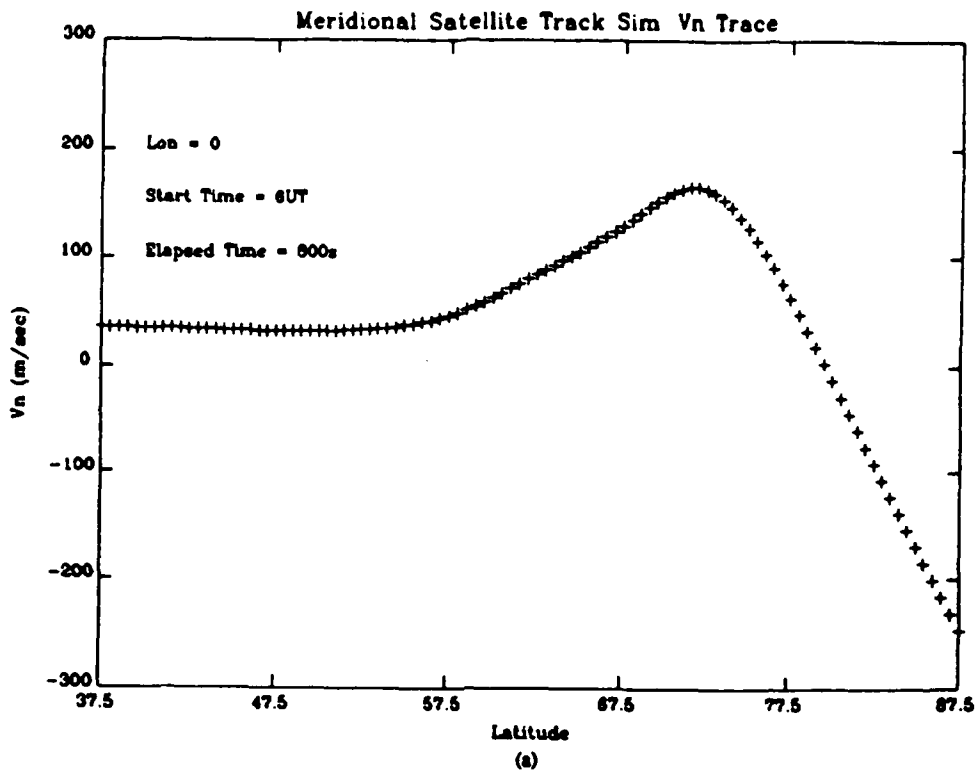
Figure 4.15 Measurements of V_n along the zero degree meridian from a northbound satellite (a) and for three different hourly sets (b). Measurements along track approximate the instantaneous profiles.
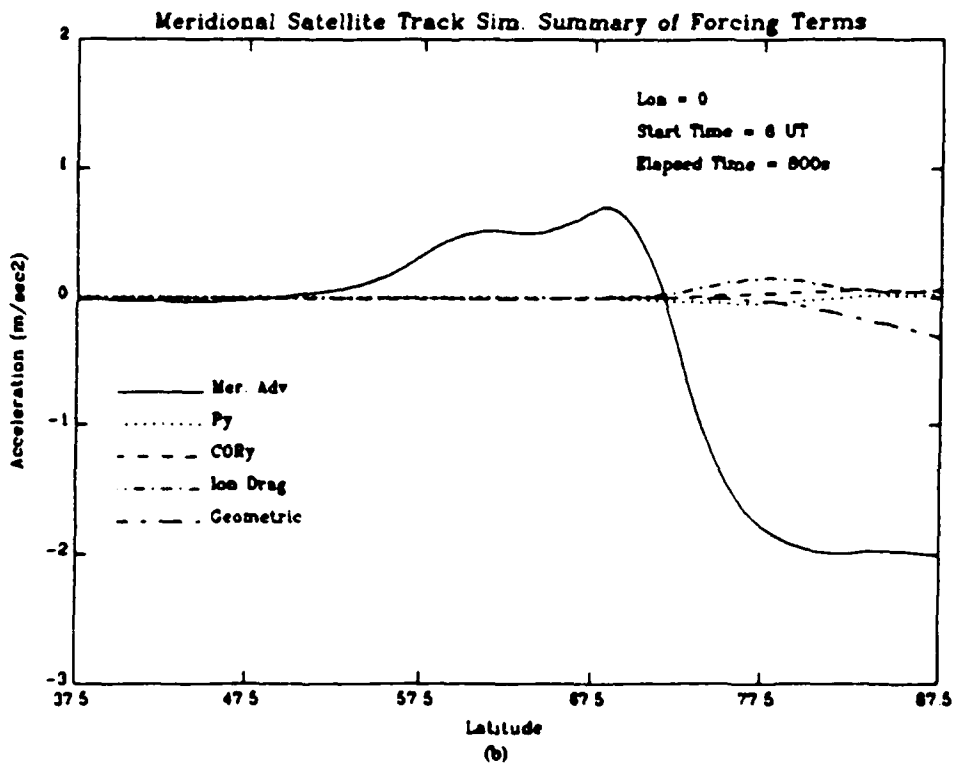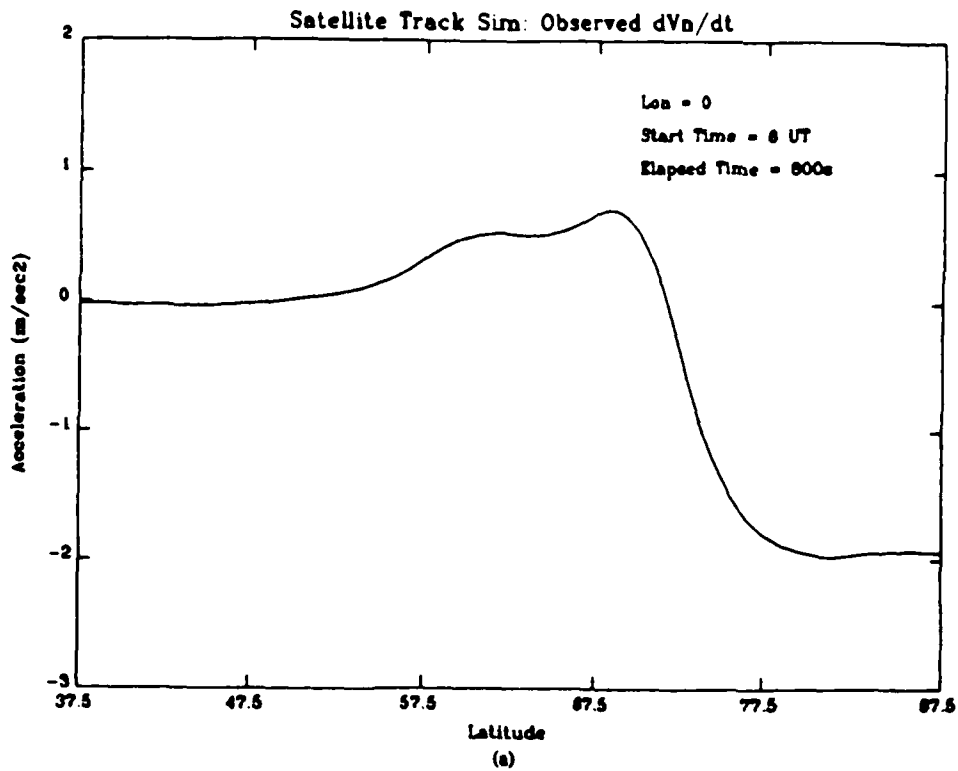
Figure 4.16 Calculation of the instantaneous rate of change of V_n (a) and a composite of calculable forces along satellite track (b). The satellite's orbital speed causes advection term to dominate and closely resemble that in (a).

54
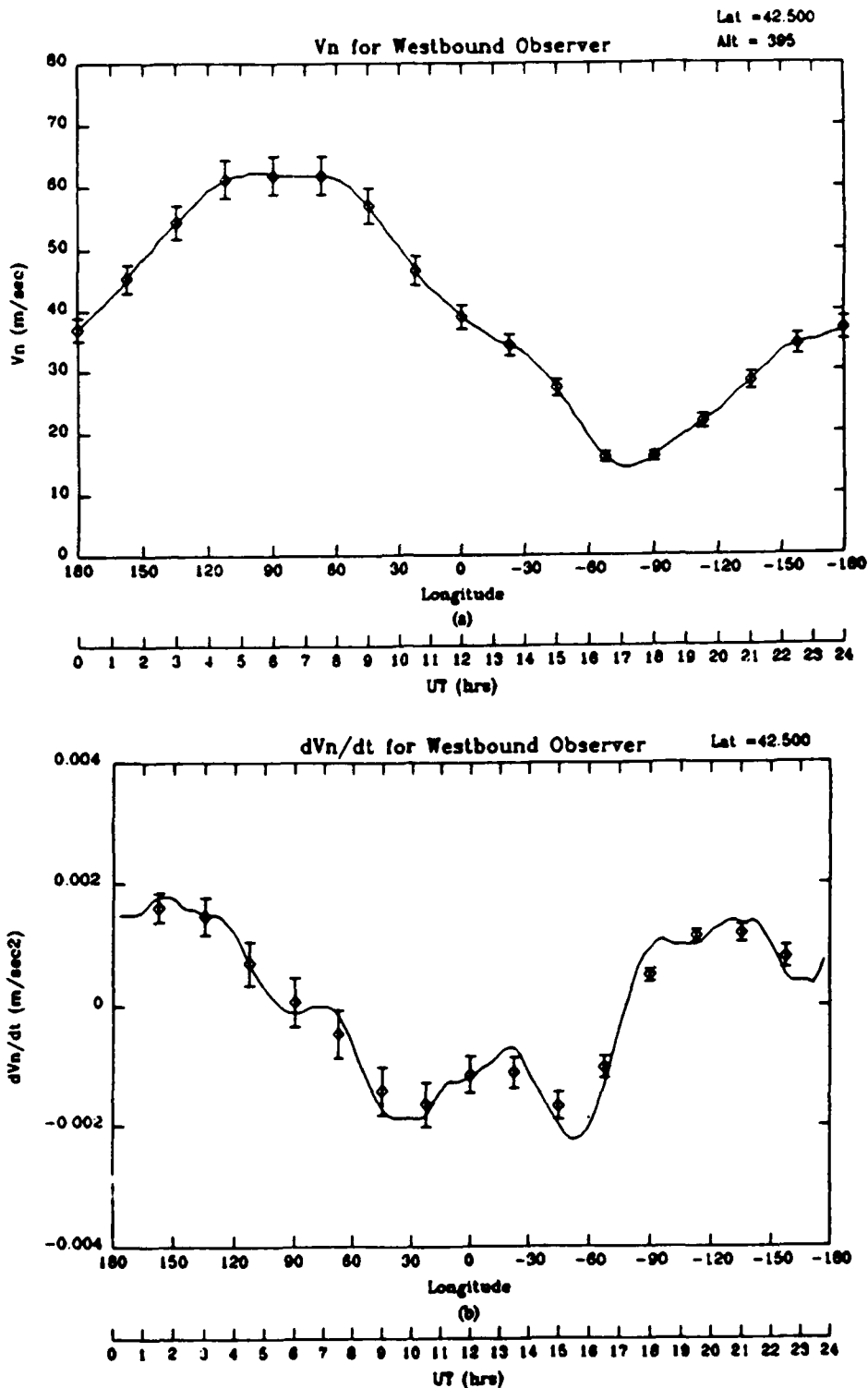
Figure 4.17 V_n and dV_n/dt for a hypothetical westbound observer. Plotting symbols are drawn 1.5 hrs. Solid lines in (b) are exact derivatives while plotting symbols are centered difference approximations. Five per cent relative error bars in (a) give rise to computational errors in (b).

55
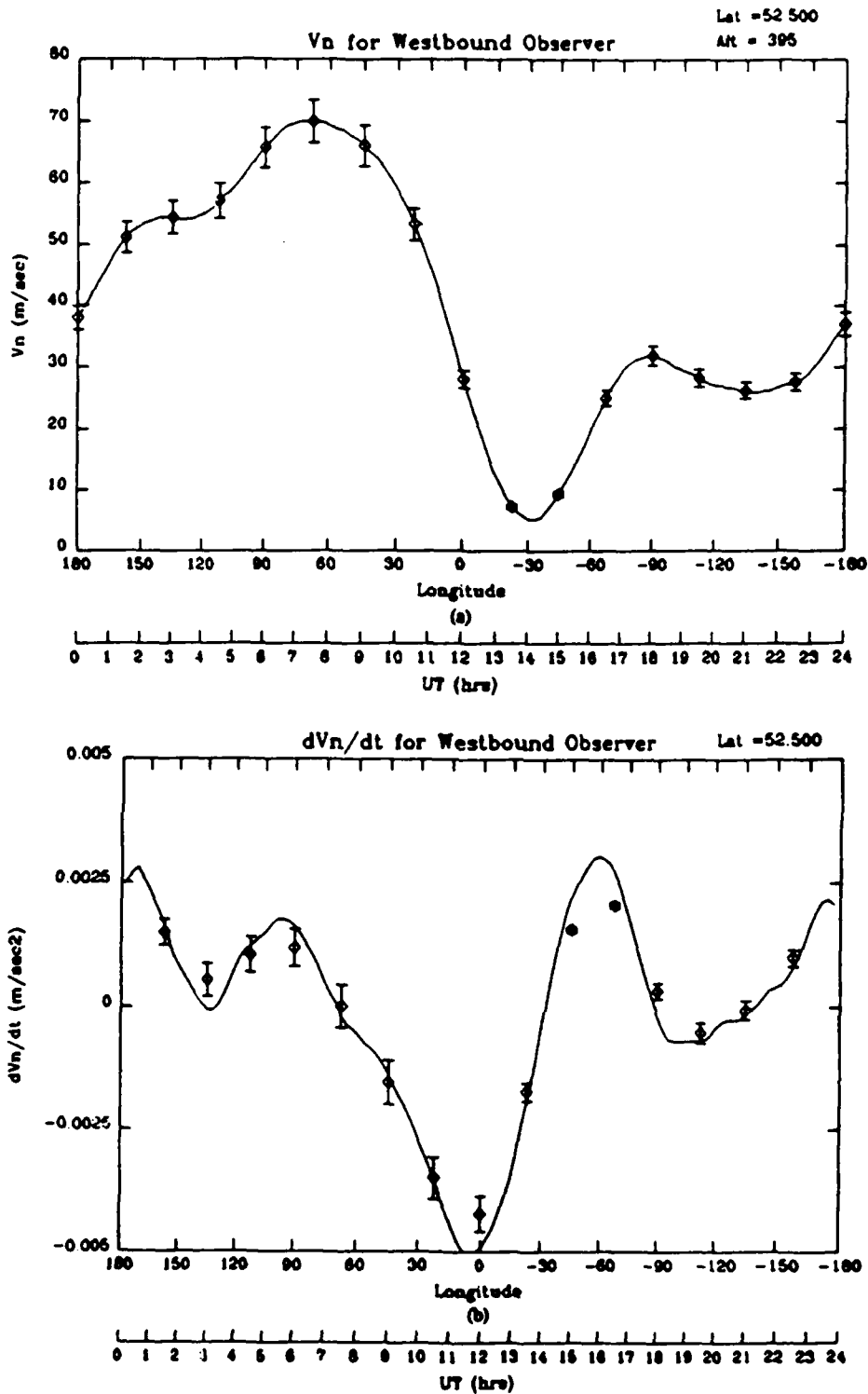
Figure 4.18 Same depiction of V_n and dV_n/dt for a high latitude. Larger variations in V_n lead to greater accelerations. Uncertainty in calculating acceleration by centered differencing is on the same order as the uncertainty resulting from the measurements.

5 6
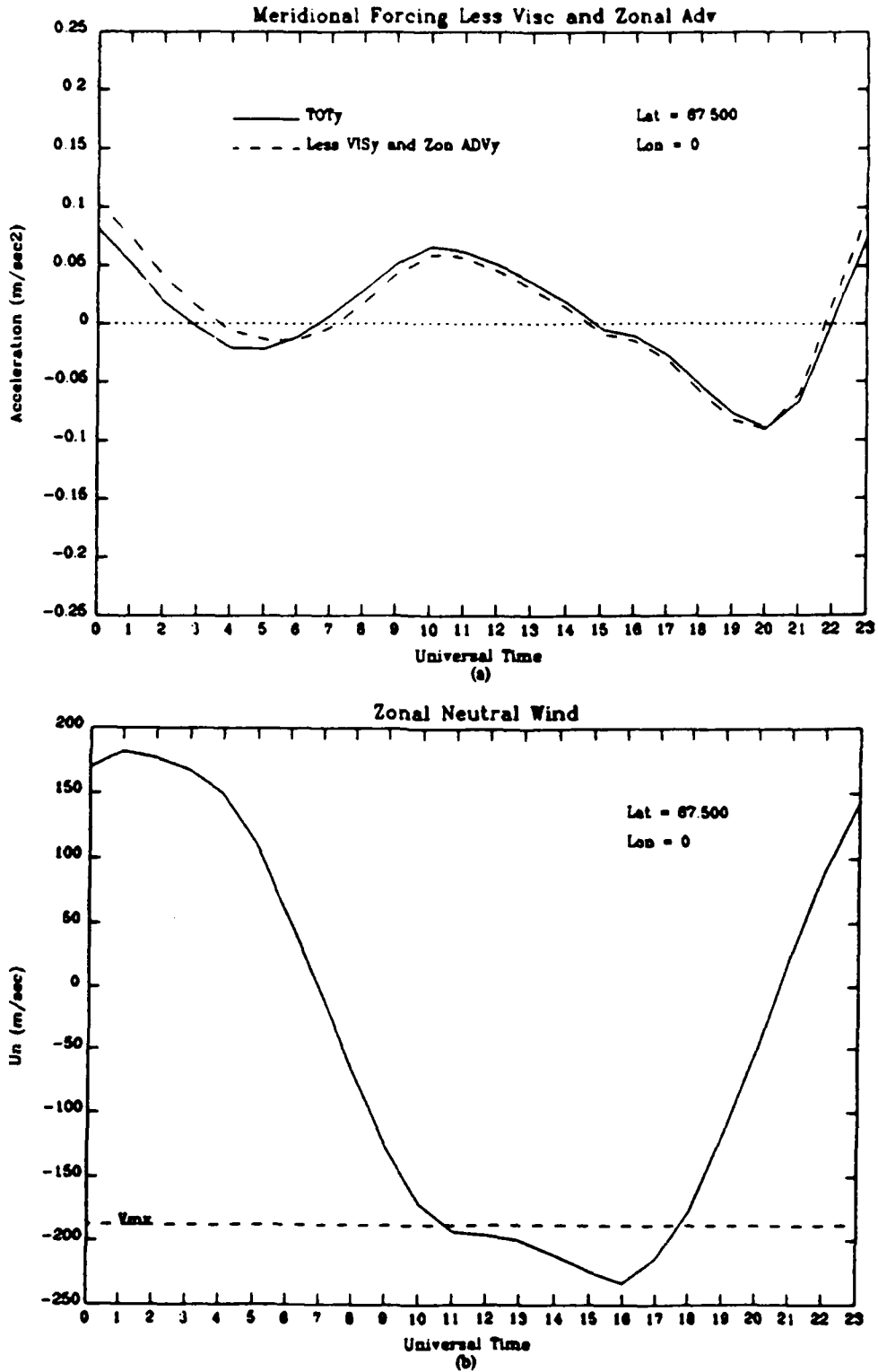
Figure 4.19 Comparison of the total meridional forcing to that excluding the viscous drag and zonal advection (a). Agreement is best where zonal wind speed approaches the satellite westward drift velocity (b).

57
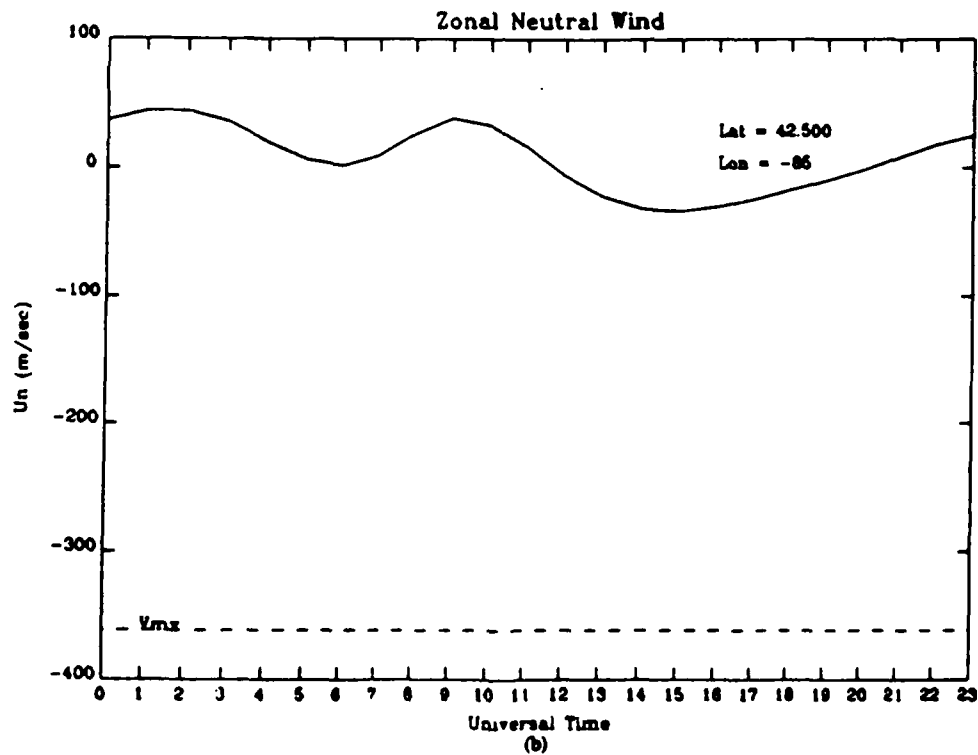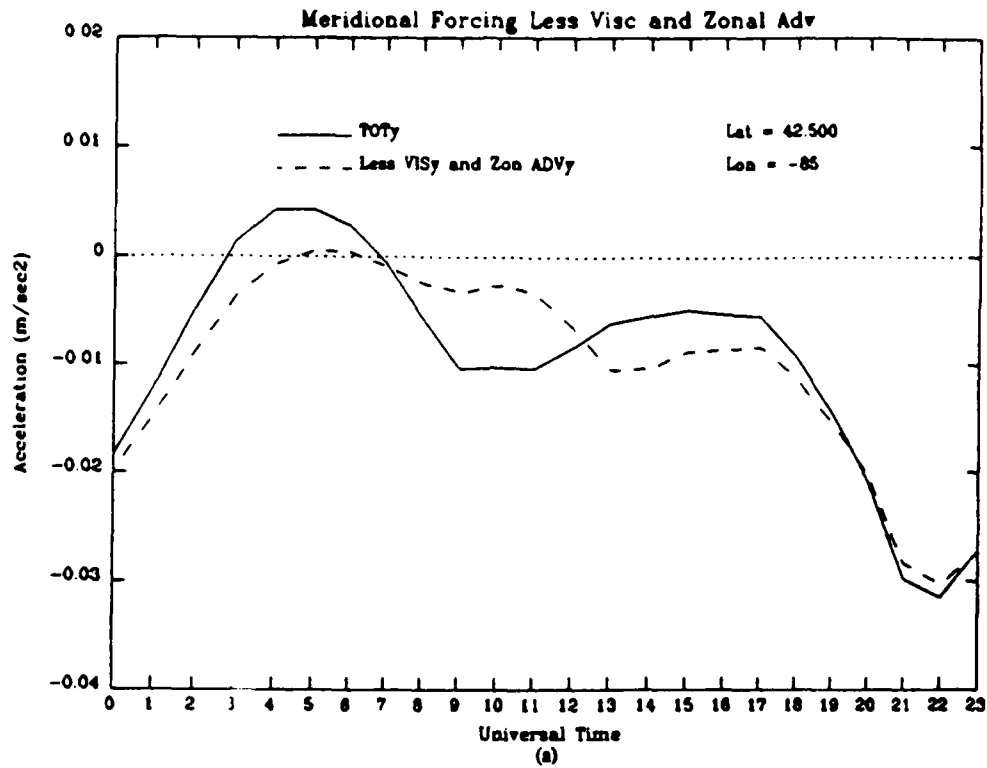
Figure 4.20 Same comparison as in figure 4.19 showing that zonal wind speed has
a noticeable albeit reduced effect when zonal winds are light.

58
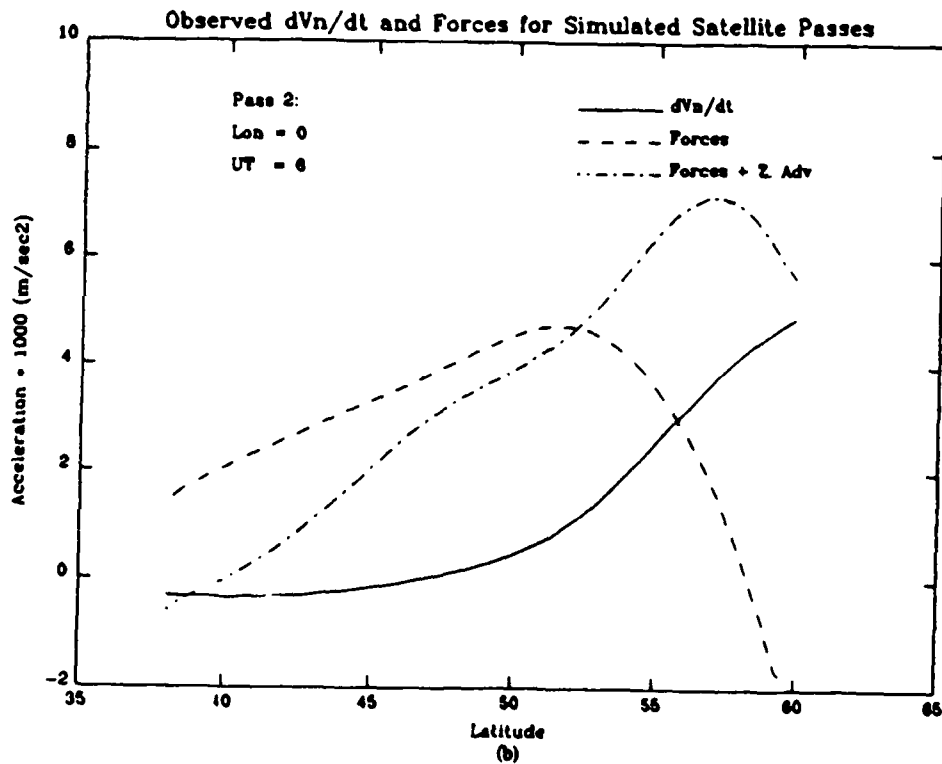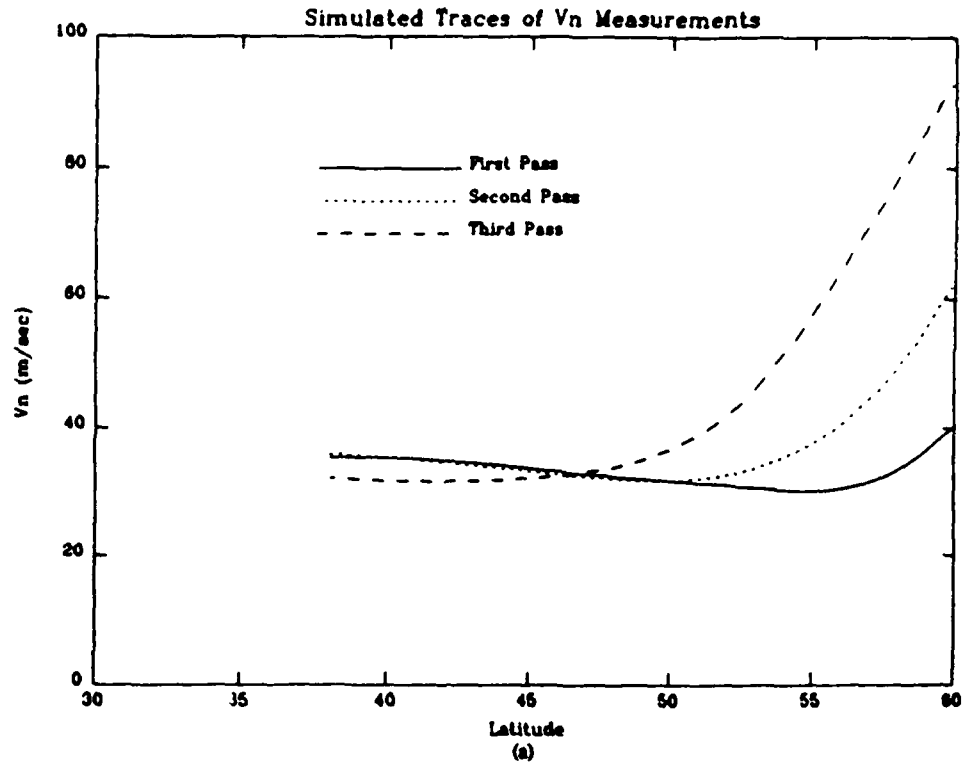
Figure 4.21 Results of constant latitude experiment showing Vn along the three orbital bands (a). Acceleration between the first and third orbits shows the effect of increasing forcing with latitude (b), but is far below total forcing curve. Effect of restoring zonal advection term also shown.
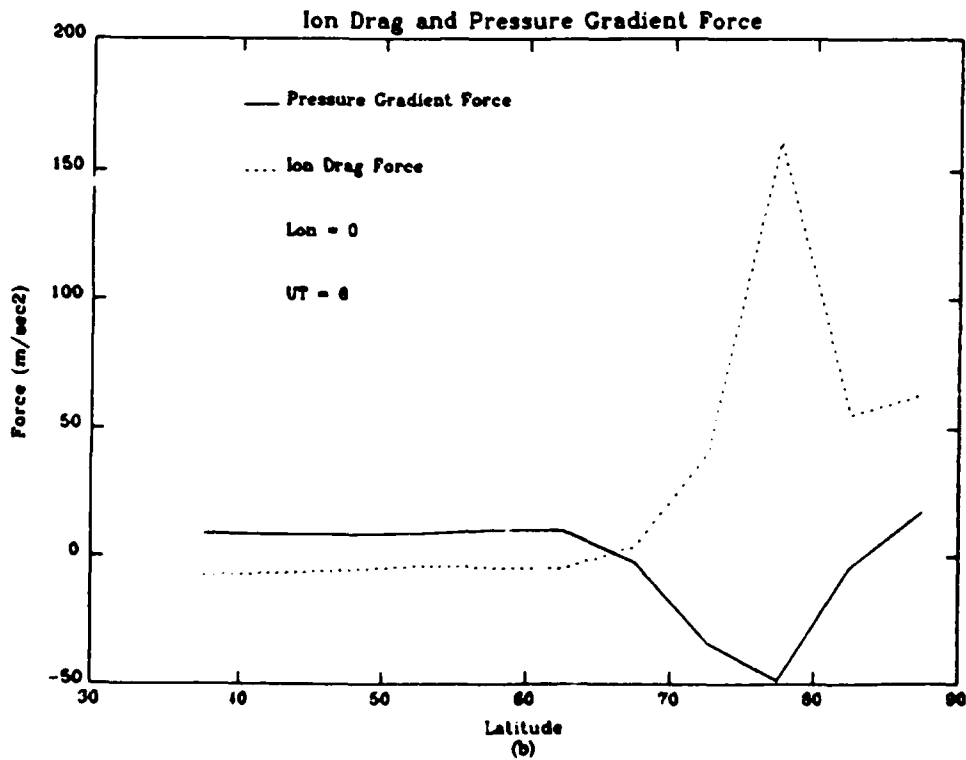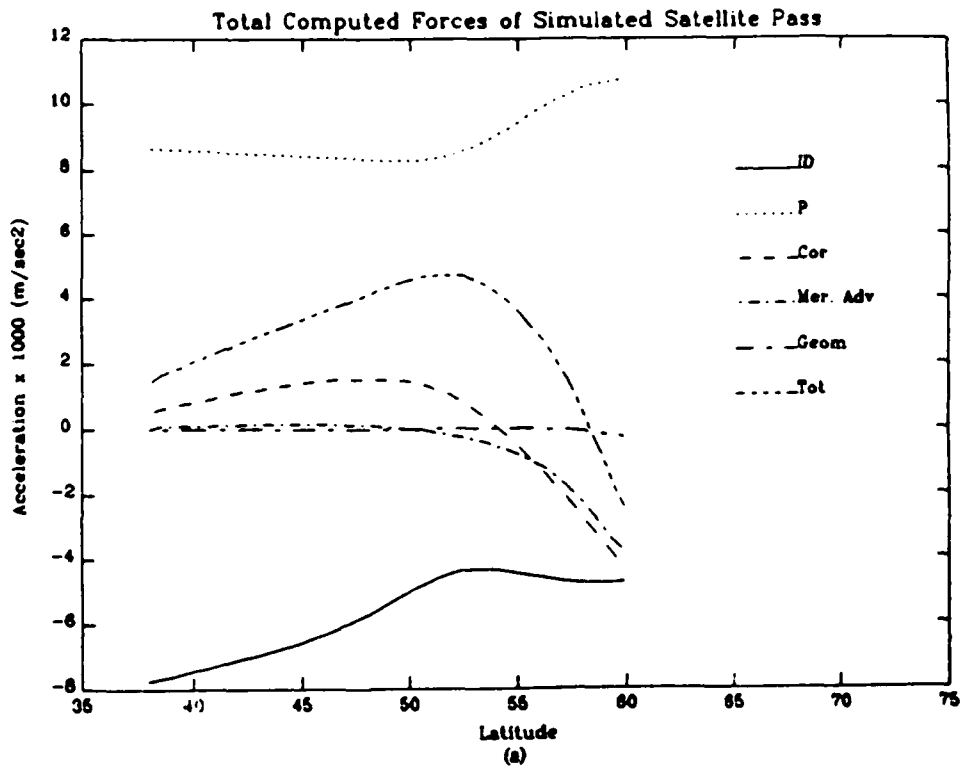
Figure 4.22 Summary of forcing along second simulated orbit (a). Pressure gradient force and ion drag force along entire meridian (b) show familiar opposing characteristics.

60

Satellite Orbit Geometry
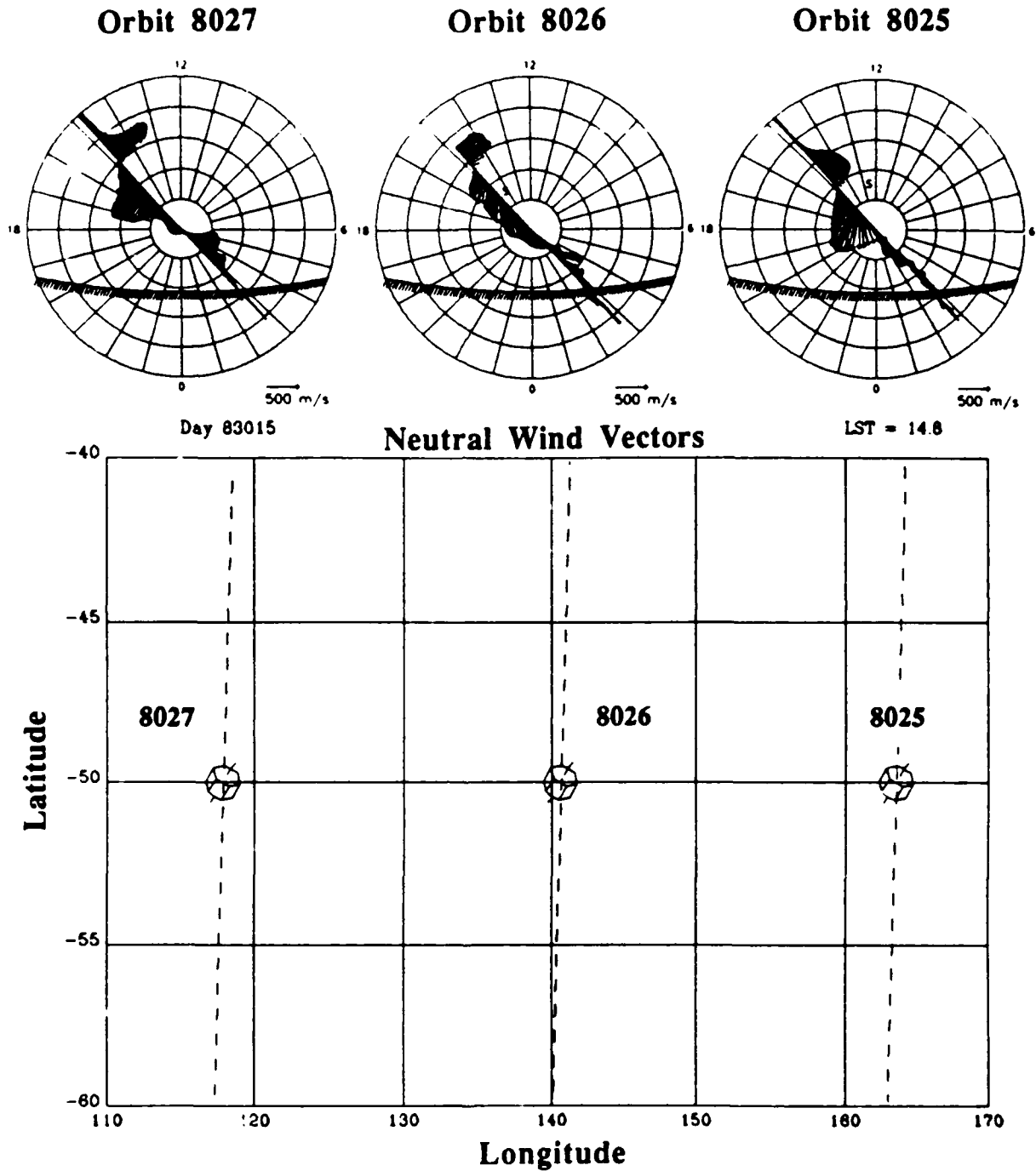
Figure 4.23 Satellite geometry featuring neutral wind vectors along the three orbits.

Tabulated Results from DE2 Satellite Data Analysis

UT	LAT	LON	ALT	LST	V1	Un	Vn1	Vn2	Vn3	dVn/dt	TOTy	Vdrag	PY	Vcor	MAY
19919.	-40.00	141.32	389.94	14.80	77.	-46.	-16.	15.	19.	0.315E-02	-0.119E-01	0.616E-01	-0.693E-01	-0.430E-02	-0.165E-03
19927.	-40.50	141.28	389.65	14.80	80.	-47.	-22.	16.	16.	0.350E-02	-0.147E-01	0.633E-01	-0.737E-01	-0.442E-02	-0.141E-03
19934.	-41.00	141.26	389.36	14.80	83.	-48.	-26.	16.	16.	0.347E-02	-0.957E-02	0.644E-01	-0.696E-01	-0.461E-02	-0.733E-04
19942.	-41.50	141.23	389.09	14.80	84.	-49.	-28.	16.	12.	0.308E-02	0.155E-01	0.646E-01	-0.447E-01	-0.476E-02	-0.284E-04
19950.	-42.00	141.20	388.71	14.80	85.	-49.	-29.	16.	6.	0.259E-02	0.435E-01	0.650E-01	-0.171E-01	-0.473E-02	-0.336E-04
19958.	-42.50	141.16	388.38	14.80	84.	-46.	-29.	16.	0.	0.222E-02	0.550E-01	0.638E-01	0.218E-02	-0.453E-02	-0.746E-04
19965.	-43.00	141.13	388.12	14.80	83.	-44.	-29.	17.	-5.	0.208E-02	0.598E-01	0.611E-01	0.869E-02	-0.440E-02	-0.114E-03
19973.	-43.50	141.10	387.75	14.80	83.	-45.	-29.	17.	-7.	0.210E-02	0.654E-01	0.618E-01	-0.135E-01	-0.447E-02	-0.133E-03
19981.	-44.00	141.07	387.42	14.80	82.	-45.	-28.	18.	-6.	0.215E-02	0.410E-01	0.590E-01	-0.763E-01	-0.459E-02	-0.160E-03
19988.	-44.50	141.04	387.15	14.80	80.	-45.	-27.	18.	-5.	0.212E-02	-0.254E-01	0.554E-01	-0.137E+00	-0.458E-02	-0.240E-03
19996.	-45.00	141.00	386.80	14.80	79.	-43.	-26.	19.	-4.	0.200E-02	-0.886E-01	0.528E-01	-0.143E+00	-0.446E-02	-0.415E-03
20004.	-45.50	140.98	386.46	14.80	80.	-42.	-25.	20.	-4.	0.180E-02	-0.958E-01	0.516E-01	-0.945E-01	-0.431E-02	-0.649E-03
20011.	-46.00	140.95	386.14	14.80	82.	-39.	-26.	25.	-5.	0.155E-02	-0.488E-01	0.504E-01	-0.406E-01	-0.408E-02	-0.867E-03
20019.	-46.50	140.92	385.74	14.80	83.	-36.	-27.	23.	-8.	0.129E-02	0.259E-02	0.480E-01	-0.152E-01	-0.380E-02	-0.986E-03
20027.	-47.00	140.89	385.39	14.80	83.	-35.	-28.	28.	-12.	0.106E-02	0.256E-01	0.453E-01	-0.134E-01	-0.376E-02	-0.907E-03
20035.	-47.50	140.85	385.08	14.80	85.	-38.	-29.	30.	-16.	0.817E-03	0.275E-01	0.454E-01	-0.245E-01	-0.405E-02	-0.594E-03
20042.	-48.00	140.82	384.68	14.80	90.	-42.	-30.	30.	-20.	0.488E-03	0.195E-01	0.483E-01	-0.456E-01	-0.454E-02	-0.924E-04
20050.	-48.50	140.79	384.30	14.80	96.	-46.	-30.	30.	-24.	0.641E-04	-0.224E-01	0.522E-01	-0.704E-01	-0.502E-02	0.355E-03
20058.	-49.00	140.76	383.91	14.80	98.	-51.	-29.	28.	-29.	-0.500E-03	-0.207E-01	0.542E-01	-0.840E-01	-0.562E-02	0.596E-03
20065.	-49.50	140.73	383.54	14.80	94.	-59.	-28.	27.	-34.	-0.106E-02	-0.379E-01	0.513E-01	-0.861E-01	-0.656E-02	0.737E-03
20073.	-50.00	140.70	383.25	14.80	89.	-70.	-27.	25.	-40.	-0.162E-02	-0.460E-01	0.482E-01	-0.924E-01	-0.783E-02	0.904E-03
20081.	-50.50	140.67	382.86	14.80	84.	-84.	-27.	23.	-45.	-0.202E-02	-0.536E-01	0.458E-01	-0.110E+00	-0.940E-02	0.109E-02
20088.	-51.00	140.64	382.47	14.80	82.	-101.	-29.	20.	-49.	-0.228E-02	-0.726E-01	0.460E-01	-0.136E+00	-0.115E-01	0.910E-03
20096.	-51.50	140.61	381.99	14.80	74.	-124.	-32.	16.	-54.	-0.234E-02	-0.104E+00	0.428E-01	-0.147E+00	-0.141E-01	0.579E-03
20104.	-52.00	140.58	381.61	14.80	66.	-151.	-36.	13.	-58.	-0.238E-02	-0.120E+00	0.390E-01	-0.137E+00	-0.173E-01	0.252E-03
20112.	-52.50	140.55	381.22	14.80	65.	-181.	-40.	10.	-62.	-0.209E-02	-0.112E+00	0.398E-01	-0.114E+00	-0.209E-01	-0.268E-05
20119.	-53.00	140.51	380.83	14.80	31.	-217.	-44.	11.	-63.	-0.155E-02	-0.115E+00	0.156E-01	-0.987E-01	-0.252E-01	-0.203E-03
20127.	-53.50	140.48	380.44	14.81	-42.	-258.	-45.	12.	-60.	-0.856E-03	-0.157E+00	-0.412E-01	-0.908E-01	-0.302E-01	-0.255E-03
20135.	-54.00	140.45	380.07	14.81	-169.	-302.	-44.	14.	-54.	-0.244E-03	-0.260E+00	-0.152E+00	-0.770E-01	-0.355E-01	-0.162E-06
20142.	-54.50	140.43	379.59	14.81	-237.	-342.	-43.	13.	-47.	0.213E-03	-0.312E+00	-0.219E+00	-0.463E-01	-0.405E-01	0.545E-01
20150.	-55.00	140.40	379.20	14.81	-272.	-375.	-42.	10.	-42.	0.338E-03	-0.307E+00	-0.246E+00	-0.175E-01	-0.447E-01	0.835E-03
20158.	-55.50	140.37	378.73	14.81	-249.	-402.	-41.	3.	-40.	-0.545E-04	-0.214E+00	-0.203E+00	0.486E-01	-0.481E-01	0.301E-03
20166.	-56.00	140.33	378.33	14.81	-232.	-421.	-39.	-5.	-43.	-0.822E-03	-0.129E+00	-0.166E+00	0.806E-01	-0.508E-01	-0.645E-03
20173.	-56.50	140.30	377.87	14.81	-199.	-431.	-36.	-13.	-50.	-0.173E-02	-0.568E-01	-0.126E+00	0.967E-01	-0.523E-01	-0.129E-02
20181.	-57.00	140.27	377.45	14.81	-178.	-431.	-34.	-18.	-57.	-0.252E-02	-0.188E-01	-0.104E+00	0.103E+00	-0.526E-01	-0.110E-02
20189.	-57.50	140.24	377.02	14.81	-172.	-425.	-34.	-20.	-64.	-0.208E-02	-0.920E-02	-0.101E+00	0.917E-01	-0.522E-01	-0.326E-03
20196.	-58.00	140.21	376.52	14.81	-155.	-423.	-36.	-19.	-66.	-0.262E-02	-0.120E-01	-0.917E-01	0.374E-01	-0.521E-01	0.243E-03
20204.	-58.50	140.18	376.10	14.81	-114.	-428.	-39.	-17.	-63.	-0.185E-02	-0.352E-01	-0.640E-01	-0.559E-01	-0.531E-01	0.343E-03
20212.	-59.00	140.16	375.68	14.81	-44.	-437.	-43.	-17.	-56.	-0.897E-03	-0.806E-01	-0.177E-01	-0.154E+00	-0.545E-01	0.245E-03
20219.	-59.50	140.13	375.19	14.81	20.	-433.	-48.	-16.	-49.	0.108E-02	-0.135E+00	0.258E-01	-0.154E+00	-0.542E-01	0.175E-03
20227.	-60.00	140.10	374.71	14.81	74.	-411.			-42.	0.114E-02	-0.135E+00	0.701E-01	-0.197E+00	-0.517E-01	

Table 4.1   Summary of observations and calculations along track of second orbit. All values have been interpolated to half degree increments of latitude.

62
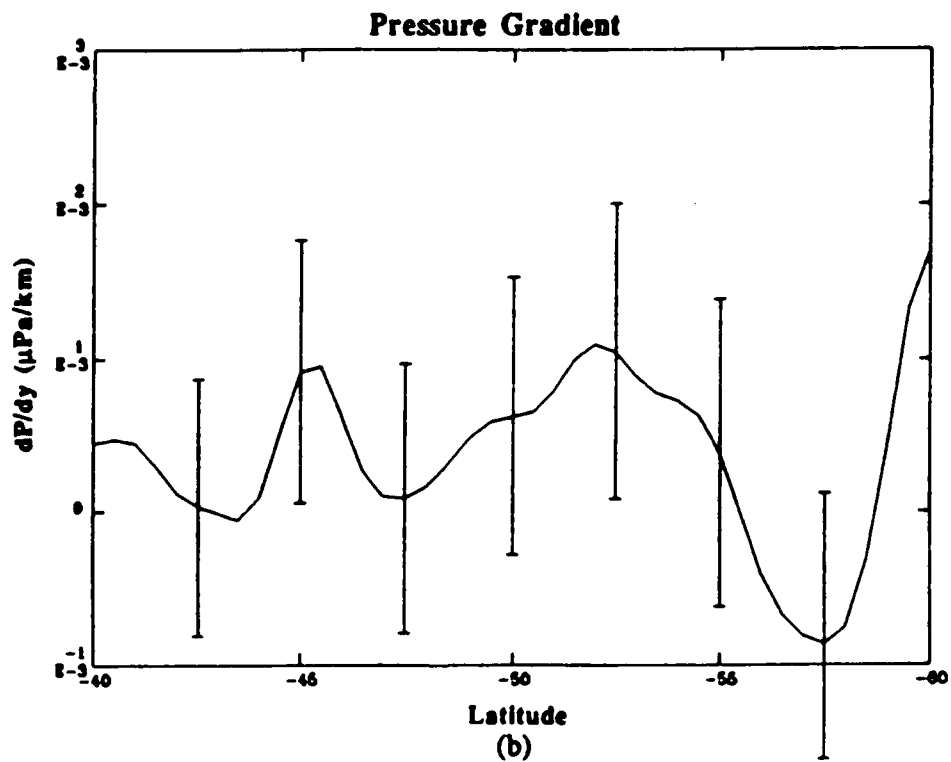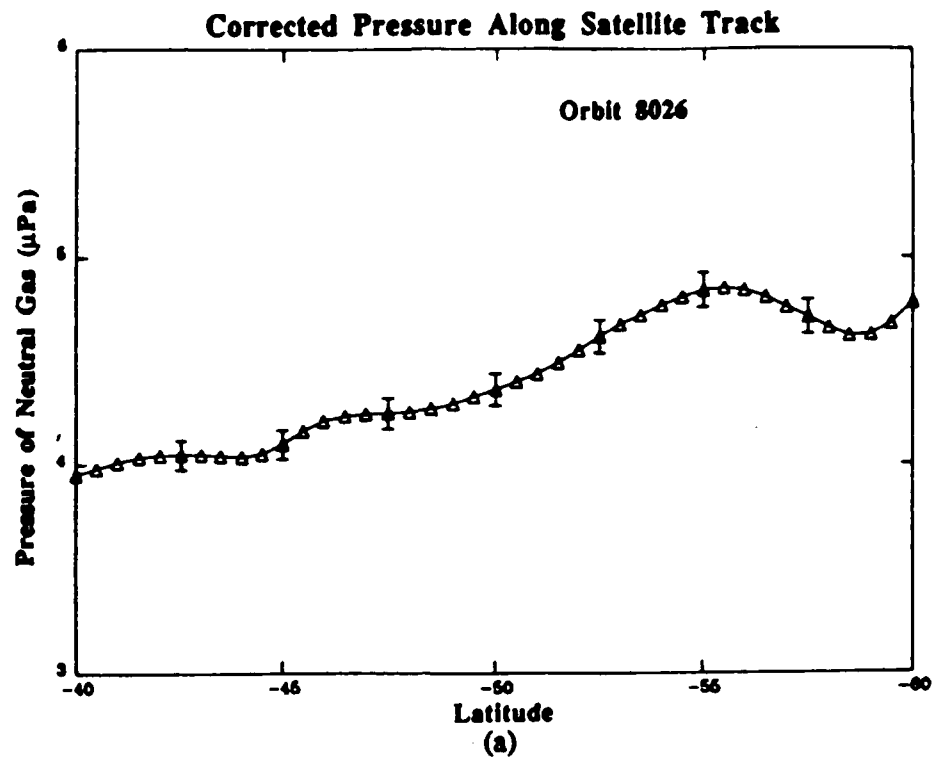
Figure 4.24 Smoothed pressure values along second orbit (a). Plotting symbols denote observation points. Meridional pressure gradient (b) showing error bars resulting from assumed uncertainties in pressure calculation.

63
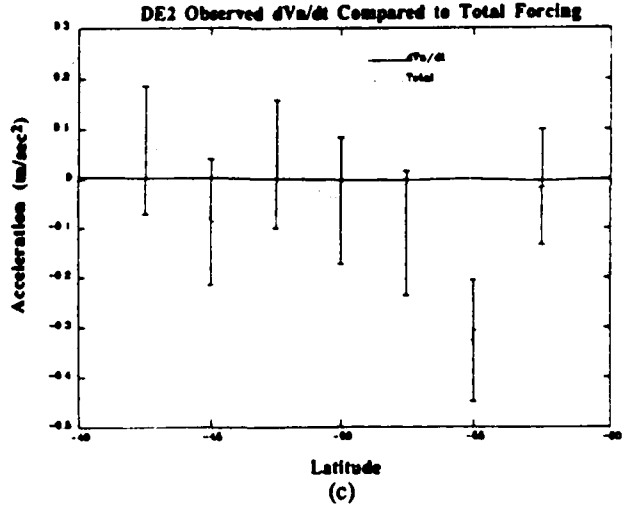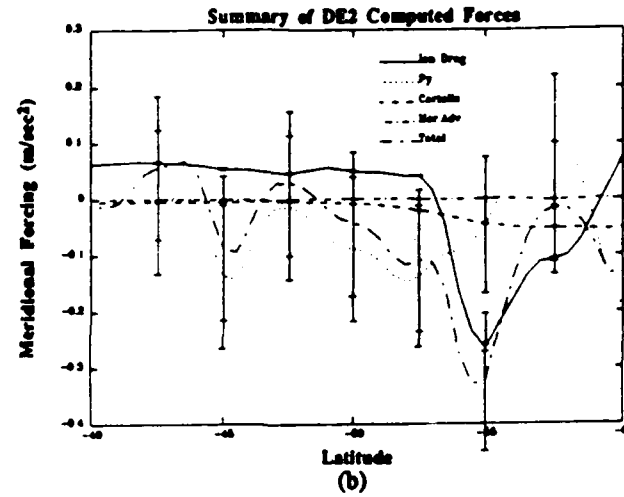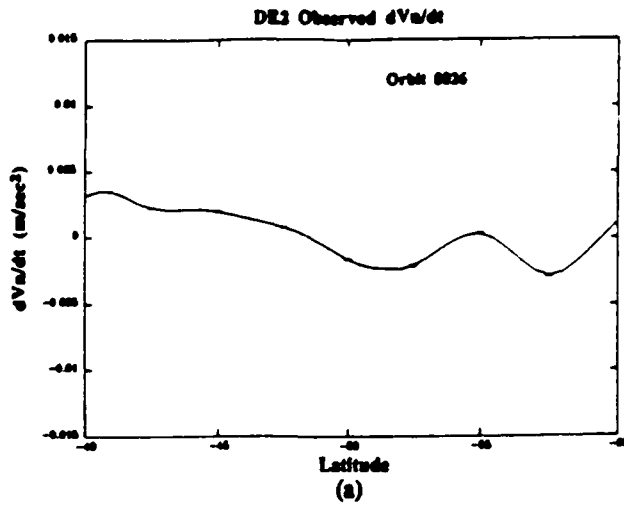
Figure 4.25 Summary of results showing comparison of observed acceleration (a) to the indivdual forces (b) and directly to the total (c). Observed acce'eration is far less than instantaneous forces.

Chapter 5 Conclusions and Remarks

The objective of this thesis was to demostrate the validity of the momentum equation based on both theoretical and experimental data. To this end I obtained a large amount of theoretical data from a single run of the NCAR general circulation model. I also had at my disposal volumes of microfiched archive data from several previous runs of an early version of the TGCM as well as vast amounts of DE-2 satellite data.

My approach was very simple in principle. The momentum equation in its eularian form states that the instantaneous acceleration of the wind at some location is exactly equal to the sum of all the forces that are acting upon the airstream at that same location for that same instant in time. In Appendix A I carefully derived the physical relationship between moving and stationary observers and how their measurements would differ in a very precise way. I also showed here that it was possible to relate the slope in the trace of a moving observer's chart recorder to the changing values of the measured quantity within the medium and account for the observer's relative motion. This set the stage for the experiment to include measurements and computations based on satellite data.

In section 4.1 I applied the predictions of the momentum equation to a fixed location in space and used microfiche data from an early TGCM run. In spite of the relatively crude manner in which data was transferred from the microfiche the data analysis software, the results for this phase were extremely encouraging. The local acceleration did indeed appear to be equal to the sum of the terms in the momentum equation. This enthusiasm was short-lived as I proceeded to the next phase of the experiment.

When I tried to apply the same analysis to the working data base, the results were not nearly as good. I found that the forces began to exceed the measured acceleration as soon as the ion drag force became appreciable. When the ion drag force was small in comparison to the sum of the other forces, the momentum equation did appear to verfy. The apparent discrepancy could not be readily attributed to impulsive ion forcing because the drag force was a smoothly varying function of time whose functional form could be approximated. It was decided to proceed with the next phase of the experiment and choose locations where ion drag was expected to be small.

Section 4.2 involved satellite simulations in an analogous case to that of the stationary observer. This time, how ver, I intentionally didn't include the forces that could

not be measured from a real satellite. As expected, the results were not as favorable as those of the fixed observer cases. What was not expected was the degree towhich the momentum equation failed to verify. Even when the missing terms were restored to the force calculation, the results were marginal at best.

Finally, in section 4.3 I applied the analysis to real satellite data. The data appeared to be very reasonable and free from noise. It was unusually complete and smooth curves of raw data were obtained. However, when all the calculations were made, the forcing curves beared no resemblence whatever to the acceleration curve. When plotted on the same scale, the total forcing curve showed significant time-dependent structure, yet no variations in the accerlation curve could be discerned.

In spite of the apparent lack of success in this experiment I demonstrated that most of the significant forces in the momentum equation could be calculated. The problem when it comes to trying to use the total force to compute local accelerations is that the total force us usually small in comparison with either the ion drag and pressure gradient or both. The difference between the two is often very small and it is the difference that provides the driving force for the atmosphere. Any uncertainties in the computation of either of the forces could very well be sufficient to make local acceleration predictions virtually meaningless.

I still believe it is possible to use satellite data in a moving observer analogy; perhaps the momentum equation is not the one to use to experiment with this. The energy equation is also involved in the TGCM and may be a candidate for a similar study.

Appendix A The Physical Meaning of the Total Derivative

In making applications of the momentum equation one has to be absolutely certain of the physical meaning of all the terms involved. While it may seem a rather simple concept, the total time derivative of the wind components has historically been a source of considerable confusion or misconception. It is the purpose of this section to remove any confusion regarding the total derivative (as it is used throughout this thesis) and in the process attach a physical meaning to this term.

It is safe to say that establishing a clearly defined coordinate system is fundamental to any discussion regarding the measurement of some physical quantity at different times and at a variety of locations. For the present discussion consider the rectangular coordinate system depicted in figure A.1. The axes are labelled with arbitrary values, but it may be instructive to consider the units to be statute miles and the grid pattern to represent an area on the earth's surface. The X and Y directions naturally correspond to the east and north directions respectively. With the coordinate system thus defined, we can calculate all positions and velocities with respect to its origin.

Within this coordinate system we will be recording measurements of some scalar quantity Q that is a characteristic of the air. Q can be any continuous measurable quantity, but for our purposes it is useful to think of it as the temperature of the air. The labelled dashed lines in figure 1a represent an analysis of the spatial distribution of Q at some point in time we have designated as t=0. From figure A.1 it is apparent that the value of Q is a function of X and Y with a local maximum at location (10,15). Figures A.1(a) and A.1(b) depict the same coordinate system and Q distribution at the two future times indicated. It is clear from the figures that the Q distribution is moving eastward as time progresses; the physical interpretation being that the airmass is moving (with respect to our coordinate system) and carries its values of Q with it. By comparing the analyses in each figure it also becomes apparent that the distribution itself is changing as it moves eastward. The physical interpretation of this is that the airmass itself is changing in the quantity Q as time goes on. If Q is the air temperature, then we can think of the airmass as a whole as gradually warming up with time. Clearly then, the value of Q depends not only on the location of the observer within the coordinate system but on the time of the observation as well.

Within the coordinate system are three observers; one observer I.   ed at
location (30,20), while the other two are moving within the coordinate system. A mobile
observer (M) is located at (90,30) at t=0 and is travelling in a westerly direction. The third
observer (B) is riding in a free flying balloon and as such is constrained to follow the wind;
he is thus stationary in relation to the airmass. Figure A.2 is a repeat of figure A.1(b) with
the paths of observers M and B superimposed on the coordinate system. Note that at time
t=3 the locations of all three observers coincide.

It is further presumed that all three observers are taking continuous measurements
of Q and are recording them on a chart-type recorder as shown in figure A.3. Note that at
time t=3 the values of Q recorded by each observer is the same (same location and time).
Note further that while the instantaneous value of Q is the same for all three observers at
this point , the *slopes* of the three curves are quite different at this point. In other words,
the rate of change of Q is different for all three observers even though the value itself is the
same. The next step is to try to calculate the value of the rate of change for all three
observers.

Let $Q(x,y,t)$ represent the spatial and temporal dependency of the quantity Q. Next
consider a differential change in Q and expand it according to the rules of differential
calculus as follows:

$$dQ = \frac{\partial Q}{\partial x}dx + \frac{\partial Q}{\partial y}dy + \frac{\partial Q}{\partial t}dt \qquad \text{(A-1)}$$

Dividing both sides of this expression by dt yields:

$$\frac{dQ}{dt} = \frac{\partial Q}{\partial x}\frac{dx}{dt} + \frac{\partial Q}{\partial y}\frac{dy}{dt} + \frac{\partial Q}{\partial t} \qquad \text{(A-2)}$$

The left hand side of this expression is just the time rate of change of quantity Q as
determined by an observer. Physically, this is the slope of the trace on the observer's chart
recorder. We recognize the quantities dx/dt and dy/dt on the right hand side as the X and Y
components of observer's velocity (as defined in our coordinate system). We can consider
the case of the mobile observer (M) and rewrite (A-2) as shown.

$$\frac{dQ_m}{dt} = \frac{\partial Q}{\partial x}V_{mx} + \frac{\partial Q}{\partial y}V_{my} + \frac{\partial Q}{\partial t} \qquad \text{(A-3)}$$

The subscript denotes values that are unique to the particular observer. The last term on the
right hand side is the time rate of change of Q the observer would record if his velocity

were zero; in other words, the slope on his trace if he were fixed at some location. In our example, this term is the slope of observer L's chart trace. We can rewrite (A-3) in vector form by recognizing the first two terms on the right hand side as the scalar product of a velocity and spatial gradient of Q.

$$\frac{dQ_m}{dt} = V_m \cdot \nabla Q + \frac{\partial Q}{\partial t} \qquad (A-4)$$

This is the familiar definition of the total time derivative of Q. As we have already noted, its physical interpretation can be thought of as the slope of the trace of continuous Q observations taken by an observer who is moving with velocity V within a spatially dependent field of Q. This value is a combination of the changes in Q occurring at that particular location and the changes he observers as a result of his motion. Clearly, the total derivative is unique to the observer, but the <u>local time derivative</u> (the second term in the right hand side of (A-4)) is observer independent. We can come up with a quantitative expression for the local derivative if we repeat (A-3) from the viewpoint of the balloon-borne observer (**B**).

$$\frac{dQ_b}{dt} = \frac{\partial Q}{\partial x} V_{bx} + \frac{\partial Q}{\partial y} V_{by} + \frac{\partial Q}{\partial t}$$

$$(A-5)$$

Since **B** is forced to follow the airmass, we can substitute the components of the wind velocity into (A-5) and come up with the following equivalent expression:

$$\frac{dQ_b}{dt} = \frac{\partial Q}{\partial x} u + \frac{\partial Q}{\partial y} v + \frac{\partial Q}{\partial t} \qquad (A-6)$$

Solving equation (A-6) for $\partial Q/dt$ yields the following expression.

$$\frac{\partial Q}{\partial t} = \frac{dQ_b}{dt} - \left(\frac{\partial Q}{\partial x} u + \frac{\partial Q}{\partial y} v \right) \qquad (A-7)$$

Or equivalently in vector form:

$$\frac{dQ}{dt} = \frac{dQ_b}{dt} - V_r \cdot \nabla Q \qquad \{ V_r \equiv V_w - V_m \} \qquad (A-8)$$

The first term on the right hand side (in addition to being the slope of **B**'s chart trace in figure A.3) represents the rate at which the quantity Q is changing *within the airmass itself.*

6 9

If Q is the temperature, then this term reflects the rate at which the airmass (or more correctly, this part of the airmass) is warming due to physical heating processes.

The vector quantity on the right (including the minus sign) is commonly called the *advection* of Q. It is the quantity responsible for observed changes in, say, temperature that result purely from the motion of the airmass past this fixed location. We can substitute expression (A-7) for the local derivative into (A-3) to obtain after rearranging:

$$\frac{dQ_m}{dt} = \frac{dQ_b}{dt} - \left[(u - V_{mx})\frac{\partial Q}{\partial t} + (v - V_{my})\frac{\partial Q}{\partial y} \right] \qquad \text{(A-9)}$$

Once again changing to the equivalent vector form:

$$\frac{\partial Q}{\partial t} = \frac{dQ_b}{dt} - V_r \cdot \nabla Q \qquad \{ V_r \equiv V_w - V_m \} \qquad \text{(A-10)}$$

The vector V_r is defined as the difference between the observer's velocity and that of the wind and is commonly referred to as the *relative wind*. Note if the observer's velocity is zero, then his total derivative assumes the role of a local derivative and we have the situation in equation (A-8). If on the other hand the wind velocity is zero, then B's total derivative becomes a local derivative and we are back to equations (A-3) and (A-4).

Equation (A-10) gives us a form of the total derivative that is very useful in interpreting the momentum equation. If instead of Q we use, say, the zonal wind component, then the first term on the right hand side in (A-10) becomes du_b/dt and is the total derivative of u following the motion of the air. In other words, it is acceleration of the air at the point of the observation that is the result of the sum of all real forces acting at that point. These forces are the individual terms in the momentum equation that do not include advection. The advection term is the second term on the right hand side and is a function of both the local wind velocity and the observer's velocity within the coordinate system. Equation (A-10) stated in words unequivocally assigns the physical meaning to the total derivative as follows:

> The instantaneous rate of change of a component of the wind for an observer moving within a well defined reference frame is equal to the total acceleration of that component of the airflow at that location minus the scalar (dot) product of the wind velocity relative to the observer and the locally observed gradient in the component being measured.
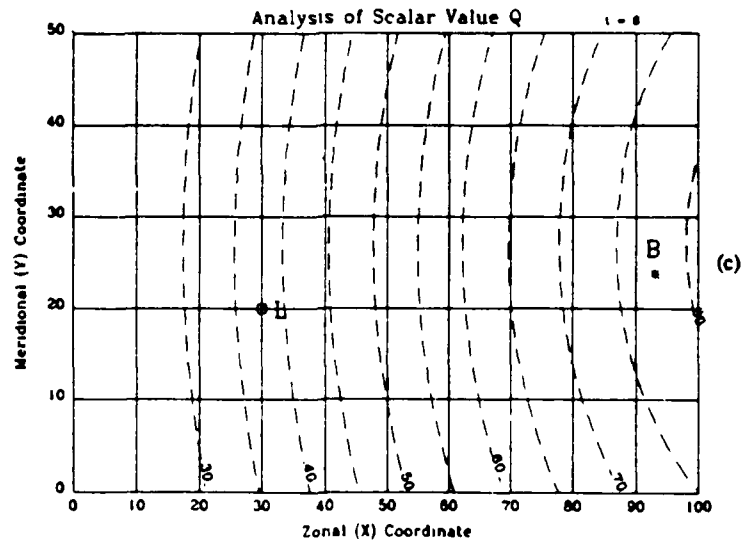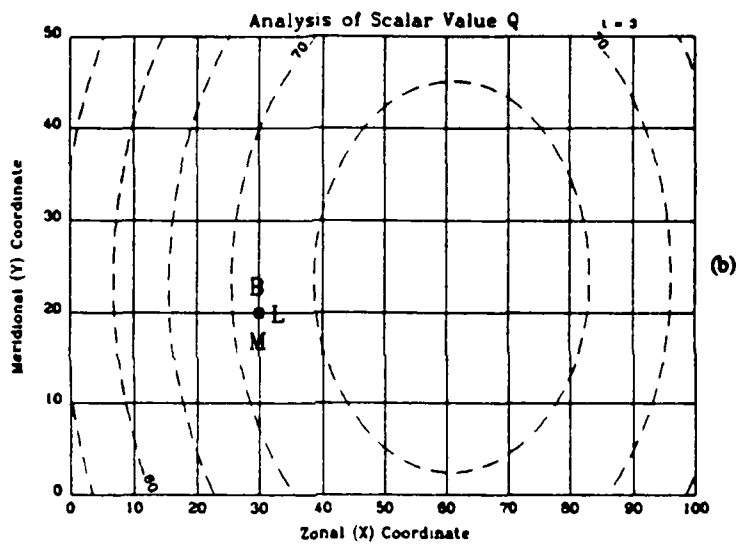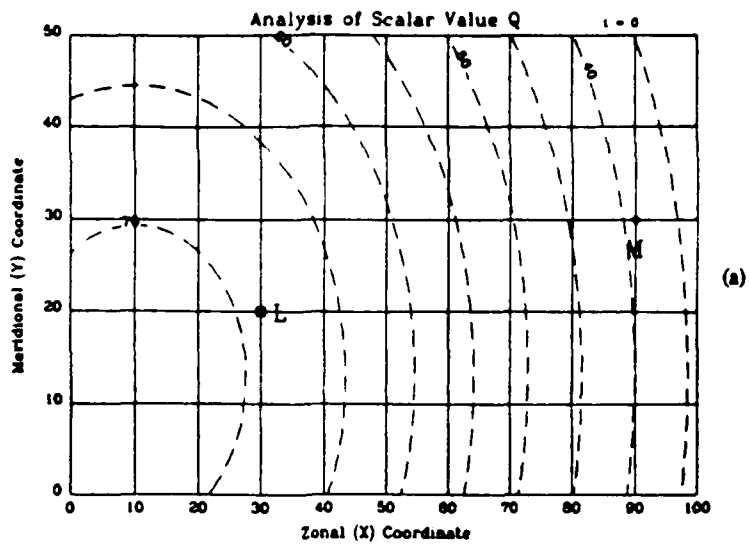
Figure A.1 Hypothetical distribution of a scalar value Q at three different times. Diagrams show locations of stationary and two moving observers (L, M, and B).
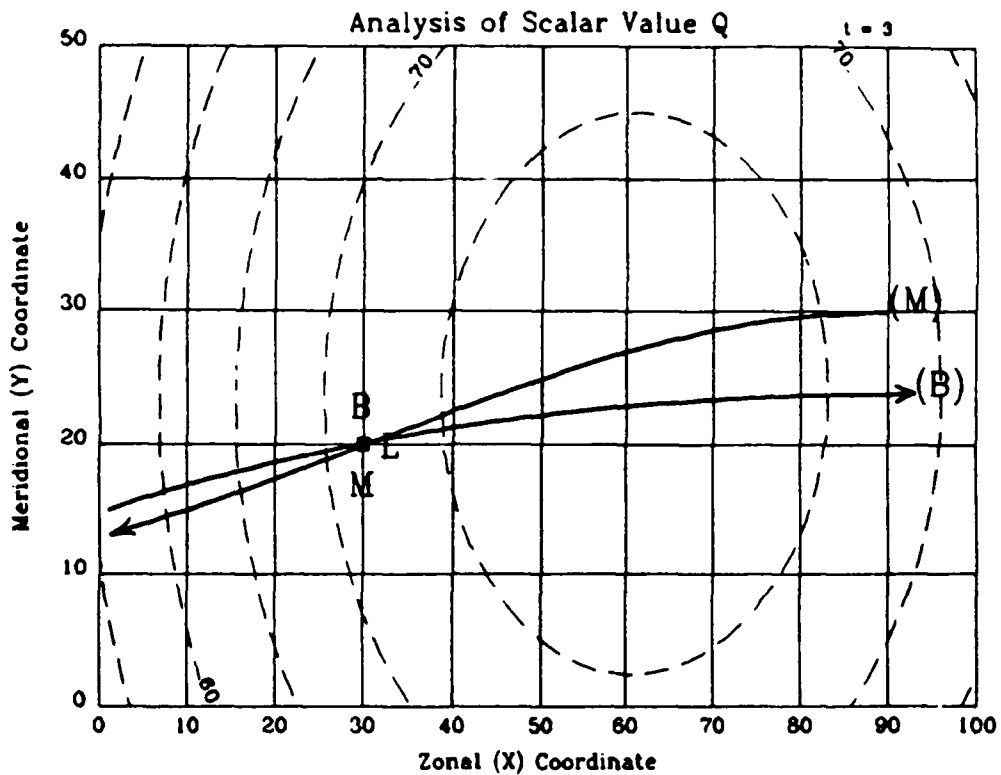
Figure A.2 Situation at time t = 3 showing all observers at same location. Trajectories of moving observers have been superimposed on the diagram.
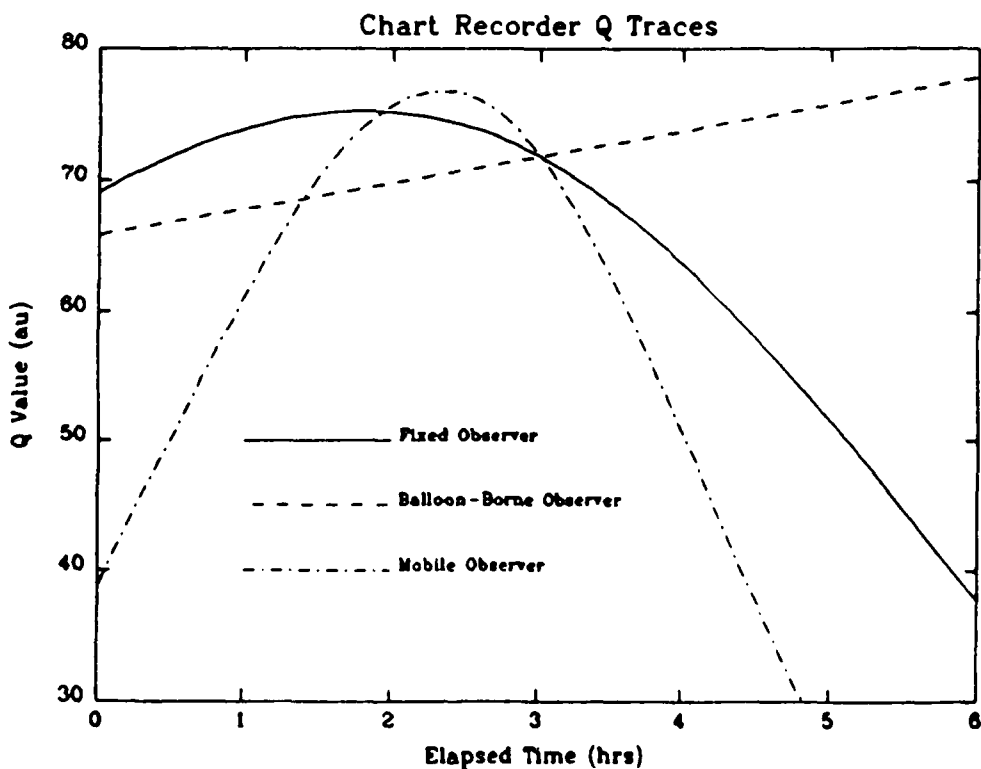
Figure A.3 Superimposed chart traces from the three observers. The curves cross at t=3 because all observers were at the same location. Different slopes at this point result from differing observer velocities.

72

Appendix B   Calculation of Errors in the Momentum Equation

Throughout this project little emphasis was placed on estimating the actual absolute error in the raw satellite data. Conversely, much was done to examine the *effects* of errors in the subsequent calculations involving these measured quantities. Specifically, we consider the errors in the forcing term calculations arising from an estimated relative error in the raw data. The treatment of error propagation in calculations is treated in *Greenberg* [1975] and is applied in this section.

In a function involving several variables the error in the calculation arising from uncertainties in the variables can be estimated as follows:

$$F(x_1, x_2, x_3 \dots) \quad \Rightarrow \quad \delta F = \frac{\partial F}{\partial x_1} \delta x_1 + \frac{\partial F}{\partial x_2} \delta x_2 + \frac{\partial F}{\partial x_3} \delta x_3 \qquad (B\text{-}1)$$

in the above expression, δF represents the absolute error in the calculation of F resulting from the absolute uncertainties in its constituent quantities (δx_1, δx_2, δx_3, ...). This expression actually estimates the maximum *possible* error, since a straight forward sum of the individual uncertainties is used to make the estimate. It is unlikely, however, that in any one calculation all of the individual quantities would simultaneously be in error by the maximum range in their uncertainties. For this reason we choose to use the *probable* error in these calculations. For an absolute error consisting of a sum of several individual errors, then the probable error is computed as follows:

$$(\delta F)_{prob} = \sqrt{\Sigma (\delta x_n)^2} \qquad (B\text{-}2)$$

where δx_n are the absolute errors in the measurement of quantity x_n.

If a calculation involves th· product of several variables, each containing its own uncertainty, then the *relative error* in the value of the function is the sum of the individual relative errors. The probable error involving such a product is computed as shown.

$$\left(\frac{\delta F}{F} \right) = \sqrt{\Sigma \left(\frac{\delta(x_n)}{x_n} \right)^2} \qquad (B\text{-}3)$$

The applications of these fundamental principles to the present problem are addressed in the paragraphs that follow.

All momentum calculations in this project are based on data that is available from the DE satellite data base. Among this includes the ion temperature (T_i), neutral temperature (T_n), atomic oxygen density (nO), nitrogen density (nN_2), electron density (ne), neutral meridional wind (V_n), ion meridional wind (V_i), and neutral zonal wind (U_n). No attempt is made here to estimate the absolute errors likely to be encountered in these data; the purpose of this section is to observe how momentum calculations are affected by errors. Thus, each of the quantities listed is assumed to have an inherent relative error of .01 (1%).

B.1 Observed Acceleration (AV_n)

A finite-centered differencing technique is used to estimate the value of the time derivative (or acceleration) of the observed neutral wind. For each latitude an observation is made once each orbit. Thus if we record wind observations (V_0, V_1, V_2, ...) every Δt seconds, the acceleration is given by:

$$AV_n \equiv \frac{dV_n}{dt} \cong \frac{1}{2\Delta t}(V_2 - V_0) \qquad \text{(B-4)}$$

Applying (B-1) to this function yields the following expressions for the absolute possible and probable errors:

$$\delta AV_n = \left| \frac{\partial AV_n}{\partial V_2} \delta V_2 \right| + \left| \frac{\partial AV_n}{\partial V_0} \delta V_0 \right| \qquad \text{(B-5a)}$$

$$(\delta AV_n)_{poss} = \frac{1}{2\Delta t}(\delta V_2) + \frac{1}{2\Delta t}(\delta V_0) \qquad \text{(B-5b)}$$

$$(\delta AV_n)_{prob} = \frac{1}{2\Delta t}\left[(\delta V_2)^2 + (\delta V_0)^2 \right]^{1/2} \qquad \text{(B-5c)}$$

where δV_0 and δV_2 are the absolute errors taken from the value of V_2 and V_0 and the assumed relative error of 1 percent.

B.2 Coriolis Force (VCor)

The Coriolis force is easily calculated from the measured wind as follows:

$$VCor = -fU_n \qquad \text{(B-6)}$$

74

Where f is the Coriolis parameter and depends only on latitude. From this formula and the above discussion the absolute error in the Coriolis term becomes:

$$\delta VCor = f\delta U_n \qquad \text{where} \quad \delta U_n = \left(\frac{\delta U_n}{U_n}\right) U_n \qquad \text{(B-7)}$$

B.3 Meridional Advection (MAv)

The meridional term of the momentum advection can be approximated from the available DE data:

$$MA_v \equiv - V_v \frac{\partial V_n}{\partial y} = - V_n GradV_n \qquad \text{(B-8)}$$

The relative error in the above calculation of advection is then:

$$\left(\frac{\delta MA_v}{MA_v}\right)_{prob} = \left[\left(\frac{\delta V_n}{V_n}\right)^2 + \left(\frac{\delta GradV_n}{GradV_n}\right)^2\right]^{1/2} \qquad \text{(B-9)}$$

The first term in brackets is the relative error in V_n and is either estimated or determined experimentally. V_n is measured along the satellite track and is virtually continuous, so finite-centered differencing can be used to compute $GradV_n$ as follows:

$$GradV_n \cong \frac{1}{2\Delta y}(V_2 - V_0) \qquad \text{(B-10)}$$

The probable error in this calculation is then:

$$\delta GradV_n = \frac{1}{2\Delta y}\left[(\delta V_2)^2 + (\delta V_0)2\right]^{1/2} \qquad \text{(B-11)}$$

Because the Δy term appears in the denominator, one must use care in computing gradients along the track of the satellite. If the smallest Δy is used, the resulting uncertainty in the calculation might be larger than the expected magnitude of the gradient. If Δy is too large, then the approximation to the spatial derivative becomes less accurate.

B.4 Pressure Gradient Force (Py)

The pressure gradient force is calculated with the following formula:

$$P_y = -\frac{1}{\rho}\left(\frac{\partial P}{\partial y}\right)_z = -(\rho)^{-1}(\text{GradP})_z \qquad (B\text{-}12)$$

The subsequent expression for the error is found by applying (B-1). The result is:

$$(\delta P_y)_{poss} = \left(\frac{\partial P_y}{\partial \rho}\right)\delta\rho + \left(\frac{\partial P_y}{\partial \text{Grad P}}\right)\delta \text{Grad P} \qquad (B\text{-}13a)$$

$$(\delta P_y)_{poss} = \frac{\text{GradP}}{\rho^2}\delta\rho + \frac{1}{\rho}\delta\text{GradP} \qquad (B\text{-}13b)$$

$$(\delta P_y)_{prob} = \left[\left(\text{GradP}\frac{\delta\rho}{\rho^2}\right)^2 + \left(\frac{\delta\text{GradP}}{\rho}\right)^2\right]^{1/2} \qquad (B\text{-}13c)$$

The neutral mass density (ρ) and uncertainty are readily calculated from the raw data:

$$\rho = \left(6.01 \times 10^{20}\right)^{-1}(\text{mO}\cdot\text{nO} + \text{mN}_2\cdot\text{nN}_2) \quad (\text{kg/m}^3) \qquad (B\text{-}14a)$$

$$\delta\rho = \left(6.01 \times 10^{20}\right)^{-1}\left[(\text{mO}\cdot\delta\text{nO})^2 + (\text{mN}_2\cdot\delta\text{nN}_2)^2\right]^{1/2} \qquad (B\text{-}14b)$$

where mO and mN$_2$ are atomic and molecular weights of oxygen and nitrogen. The pressure gradient is calculated in the same manner as the meridional velocity gradient above. The resulting erro· in this calculation is:

$$\delta\text{GradP} = \frac{1}{2\Delta y}\left[(\delta P_2)^2 + (\delta P_0)^2\right]^{1/2} \qquad (B\text{-}15)$$

As before, the value of Δy should be carefully chosen to ensure the magnitude of the uncertainty does not exceed that of the gradient. The pressure and its uncertainty are calculated from the ideal gas law:

$$P = n_n k_B T_n \qquad (B\text{-}16a)$$

$$\frac{\delta P}{P} = \frac{\delta n_n}{n_n} + \frac{\delta T_n}{T_n} \qquad (B\text{-}16b)$$

The second term on the right hand side of (B-16b) is the estimated relative error of the neutral temperature. The first term on the right hand side is the relative error in the neutral density:

$$n_n = nO + nN_2 \quad \Rightarrow \quad \delta n_n = \left[(\delta nO)^2 + (\delta nN_2)^2 \right]^{1/2} \quad \text{(B-17)}$$

Finally, the absolute probable error in the pressure calculation is given by:

$$\delta P_y = P \left[\left(\frac{\delta n_n}{n_n} \right)^2 + \left(\frac{\delta T_n}{T_n} \right)^2 \right]^{1/2} \quad \text{(B-18)}$$

B.5 Ion Drag (ID)

The ion drag force and resulting possible relative error can be calculated with the following expressions:

$$ID = v_{in} V_{in} n_r \quad \Rightarrow \quad \frac{\delta ID}{ID} = \frac{\delta v_{in}}{v_{in}} + \frac{\delta V_{in}}{V_{in}} + \frac{\delta n_r}{n_r} \quad \text{(B-19)}$$

where: $\quad v_{in}$ = ion-neutral momentum transfer collision frequency

$$V_{in} = (V_i - V_n)$$

$$n_r = n_e / n_n$$

The last two terms on the right hand side are easily calculated as follows:

$$\frac{\delta n_r}{n_r} = \left[\left(\frac{\delta n_e}{n_e} \right)^2 + \left(\frac{\delta n_n}{n_n} \right)^2 \right]^{1/2} \quad \text{(B-20a)}$$

$$\delta V_{in} = \left[(\delta V_i)^2 + (\delta V_r)^2 \right]^{1/2} \quad \text{(B-20b)}$$

The error in the collision frequency requires many more computations, the total ion-neutral collision frequency being the sum of the collision ion-oxygen and ion-nitrogen collision frequencies:

$$v_{in} = v_{iO} + v_{iN2} \quad \Rightarrow \quad \delta n_n = \left[(\delta v_{iO})^2 + (\delta v_{iN2})^2 \right]^{1/2} \quad \text{(B-21)}$$

The formulas for calculating the ion-nitrogen collision frequency and uncertainty are fairly simple:

77

$$v_{iN2} = C_3 n_{N2} \quad \Rightarrow \quad \delta v_{iN2} = C_3 \delta n_{N2} \tag{B-22}$$

The resonant ion-oxygen collision frequency requires a more complex formula:

$$v_{iO} = C_1 \, nO \, T_r^{1/2} B^2 \tag{B-23}$$

where: $\quad T_r = .5 \, (T_i + T_n)$

$\qquad\qquad\qquad B = 1 - C_2 \, Log_{10}(T_r)$

Equation (B-1) must be rigorously applied to this expression as follows:

$$\delta v_{iO} = \frac{\partial v_{iO}}{\partial nO} \delta nO + \frac{\partial v_{iO}}{\partial T_r} \delta T_r \tag{B-24a}$$

where $\quad \delta T_r = .5 \left[(\delta T_i)^2 + (\delta T_n)^2 \right]^{1/2} \tag{B-24b}$

Performing the indicated partial differentiations eventually leads to the following expression for the absolute error in the ion-oxygen collision frequency:

$$\delta v_{iO} = \left\{ \left[C_1 T_r^{1/2} B^2 \, \delta nO \right]^2 + \left[\frac{C_1 \, nO}{2 T_r^{1/2}} \left(B^2 - 1.74 C_2 \right) \delta T_r \right]^2 \right\}^{1/2} \tag{B-25}$$

B.6 Total Force (TOTy)

The absolute probable error for the total force is found by summing the individual errors in the usual way:

$$\delta TOT_y = \left[(\delta ID)^2 + (\delta P_y)^2 + (\delta MA_y)^2 + (\delta VCor)^2 \right]^{1/2} \tag{B-26}$$

Appendix C   Simulated Satellite Data

This section contains listings of the simulated data and calculated quantities in the satellite simulations described in sections 4.2.1 and 4.2.2. Because of their size the data tables were included in an appendix rather than in the main body. Table C.1 contains the data from the constant longitude portion of the experiment. Table C.2 contains the data and computations from the constant latitude case.

SIMULATED DATA RECORDED BY A NORTHBOUND SATELLITE MOVING ALONG ZERO DEGREE MERIDIAN

Time(s)	Lat	Un	Vn	Py	VCor	Vdrag	Geom	KAv	dVn/dt
0	37.5	-5.21	35.9	8.62E-03	4.62E-04	-7.68E-03	-3.08E-06	-1.73E-02	-1.73E-02
8	38.0	-6.05	35.7	8.61E-03	5.46E-04	-7.66E-03	-4.25E-06	-1.73E-02	-1.74E-02
16	38.5	-6.86	35.6	8.61E-03	6.27E-04	-7.63E-03	-5.55E-06	-1.76E-02	-1.77E-02
24	39.0	-7.61	35.4	8.61E-03	7.05E-04	-7.59E-03	-6.96E-06	-1.81E-02	-1.81E-02
32	39.5	-8.33	35.3	8.60E-03	7.79E-04	-7.56E-03	-8.49E-06	-1.87E-02	-1.88E-02
40	40.0	-9.01	35.1	8.59E-03	8.50E-04	-7.51E-03	-1.01E-05	-1.96E-02	-1.97E-02
48	40.5	-9.65	35.0	8.58E-03	9.18E-04	-7.46E-03	-1.18E-05	-2.06E-02	-2.07E-02
56	41.0	-10.2	34.8	8.57E-03	9.84E-04	-7.40E-03	-1.35E-05	-2.19E-02	-2.20E-02
64	41.5	-10.8	34.6	8.55E-03	1.04E-03	-7.34E-03	-1.54E-05	-2.35E-02	-2.36E-02
72	42.0	-11.3	34.4	8.53E-03	1.10E-03	-7.27E-03	-1.72E-05	-2.53E-02	-2.54E-02
80	42.5	-11.8	34.2	8.51E-03	1.16E-03	-7.20E-03	-1.92E-05	-2.72E-02	-2.74E-02
88	43.0	-12.3	34.0	8.48E-03	1.22E-03	-7.12E-03	-2.11E-05	-2.90E-02	-2.91E-02
96	43.5	-12.8	33.7	8.45E-03	1.28E-03	-7.04E-03	-2.30E-05	-3.02E-02	-3.03E-02
104	44.0	-13.2	33.5	8.42E-03	1.33E-03	-6.95E-03	-2.49E-05	-3.06E-02	-3.08E-02
112	44.5	-13.5	33.2	8.39E-03	1.38E-03	-6.85E-03	-2.68E-05	-3.05E-02	-3.06E-02
120	45.0	-13.8	33.0	8.36E-03	1.42E-03	-6.75E-03	-2.85E-05	-2.96E-02	-2.97E-02
128	45.5	-14.1	32.8	8.32E-03	1.46E-03	-6.63E-03	-3.01E-05	-2.80E-02	-2.82E-02
136	46.0	-14.3	32.5	8.29E-03	1.49E-03	-6.51E-03	-3.14E-05	-2.58E-02	-2.59E-02
144	46.5	-14.4	32.4	8.26E-03	1.52E-03	-6.38E-03	-3.26E-05	-2.28E-02	-2.29E-02
152	47.0	-14.5	32.2	8.23E-03	1.54E-03	-6.24E-03	-3.34E-05	-1.91E-02	-1.92E-02
160	47.5	-14.4	32.0	8.21E-03	1.55E-03	-6.09E-03	-3.39E-05	-1.46E-02	-1.47E-02
168	48.0	-14.3	31.9	8.19E-03	1.55E-03	-5.93E-03	-3.39E-05	-9.66E-03	-9.70E-03
176	48.5	-14.1	31.9	8.18E-03	1.54E-03	-5.76E-03	-3.35E-05	-4.25E-03	-4.27E-03
184	49.0	-13.8	31.9	8.17E-03	1.51E-03	-5.59E-03	-3.25E-05	1.53E-03	1.54E-03
192	49.5	-13.3	31.9	8.17E-03	1.48E-03	-5.41E-03	-3.11E-05	7.77E-03	7.80E-03
200	50.0	-12.8	32.0	8.18E-03	1.43E-03	-5.24E-03	-2.90E-05	1.45E-02	1.45E-02
208	50.5	-12.1	32.1	8.19E-03	1.36E-03	-5.08E-03	-2.64E-05	2.18E-02	2.19E-02
216	51.0	-11.2	32.4	8.21E-03	1.27E-03	-4.93E-03	-2.32E-05	2.98E-02	2.99E-02
224	51.5	-10.2	32.6	8.24E-03	1.17E-03	-4.79E-03	-1.96E-05	3.85E-02	3.86E-02
232	52.0	-9.06	33.0	8.28E-03	1.04E-03	-4.67E-03	-1.56E-05	4.80E-02	4.82E-02
240	52.5	-7.67	33.4	8.32E-03	8.85E-04	-4.58E-03	-1.13E-05	5.85E-02	5.88E-02
248	53.0	-6.06	33.9	8.38E-03	7.02E-04	-4.52E-03	-7.23E-06	7.10E-02	7.13E-02
256	53.5	-4.25	34.5	8.45E-03	4.94E-04	-4.49E-03	-3.63E-06	8.62E-02	8.66E-02
264	54.0	-2.26	35.3	8.52E-03	2.62E-04	-4.48E-03	-1.05E-06	0.10	0.10
272	54.5	-0.112	36.2	8.60E-03	7.48E-06	-4.49E-03	-2.63E-09	0.12	0.12
280	55.0	2.19	37.3	8.69E-03	-2.68E-04	-4.53E-03	-1.02E-06	0.15	0.15
288	55.5	4.64	38.7	8.78E-03	-5.63E-04	-4.59E-03	-4.65E-06	0.17	0.18
296	56.0	7.22	40.2	8.87E-03	-8.77E-04	-4.66E-03	-1.14E-05	0.21	0.21
304	56.5	9.92	42.1	8.96E-03	-1.20E-03	-4.76E-03	-2.20E-05	0.24	0.25
312	57.0	12.7	44.2	9.05E-03	-1.55E-03	-4.87E-03	-3.69E-05	0.29	0.29
320	57.5	15.6	46.8	9.14E-03	-1.92E-03	-5.00E-03	-5.69E-05	0.33	0.33
328	58.0	18.6	49.7	9.22E-03	-2.30E-03	-5.14E-03	-8.24E-05	0.38	0.38
336	58.5	21.7	52.9	9.29E-03	-2.69E-03	-5.28E-03	-1.14E-04	0.42	0.42
344	59.0	24.8	56.4	9.33E-03	-3.09E-03	-5.41E-03	-1.51E-04	0.45	0.45
352	59.5	27.8	60.2	9.34E-03	-3.50E-03	-5.50E-03	-1.95E-04	0.47	0.48
360	60.0	30.9	64.2	9.30E-03	-3.90E-03	-5.54E-03	-2.45E-04	0.49	0.50
368	60.5	33.9	68.2	9.20E-03	-4.29E-03	-5.51E-03	-3.01E-04	0.51	0.51
376	61.0	36.7	72.4	9.03E-03	-4.67E-03	-5.40E-03	-3.61E-04	0.52	0.52
384	61.5	39.5	76.7	8.78E-03	-5.04E-03	-5.18E-03	-4.26E-04	0.52	0.53
392	62.0	42.0	81.0	8.43E-03	-5.39E-03	-4.83E-03	-4.92E-04	0.52	0.53
400	62.5	44.3	85.2	7.97E-03	-5.71E-03	-4.33E-03	-5.60E-04	0.51	0.52
408	63.0	46.4	89.3	7.39E-03	-6.00E-03	-3.67E-03	-6.26E-04	0.51	0.51
416	63.5	48.1	93.5	6.67E-03	-6.26E-03	-2.88E-03	-6.89E-04	0.50	0.51
424	64.0	49.5	97.6	5.82E-03	-6.47E-03	-1.98E-03	-7.47E-04	0.51	0.51
432	64.5	50.6	101.	4.83E-03	-6.64E-03	-1.03E-03	-7.97E-04	0.51	0.52
440	65.0	51.2	106.	3.68E-03	-6.75E-03	-5.65E-05	-8.36E-04	0.53	0.54
448	65.5	51.4	110.	2.38E-03	-6.81E-03	9.14E-04	-8.61E-04	0.54	0.55
456	66.0	51.1	115.	9.07E-04	-6.79E-03	1.84E-03	-8.70E-04	0.57	0.58
464	66.5	50.2	119.	-7.49E-04	-6.70E-03	2.69E-03	-8.60E-04	0.60	0.61
472	67.0	48.7	124.	-2.60E-03	-6.52E-03	3.42E-03	-8.28E-04	0.63	0.64
480	67.5	46.4	130.	-4.67E-03	-6.24E-03	4.00E-03	-7.73E-04	0.67	0.68
488	68.0	43.4	135.	-6.96E-03	-5.86E-03	4.43E-03	-6.93E-04	0.69	0.71
496	68.5	39.6	141.	-9.45E-03	-5.37E-03	4.91E-03	-5.91E-04	0.70	0.71
504	69.0	34.8	147.	-1.21E-02	-4.74E-03	5.64E-03	-4.69E-04	0.67	0.68
512	69.5	29.1	152.	-1.48E-02	-3.98E-03	6.88E-03	-3.36E-04	0.61	0.63
520	70.0	22.3	157.	-1.77E-02	-3.06E-03	8.84E-03	-2.03E-04	0.53	0.54

Table C.1 Constant Longitude Simulation Data

- continued from previous page -

Time(s)	Lat	Un	Vn	Py	VCor	Vdrag	Geom	NAv	dVn/dt
528	70.5	14.3	161.	-2.06E-02	-1.98E-03	1.17E-02	-8.65E-05	0.42	0.43
536	71.0	5.13	164.	-2.36E-02	-7.19E-04	1.59E-02	-1.13E-05	0.27	0.28
544	71.5	-5.51	165.	-2.66E-02	7.49E-04	2.16E-02	-1.34E-05	0.10	0.10
552	72.0	-17.6	165.	-2.96E-02	2.44E-03	2.90E-02	-1.42E-04	-0.10	-0.10
560	72.5	-31.5	164.	-3.25E-02	4.37E-03	3.85E-02	-4.68E-04	-0.34	-0.35
568	73.0	-47.2	160.	-3.53E-02	6.57E-03	5.03E-02	-1.08E-03	-0.59	-0.60
576	73.5	-64.4	154.	-3.79E-02	9.00E-03	6.37E-02	-2.07E-03	-0.81	-0.83
584	74.0	-83.0	146.	-4.04E-02	1.16E-02	7.82E-02	-3.56E-03	-1.0	-1.0
592	74.5	-102.	137.	-4.24E-02	1.44E-02	9.31E-02	-5.62E-03	-1.1	-1.2
600	75.0	-123.	127.	-4.41E-02	1.73E-02	0.10	-8.37E-03	-1.3	-1.3
608	75.5	-144.	116.	-4.53E-02	2.03E-02	0.12	-1.18E-02	-1.4	-1.4
616	76.0	-165.	103.	-4.58E-02	2.33E-02	0.13	-1.62E-02	-1.5	-1.5
624	76.5	-186.	90.8	-4.57E-02	2.64E-02	0.14	-2.15E-02	-1.6	-1.6
632	77.0	-208.	77.0	-4.47E-02	2.95E-02	0.14	-2.78E-02	-1.7	-1.7
640	77.5	-229.	62.7	-4.29E-02	3.25E-02	0.15	-3.51E-02	-1.7	-1.8
648	78.0	-249.	48.1	-4.00E-02	3.55E-02	0.15	-4.35E-02	-1.8	-1.8
656	78.5	-269.	33.1	-3.62E-02	3.84E-02	0.14	-5.30E-02	-1.8	-1.8
664	79.0	-288.	17.9	-3.18E-02	4.11E-02	0.13	-6.35E-02	-1.9	-1.9
672	79.5	-306.	2.54	-2.69E-02	4.38E-02	0.12	-7.51E-02	-1.9	-1.9
680	80.0	-323.	-13.0	-2.16E-02	4.62E-02	0.11	-8.77E-02	-1.9	-1.9
688	80.5	-338.	-28.7	-1.62E-02	4.84E-02	0.10	-0.10	-1.9	-1.9
696	81.0	-351.	-44.5	-1.08E-02	5.04E-02	9.06E-02	-0.11	-1.9	-1.9
704	81.5	-362.	-60.3	-5.52E-03	5.21E-02	7.83E-02	-0.13	-1.9	-1.9
712	82.0	-371.	-76.1	-5.81E-04	5.35E-02	6.72E-02	-0.14	-1.9	-1.9
720	82.5	-378.	-91.9	3.86E-03	5.45E-02	5.79E-02	-0.16	-1.9	-1.9
728	83.0	-382.	-107.	7.67E-03	5.51E-02	5.10E-02	-0.17	-1.9	-1.9
736	83.5	-383.	-123.	1.08E-02	5.53E-02	4.65E-02	-0.19	-1.9	-1.9
744	84.0	-382.	-138.	1.35E-02	5.52E-02	4.40E-02	-0.20	-1.9	-1.9
752	84.5	-378.	-154.	1.57E-02	5.47E-02	4.33E-02	-0.22	-1.9	-1.9
760	85.0	-373.	-169.	1.75E-02	5.39E-02	4.40E-02	-0.23	-1.9	-1.9
768	85.5	-365.	-185.	1.90E-02	5.28E-02	4.62E-02	-0.25	-1.9	-1.9
776	86.0	-354.	-200.	2.01E-02	5.14E-02	4.94E-02	-0.26	-1.9	-1.9
784	86.5	-342.	-216.	2.10E-02	4.96E-02	5.35E-02	-0.28	-1.9	-1.9
792	87.0	-328.	-231.	2.16E-02	4.76E-02	5.84E-02	-0.30	-2.0	-1.9
800	87.5	-311.	-247.	2.21E-02	4.53E-02	6.38E-02	-0.33	-2.0	-1.9

Table C.1 Constant Longitude Simulation Data - cont.

DATA FROM SECOND SIMULATED SATELLITE RUN (THREE ORBITS)

Time	Lat	Lon	Un	Vn	Vdrag	VCor	Py	Geom	MAv
4.4479	30.00	23.28	0.00	0.00	0.000E+00	0.000E+00	0.000E+00	0.000E+00	0.000E+00
4.4501	30.53	23.25	0.00	0.00	0.000E+00	0.000E+00	0.000E+00	0.000E+00	0.000E+00
4.4524	31.07	23.21	0.00	0.00	0.000E+00	0.000E+00	0.000E+00	0.000E+00	0.000E+00
4.4546	31.60	23.18	0.00	0.00	0.000E+00	0.000E+00	0.000E+00	0.000E+00	0.000E+00
4.4568	32.13	23.15	0.00	0.00	0.000E+00	0.000E+00	0.000E+00	0.000E+00	0.000E+00
4.4590	32.67	23 11	0.00	0.00	0.000E+00	0.000E+00	0.000E+00	0.000E+00	0.000E+00
4.4612	33.20	23.08	0.00	0.00	0.000E+00	0.000E+00	0.000E+00	0.000E+00	0.000E+00
4.4635	33.73	23.05	0.00	0.00	0.000E+00	0.000E+00	0.000E+00	0.000E+00	0.000E+00
4.4657	34.27	23.01	0.00	0.00	0.000E+00	0.000E+00	0.000E+00	0.000E+00	0.000E+00
4.4679	34.80	22.98	0.00	0.00	0.000E+00	0.000E+00	0.000E+00	0.000E+00	0.000E+00
4.4701	35.33	22.95	0.00	0.00	0.000E+00	0.000E+00	0.000E+00	0.000E+00	0.000E+00
4.4724	35.87	22.91	0.00	0.00	0.000E+00	0.000E+00	0.000E+00	0.000E+00	0.000E+00
4.4746	36.40	22.88	0.00	0.00	0.000E+00	0.000E+00	0.000E+00	0.000E+00	0.000E+00
4.4768	36.93	22.85	0.00	0.00	0.000E+00	0.000E+00	0.000E+00	0.000E+00	0.000E+00
4.4790	37.47	22.81	0.00	0.00	0.000E+00	0.000E+00	0.000E+00	0.000E+00	0.000E+00
4.4812	38.00	22.78	-3.43	35.34	-0.830E-02	0.261E-03	0.930E-02	-0.136E-05	0.000E+00
4.4835	38.53	22.75	-4.00	35.32	-0.832E-02	0.316E-03	0.933E-02	-0.189E-05	0.142E-04
4.4857	39.07	22.71	-4.58	35.29	-0.833E-02	0.374E-03	0.936E-02	-0.252E-05	0.226E-04
4.4879	39.60	22.68	-5.17	35.24	-0.835E-02	0.433E-03	0.938E-02	-0.328E-05	0.316E-04
4.4901	40.13	22.65	-5.77	35.18	-0.835E-02	0.495E-03	0.940E-02	-0.416E-05	0.412E-04
4.4924	40.67	22.61	-6.39	35.09	-0.836E-02	0.560E-03	0.941E-02	-0.520E-05	0.516E-04
4.4946	41.20	22.58	-7.03	34.99	-0.835E-02	0.628E-03	0.942E-02	-0.641E-05	0.627E-04
4.4968	41.73	22.55	-7.69	34.87	-0.835E-02	0.700E-03	0.942E-02	-0.781E-05	0.748E-04
4.4990	42.27	22.51	-8.37	34.72	-0.835E-02	0.775E-03	0.941E-02	-0.943E-05	0.879E-04
4.5012	42.80	22.48	-9.07	34.55	-0.834E-02	0.854E-03	0.939E-02	-0.113E-04	0.101E-03
4.5035	43.33	22.45	-9.80	34.36	-0.833E-02	0.937E-03	0.936E-02	-0.134E-04	0.112E-03
4.5057	43.87	22.41	-10.55	34.14	-0.831E-02	0.102E-02	0.932E-02	-0.159E-04	0.120E-03
4.5079	44.40	22.38	-11.31	33.91	-0.829E-02	0.111E-02	0.928E-02	-0.186E-04	0.126E-03
4.5101	44.93	22.35	-12.06	33.68	-0.826E-02	0.120E-02	0.924E-02	-0.215E-04	0.129E-03
4.5124	45.47	22.31	-12.82	33.43	-0.823E-02	0.129F-02	0.920E-02	-0.247E-04	0.129E-03
4.5146	46.00	22.28	-13.55	33.19	-0.819E-02	0.138E-02	0.916E-02	-0.282E-04	0.127E-03
4.5168	46.53	22.25	-14.27	32.95	-0.813E-02	0.147E-02	0.913E-02	-0.319E-04	0.123E-03
4.5190	47.07	22.21	-14.96	32.72	-0.807E-02	0.155E-02	0.910E-02	-0.357E-04	0.117E-03
4.5212	47.60	22.18	-15.61	32.50	-0.799E-02	0.164E-02	0.909E-02	-0.396E-04	0.109E-03
4.5235	48.13	22.15	-16.23	32.30	-0.790E-02	0.172E-02	0.908E-02	-0.436E-04	0.102E-03
4.5257	48.67	22.11	-16.79	32.11	-0.779E-02	0.179E-02	0.908E-02	-0.475E-04	0.957E-04
4.5279	49.20	22.08	-17.32	31.92	-0.766E-02	0.187E-02	0.907E-02	-0.515E-04	0.916E-04
4.5301	49.73	22.05	-17.81	31.75	-0.752E-02	0.194E-02	0.906E-02	-0.555E-04	0.891E-04
4.5324	50.27	22.01	-18.26	31.57	-0.737E-02	0.200E-02	0.904E-02	-0.594E-04	0.883E-04
4.5346	50.80	21.98	-18.66	31.40	-0.720E-02	0.207E-02	0.900E-02	-0.633E-04	0.890E-04
4.5368	51.33	21.95	-19.02	31.21	-0.701E-02	0.212E-02	0.893E-02	-0.670E-04	0.914E-04
4.5390	51.87	21.91	-19.33	31.03	-0.681E-02	0.218E-02	0.884E-02	-0.706E-04	0.953E-04
4.5412	52.40	21.88	-19.60	30.83	-0.658E-02	0.223E-02	0.870E-02	-0.740E-04	0.100E-03
4.5435	52.93	21.85	-19.82	30.62	-0.634E-02	0.228E-02	0.853E-02	-0.771E-04	0.998E-04
4.5457	53.47	21.81	-19.96	30.42	-0.609E-02	0.232E-02	0.832E-02	-0.797E-04	0.874E-04
4.5479	54.00	21.78	-19.99	30.26	-0.583E-02	0.234E-02	0.810E-02	-0.816E-04	0.607E-04
4.5501	54.53	21.75	-19.89	30.17	-0.558E-02	0.235E-02	0.788E-02	-0.824E-04	0.197E-04
4.5524	55.07	21.71	-19.63	30.18	-0.534E-02	0.234E-02	0.767E-02	-0.818E-04	-0.363E-04
4.5546	55.60	21.68	-19.16	30.32	-0.513E-02	0.231E-02	0.750E-02	-0.795E-04	-0.109E-03
4.5568	56.13	21.65	-18.46	30.63	-0.495E-02	0.224E-02	0.738E-02	-0.753E-04	-0.200E-03
4.5590	56.67	21.61	-17.48	31.14	-0.482E-02	0.213E-02	0.732E-02	-0.689E-04	-0.313E-03
4.5612	57.20	21.58	-16.18	31.89	-0.475E-02	0.199E-02	0.735E-02	-0.603E-04	-0.453E-03
4.5635	57.73	21.55	-14.52	32.92	-0.474E-02	0.179E-02	0.748E-02	-0.495E-04	-0.618E-03
4.5657	58.27	21.51	-12.48	34.25	-0.480E-02	0.155E-02	0.772E-02	-0.374E-04	-0.797E-03
4.5679	58.80	21.48	-10.09	35.85	-0.493E-02	0.125E-02	0.806E-02	-0.249E-04	-0.986E-03
4.5701	59.33	21.45	-7.36	37.70	-0.512E-02	0.914R-03	0.849E-02	-0.136E-04	-0.119E-02
4.5724	59.87	21.41	-4.32	39.80	-0.537E-02	0.534E-03	0.901E-02	-0.477E-05	-0.133E-02
5.9479	30.00	0.78	0.00	0.00	0.000E+00	0.000E+00	0.000E+00	0.000E+00	0.000E+00
5.9501	30.53	0.75	0.00	0.00	0.000E+00	0.000E+00	0.000E+00	0.000E+00	0.000E+00
5.9524	31.07	0.71	0.00	0.00	0.000E+00	0.000E+00	0.000E+00	0.000E+00	0.000E+00
5.9546	31.60	0.68	0.00	0.00	0.000E+00	0.000E+00	0.000E+00	0.000E+00	0.000E+00
5.9568	32.13	0.65	0.00	0.00	0.000E+00	0.000E+00	0.000E+00	0.000E+00	0.000E+00

Table C.2 Constant Latitude Simulation Data

82

Time	Lat	Lon	Un	Vn	Vdrag	VCor	Py	Geom	MAv
5.9590	32.67	0.61	0.00	0.00	0.000E+00	0.000E+00	0.000E+00	0.000E+00	0.000E+00
5.9612	33.20	0.58	0.00	0.00	0.000E+00	0.000E+00	0.000E+00	0.000E+00	0.000E+00
5.9635	33.73	0.55	0.00	0.00	0.000E+00	0.000E+00	0.000E+00	0.000E+00	0.000E+00
5.9657	34.27	0.51	0.00	0.00	0.000E+00	0.000E+00	0.000E+00	0.000E+00	0.000E+00
5.9679	34.80	0.48	0.00	0.00	0.000E+00	0.000E+00	0.000E+00	0.000E+00	0.000E+00
5.9701	35.33	0.45	0.00	0.00	0.000E+00	0.000E+00	0.000E+00	0.000E+00	0.000E+00
5.9724	35.87	0.41	0.00	0.00	0.000E+00	0.000E+00	0.000E+00	0.000E+00	0.000E+00
5.9746	36.40	0.38	0.00	0.00	0.000E+00	0.000E+00	0.000E+00	0.000E+00	0.000E+00
5.9768	36.93	0.35	0.00	0.00	0.000E+00	0.000E+00	0.000E+00	0.000E+00	0.000E+00
5.9790	37.47	0.31	0.00	0.00	0.000E+00	0.000E+00	0.000E+00	0.000E+00	0.000E+00
5.9812	38.00	0.28	-5.65	35.81	-0.774E-02	0.505E-03	0.865E-02	-0.370E-05	0.000E+00
5.9835	38.53	0.25	-6.54	35.64	-0.766E-02	0.595E-03	0.863E-02	-0.505E-05	0.961E-04
5.9857	39.07	0.21	-7.37	35.47	-0.758E-02	0.680E-03	0.861E-02	-0.653E-05	0.977E-04
5.9879	39.60	0.18	-8.15	35.29	-0.750E-02	0.761E-03	0.860E-02	-0.815E-05	0.100E-03
5.9901	40.13	0.15	-8.89	35.11	-0.742E-02	0.839E-03	0.858E-02	-0.987E-05	0.103E-03
5.9924	40.67	0.11	-9.57	34.92	-0.733E-02	0.913E-03	0.856E-02	-0.117E-04	0.107E-03
5.9946	41.20	0.08	-10.22	34.73	-0.724E-02	0.983E-03	0.854E-02	-0.136E-04	0.112E-03
5.9968	41.73	0.05	-10.82	34.52	-0.715E-02	0.105E-02	0.853E-02	-0.155E-04	0.117E-03
5.9990	42.27	0.01	-11.37	34.30	-0.706E-02	0.111E-02	0.851E-02	-0.174E-04	0.124E-03
6.0012	42.80	-0.02	-11.88	34.07	-0.697E-02	0.117E-02	0.849E-02	-0.194E-04	0.130E-03
6.0035	43.33	-0.05	-12.34	33.82	-0.688E-02	0.123E-02	0.847E-02	-0.213E-04	0.134E-03
6.0057	43.87	-0.09	-12.76	33.57	-0.678E-02	0.128E-02	0.846E-02	-0.232E-04	0.136E-03
6.0079	44.40	-0.12	-13.12	33.31	-0.668E-02	0.133E-02	0.844E-02	-0.250E-04	0.135E-03
6.0101	44.93	-0.15	-13.43	33.06	-0.658E-02	0.138E-02	0.842E-02	-0.267E-04	0.132E-03
6.0124	45.47	-0.19	-13.68	32.81	-0.647E-02	0.141E-02	0.840E-02	-0.282E-04	0.126E-03
6.0146	46.00	-0.22	-13.86	32.58	-0.634E-02	0.145E-02	0.839E-02	-0.295E-04	0.118E-03
6.0168	46.53	-0.25	-13.97	32.36	-0.621E-02	0.147E-02	0.837E-02	-0.305E-04	0.107E-03
6.0190	47.07	-0.29	-14.01	32.16	-0.606E-02	0.149E-02	0.835E-02	-0.313E-04	0.939E-04
6.0212	47.60	-0.32	-13.96	31.99	-0.590E-02	0.150E-02	0.833E-02	-0.316E-04	0.780E-04
6.0235	48.13	-0.35	-13.81	31.85	-0.571E-02	0.149E-02	0.831E-02	-0.316E-04	0.586E-04
6.0257	48.67	-0.39	-13.56	31.76	-0.552E-02	0.148E-02	0.830E-02	-0.310E-04	0.351E-04
6.0279	49.20	-0.42	-13.18	31.72	-0.532E-02	0.145E-02	0.829E-02	-0.298E-04	0.717E-05
6.0301	49.73	-0.45	-12.64	31.73	-0.513E-02	0.141E-02	0.829E-02	-0.280E-04	-0.257E-04
6.0324	50.27	-0.49	-11.94	31.82	-0.494E-02	0.134E-02	0.831E-02	-0.254E-04	-0.641E-04
6.0346	50.80	-0.52	-11.05	31.98	-0.477E-02	0.125E-02	0.834E-02	-0.222E-04	-0.109E-03
6.0368	51.33	-0.55	-9.93	32.24	-0.462E-02	0.113E-02	0.839E-02	-0.183E-04	-0.161E-03
6.0390	51.87	-0.59	-8.57	32.61	-0.450E-02	0.983E-03	0.847E-02	-0.139E-04	-0.221E-03
6.0412	52.40	-0.62	-6.93	33.10	-0.441E-02	0.800E-03	0.858E-02	-0.925E-05	-0.292E-03
6.0435	52.93	-0.65	-4.99	33.72	-0.436E-02	0.578E-03	0.872E-02	-0.408E-05	-0.373E-03
6.0457	53.47	-0.69	-2.76	34.49	-0.435E-02	0.319E-03	0.889E-02	-0.153E-05	-0.467E-03
6.0479	54.00	-0.72	-0.29	35.42	-0.438E-02	0.286E-04	0.908E-02	-0.171E-07	-0.576E-03
6.0501	54.53	-0.75	2.39	36.53	-0.442E-02	-0.290E-03	0.928E-02	-0.119E-05	-0.704E-03
6.0524	55.07	-0.79	5.25	37.84	-0.448E-02	-0.632E-03	0.950E-02	-0.585E-05	-0.854E-03
6.0546	55.60	-0.82	8.25	39.36	-0.455E-02	-0.996E-03	0.971E-02	-0.147E-04	-0.103E-02
6.0568	56.13	-0.85	11.36	41.13	-0.462E-02	-0.138E-02	0.991E-02	-0.285E-04	-0.124E-02
6.0590	56.67	-0.89	14.56	43.16	-0.469E-02	-0.177E-02	0.101E-01	-0.478E-04	-0.150E-02
6.0612	57.20	-0.92	17.81	45.48	-0.475E-02	-0.218E-02	0.103E-01	-0.730E-04	-0.180E-02
6.0635	57.73	-0.95	21.10	48.13	-0.478E-02	-0.259E-02	0.104E-01	-0.105E-03	-0.216E-02
6.0657	58.27	-0.99	24.40	51.11	-0.480E-02	-0.302E-02	0.105E-01	-0.143E-03	-0.255E-02
6.0679	58.80	-1.02	27.72	54.40	-0.480E-02	-0.345E-02	0.106E-01	-0.188E-03	-0.299E-02
6.0701	59.33	-1.05	31.09	58.00	-0.478E-02	-0.389E-02	0.107E-01	-0.242E-03	-0.345E-02
6.0724	59.87	-1.09	34.49	61.88	-0.475E-02	-0.433E-02	0.108E-01	-0.304E-03	-0.383E-02
7.4479	30.00	-21.72	0.00	0.00	0.000E+00	0.000E+00	0.000E+00	0.000E+00	0.000E+00
7.4501	30.53	-21.75	0.00	0.00	0.000E+00	0.000E+00	0.000E+00	0.000E+00	0.000E+00
7.4524	31.07	-21.79	0.00	0.00	0.000E+00	0.000E+00	0.000E+00	0.000E+00	0.000E+00
7.4546	31.60	-21.82	0.00	0.00	0.000E+00	0.000E+00	0.000E+00	0.000E+00	0.000E+00
7.4568	32.13	-21.85	0.00	0.00	0.000E+00	0.000E+00	0.000E+00	0.000E+00	0.000E+00
7.4590	32.67	-21.89	0.00	0.00	0.000E+00	0.000E+00	0.000E+00	0.000E+00	0.000E+00
7.4612	33.20	-21.92	0.00	0.00	0.000E+00	0.000E+00	0.000E+00	0.000E+00	0.000E+00
7.4635	33.73	-21.95	0.00	0.00	0.000E+00	0.000E+00	0.000E+00	0.000E+00	0.000E+00
7.4657	34.27	-21.99	0.00	0.00	0.000E+00	0.000E+00	0.000E+00	0.000E+00	0.000E+00
7.4679	34.80	-22.02	0.00	0.00	0.000E+00	0.000E+00	0.000E+00	0.000E+00	0.000E+00

Table C.2 Constant Latitude Simulation Data - cont.

Time	Lat	Lon	Un	Vn	Vdrag	VCor	Py	Geom	RAv
7.4701	35.33	-22.05	0.00	0.00	0.000E+00	0.000E+00	0.000E+00	0.000E+00	0.000E+00
7.4724	35.87	-22.09	0.00	0.00	0.000E+00	0.000E+00	0.000E+00	0.000E+00	0.000E+00
7.4746	36.40	-22.12	0.00	0.00	0.000E+00	0.000E+00	0.000E+00	0.000E+00	0.000E+00
7.4768	36.93	-22.15	0.00	0.00	0.000E+00	0.000E+00	0.000E+00	0.000E+00	0.000E+00
7.4790	37.47	-22.19	0.00	0.00	0.000E+00	0.000E+00	0.000E+00	0.000E+00	0.000E+00
7.4812	38.00	-22.22	-4.45	32.07	-0.746E-02	0.371E-03	0.838E-02	-0.230E-05	0.000E+00
7.4835	38.53	-22.25	-5.15	31.90	-0.736E-02	0.441E-03	0.835E-02	-0.313E-05	0.783E-04
7.4857	39.07	-22.29	-5.76	31.76	-0.727E-02	0.504E-03	0.833E-02	-0.399E-05	0.623E-04
7.4879	39.60	-22.32	-6.29	31.65	-0.717E-02	0.560E-03	0.832E-02	-0.486E-05	0.474E-04
7.4901	40.13	-22.35	-6.77	31.57	-0.708E-02	0.611E-03	0.833E-02	-0.573E-05	0.336E-04
7.4924	40.67	-22.39	-7.19	31.52	-0.699E-02	0.658E-03	0.835E-02	-0.658E-05	0.205E-04
7.4946	41.20	-22.42	-7.56	31.49	-0.690E-02	0.700E-03	0.838E-02	-0.742E-05	0.802E-05
7.4968	41.73	-22.45	-7.89	31.49	-0.681E-02	0.740E-03	0.843E-02	-0.823E-05	-0.405E-05
7.4990	42.27	-22.49	-8.18	31.51	-0.672E-02	0.778E-03	0.848E-02	-0.902E-05	-0.159E-04
7.5012	42.80	-22.52	-8.44	31.55	-0.663E-02	0.815E-03	0.855E-02	-0.979E-05	-0.281E-04
7.5035	43.33	-22.55	-8.67	31.62	-0.653E-02	0.849E-03	0.864E-02	-0.105E-04	-0.416E-04
7.5057	43.87	-22.59	-8.83	31.72	-0.643E-02	0.878E-03	0.874E-02	-0.111E-04	-0.569E-04
7.5079	44.40	-22.62	-8.91	31.85	-0.634E-02	0.900E-03	0.885E-02	-0.115E-04	-0.742E-04
7.5101	44.93	-22.65	-8.89	32.01	-0.625E-02	0.912E-03	0.897E-02	-0.117E-04	-0.940E-04
7.5124	45.47	-22.69	-8.74	32.21	-0.618E-02	0.910E-03	0.911E-02	-0.115E-04	-0.116E-03
7.5146	46.00	-22.72	-8.45	32.46	-0.611E-02	0.892E-03	0.927E-02	-0.110E-04	-0.142E-03
7.5168	46.53	-22.75	-7.97	32.76	-0.607E-02	0.854E-03	0.944E-02	-0.994E-05	-0.171E-03
7.5190	47.07	-22.79	-7.29	33.12	-0.604E-02	0.794E-03	0.963E-02	-0.846E-05	-0.204E-03
7.5212	47.60	-22.82	-6.37	33.54	-0.603E-02	0.707E-03	0.983E-02	-0.659E-05	-0.243E-03
7.5235	48.13	-22.85	-5.19	34.03	-0.605E-02	0.591E-03	0.101E-01	-0.446E-05	-0.293E-03
7.5257	48.67	-22.89	-3.75	34.62	-0.609E-02	0.445E-03	0.103E-01	-0.238E-05	-0.358E-03
7.5279	49.20	-22.92	-2.06	35.33	-0.615E-02	0.269E-03	0.105E-01	-0.732E-06	-0.441E-03
7.5301	49.73	-22.95	-0.12	36.19	-0.624E-02	0.607E-04	0.108E-01	-0.251E-08	-0.545E-03
7.5324	50.27	-22.99	2.08	37.22	-0.636E-02	-0.180E-03	0.111E-01	-0.774E-06	-0.672E-03
7.5346	50.80	-23.02	4.55	38.46	-0.649E-02	-0.454E-03	0.114E-01	-0.376E-05	-0.830E-03
7.5368	51.33	-23.05	7.29	39.93	-0.665E-02	-0.764E-03	0.117E-01	-0.985E-05	-0.102E-02
7.5390	51.87	-23.09	10.31	41.67	-0.683E-02	-0.111E-02	0.120E-01	-0.201E-04	-0.126E-02
7.5412	52.40	-23.12	13.64	43.73	-0.704E-02	-0.150E-02	0.124E-01	-0.358E-04	-0.155E-02
7.5435	52.93	-23.15	17.28	46.12	-0.728E-02	-0.194E-02	0.127E-01	-0.586E-04	-0.188E-02
7.5457	53.47	-23.19	21.19	48.84	-0.752E-02	-0.241E-02	0.131E-01	-0.899E-04	-0.222E-02
7.5479	54.00	-23.22	25.33	51.82	-0.777E-02	-0.291E-02	0.134E-01	-0.131E-03	-0.256E-02
7.5501	54.53	-23.25	29.63	55.05	-0.799E-02	-0.345E-02	0.138E-01	-0.183E-03	-0.291E-02
7.5524	55.07	-23.29	34.05	58.46	-0.818E-02	-0.400E-02	0.142E-01	-0.246E-03	-0.325E-02
7.5546	55.60	-23.32	38.54	62.03	-0.832E-02	-0.456E-02	0.145E-01	-0.322E-03	-0.359E-02
7.5568	56.13	-23.35	43.05	65.73	-0.839E-02	-0.514E-02	0.148E-01	-0.409E-03	-0.391E-02
7.5590	56.67	-23.39	47.54	69.51	-0.837E-02	-0.571E-02	0.151E-01	-0.509E-03	-0.422E-02
7.5612	57.20	-23.42	51.94	73.35	-0.824E-02	-0.629E-02	0.154E-01	-0.621E-03	-0.450E-02
7.5635	57.73	-23.45	56.22	77.22	-0.798E-02	-0.685E-02	0.156E-01	-0.742E-03	-0.476E-02
7.5657	58.27	-23.49	60.36	81.09	-0.759E-02	-0.741E-02	0.158E-01	-0.873E-03	-0.502E-02
7.5679	58.80	-23.52	64.37	84.99	-0.707E-02	-0.795E-02	0.159E-01	-0.101E-02	-0.529E-02
7.5701	59.33	-23.55	68.27	88.91	-0.644E-02	-0.849E-02	0.161E-01	-0.117E-02	-0.559E-02
7.5724	59.87	-23.59	72.08	92.88	-0.570E-02	-0.902E-02	0.161E-01	-0.133E-02	-0.587E-02

Table C.2 Constant Latitude Simulation Data - cont.

Appendix D   DE Satellite Data Summary

Much of the data used to compute the momentum forcing along the satellite tracks was not explicitly referenced in the text. This appendix includes that data that, though certainly important for computational importance, was not included in the discussion. Rather than take up space in the main body, it was more prudent to include the raw data in a separate section. The raw DE2 data for the three orbits is contained in the following tables and figures:

Tables D.1(a thru c):	Raw data as retrieved from the data base
Figure D.1:	Zonal Neutral Wind (U_n)
Figure D.2:	Meridional Neutral Wind (V_n)
Figure D.3:	Meridional Ion Wind (V_i)
Figure D.4:	Ion Temperature (T_i)
Figure D.5:	Neutral Temperature (T_n)
Figure D.6:	Ion Density (n_e)
Figure D.7:	Neutral Density (n_n)

RAW DATA RETRIEVED FROM DE2 SATELLITE DATA BASE: ORBIT 8025   DAY=83015

TIME	UZ	VZ	WZ	UB	VB	LAF	LAT	LONG	LOCST	MAGLAT	LOCRT	STEMP	ITEMP	NTEMP	ELECDENS	PTEMP	O DENSITY	N2 DENSITY	ALT
14448.	64.	-26.	28.	38.	4.	-12.	-39.13	164.17	14.01	-50.60	15.59	2240.	1421.	1252.	5.934E+05	1235.	2.037E+08	2.311E+07	391.08
14456.	72.	-26.	26.	37.	10.	-14.	-39.65	164.14	14.01	-51.10	15.60	2270.	1429.	1258.	5.793E+05	1240.	2.031E+08	2.333E+07	390.78
14464.	66.	-32.	27.	35.	18.	-20.	-40.17	164.11	14.01	-51.61	15.62	2284.	1451.	1261.	5.682E+05	1263.	2.025E+08	2.356E+07	390.40
14472.	63.	-36.	26.	34.	20.	-21.	-40.68	164.08	14.01	-52.11	15.63	2305.	1430.	1259.	5.607E+05	1277.	2.019E+08	2.375E+07	390.10
14480.	66.	-43.	27.	36.	28.	-19.	-41.20	164.05	14.01	-52.62	15.65	2322.	1461.	1257.	5.513E+05	1264.	2.012E+08	2.398E+07	389.70
14488.	69.	-54.	25.	39.	28.	-24.	-41.72	164.01	14.01	-53.12	15.67	2330.	1464.	1263.	5.423E+05	1257.	2.012E+08	2.420E+07	389.40
14496.	70.	-55.	24.	38.	28.	-24.	-42.24	163.98	14.01	-53.63	15.68	2359.	1463.	1263.	5.353E+05	1292.	2.012E+08	2.447E+07	389.14
14504.	71.	-59.	26.	35.	29.	-21.	-42.76	163.95	14.01	-54.13	15.70	2378.	1460.	1272.	5.260E+05	1296.	2.012E+08	2.473E+07	388.68
14512.	75.	-61.	28.	32.	30.	-16.	-43.28	163.92	14.01	-54.63	15.72	2400.	1476.	1275.	5.102E+05	1300.	2.012E+08	2.500E+07	388.58
14520.	76.	-64.	27.	30.	27.	-20.	-43.80	163.88	14.01	-55.14	15.73	2421.	1442.	1277.	5.113E+05	1299.	2.012E+08	2.527E+07	388.18
14528.	78.	-60.	28.	30.	27.	-24.	-44.32	163.85	14.01	-55.64	15.75	2434.	1475.	1282.	5.101E+05	1298.	2.012E+08	2.553E+07	387.88
14536.	81.	-58.	28.	28.	26.	-23.	-44.84	163.82	14.01	-56.14	15.77	2444.	1465.	1288.	5.082E+05	1296.	2.012E+08	2.580E+07	387.68
14544.	82.	-57.	31.	28.	25.	-20.	-45.36	163.79	14.01	-56.64	15.79	2451.	1460.	1282.	5.041E+05	1297.	2.012E+08	2.606E+07	387.10
14552.	85.	-60.	30.	27.	24.	-21.	-45.87	163.76	14.01	-57.14	15.81	2471.	1447.	1269.	4.997E+05	1295.	2.012E+08	2.636E+07	386.70
14560.	87.	-65.	29.	27.	26.	-15.	-46.39	163.73	14.01	-57.64	15.83	2407.	1442.	1245.	4.900E+05	1287.	2.019E+08	2.667E+07	386.40
14568.	90.	-60.	27.	29.	27.	-16.	-46.91	163.69	14.01	-58.14	15.85	2494.	1445.	1292.	4.901E+05	1295.	2.012E+08	2.689E+07	386.00
14576.	67.	-60.	30.	24.	28.	-21.	-47.43	163.66	14.01	-58.64	15.87	2400.	1446.	1292.	4.344E+05	1287.	2.019E+08	2.712E+07	385.60
14584.	69.	-55.	28.	25.	30.	-20.	-47.95	163.63	14.01	-59.14	15.89	2407.	1456.	1292.	4.906E+05	1263.	2.019E+08	2.731E+07	385.30
14592.	90.	-52.	27.	22.	30.	-13.	-48.47	163.60	14.01	-59.63	15.92	2451.	1458.	1281.	5.020E+05	1279.	2.012E+08	2.750E+07	384.90
14600.	88.	-46.	28.	21.	30.	-12.	-48.99	163.56	14.01	-60.13	15.94	2407.	1473.	1277.	5.047E+05	1282.	2.019E+08	2.773E+07	384.50
14608.	63.	-45.	29.	20.	29.	-12.	-49.51	163.53	14.01	-60.63	15.96	2487.	1436.	1276.	5.060E+05	1292.	2.025E+08	2.795E+07	384.18
14616.	91.	-41.	29.	24.	29.	-14.	-50.03	163.50	14.01	-61.12	15.99	2494.	1449.	1266.	5.078E+05	1305.	2.025E+08	2.816E+07	383.70
14624.	86.	-37.	31.	26.	31.	-13.	-50.54	163.47	14.01	-61.62	16.01	2493.	1458.	1262.	5.071E+05	1310.	2.025E+08	2.841E+07	383.30
14632.	96.	-34.	26.	36.	11.	-17.	-51.06	163.44	14.01	-62.11	16.04	2421.	1458.	1274.	5.080E+05	1312.	2.025E+08	2.846E+07	382.90
14640.	110.	-30.	28.	36.	36.	-17.	-51.58	163.40	14.01	-62.60	16.07	2494.	1461.	1288.	5.067E+05	1296.	2.031E+08	2.866E+07	382.58
14648.	128.	-32.	32.	42.	41.	-14.	-52.10	163.37	14.01	-63.09	16.09	2490.	1462.	1294.	5.045E+05	1265.	2.031E+08	2.909E+07	382.18
14656.	135.	-30.	33.	51.	45.	-12.	-52.62	163.34	14.01	-63.58	16.12	2516.	1469.	1300.	5.081E+05	1272.	2.037E+08	2.932E+07	382.10
14664.	119.	-22.	32.	61.	44.	-11.	-53.14	163.31	14.01	-64.07	16.15	2527.	1484.	1293.	5.129E+05	1259.	2.037E+08	2.955E+07	381.20
14672.	126.	-4.	37.	76.	45.	-10.	-53.66	163.28	14.01	-64.56	16.18	2491.	1462.	1288.	5.157E+05	1251.	2.037E+08	2.977E+07	380.60
14680.	200.	43.	45.	91.	44.	-10.	-54.18	163.25	14.01	-65.04	16.21	2417.	1467.	1286.	5.489E+05	1323.	2.043E+08	3.004E+07	380.40
14688.	202.	-17.	34.	104.	43.	-8.	-54.70	163.21	14.01	-65.53	16.25	2328.	1496.	1284.	5.700E+05	1336.	2.049E+08	3.030E+07	380.08
14696.	192.	16.	37.	119.	42.	-8.	-55.22	163.18	14.01	-66.00	16.28	2666.	1451.	1287.	5.657E+05	1388.	2.043E+08	3.053E+07	379.58
14704.	254.	26.	36.	135.	40.	-11.	-55.74	163.15	14.01	-66.49	16.32	2353.	1514.	1269.	6.190E+05	1400.	2.037E+08	3.076E+07	379.18
14712.	249.	39.	42.	160.	36.	-11.	-56.26	163.12	14.01	-66.97	16.35	2252.	1487.	1265.	5.517E+05	1370.	2.049E+08	3.102E+07	378.60
14720.	366.	63.	36.	165.	35.	-14.	-56.77	163.09	14.01	-67.45	16.39	2160.	1536.	1275.	7.260E+05	1357.	2.049E+08	3.128E+07	378.24
14728.	337.	78.	36.	185.	31.	-14.	-57.29	163.06	14.01	-67.92	16.43	2060.	1536.	1282.	8.291E+05	1335.	2.043E+08	3.135E+07	377.70
14736.	400.	94.	35.	205.	34.	-14.	-57.81	163.03	14.01	-68.40	16.47		1534.	1284.		1314.	2.031E+08	3.136E+07	377.20
14744.	474.	103.	39.	262.	38.	-20.	-58.33	162.99	14.01	-68.87	16.52		1536.	1283.		1302.	2.031E+08	3.121E+07	376.80
14752.	524.	7.	39.	262.			-58.85	162.96	14.01	-69.34	16.56	2163.	1617.	1301.	7.372E+05	1296.	2.025E+08	3.106E+07	376.30
14760.	615.	-12.	42.	206.		-19.	-59.37	162.93	14.01	-69.80	16.61	2215.	1637.	1306.	6.513E+05	1290.	2.031E+08	3.145E+07	375.80
14768.	676.	-18.	47.	305.		-2.	-59.89	162.90	14.01	-70.27	16.66	2057.	1609.	1307.	7.671E+05	1284.	2.037E+08	3.174E+07	375.10
14776.	707.	-47.	54.	119.		-6.	-60.41	162.87	14.01	-70.73	16.71	2236.	1646.	1305.	6.354E+05	1270.	2.062E+08	3.375E+07	374.00

Table D.1(a) Archived DE2 satellite data from orbit 8025.

86

RAW DATA RETRIEVED FROM DE2 SATELLITE DATA BASE: ORBIT 8026   DAY=83015

TIME	UI	VI	WI	UN	VN	WN	LAT	LONG	LOCST	LOCHT	MAGLAT	STEMP	ITEMP	NTEMP	ELECDENS	PTEMP	O DENSITY	N2 DENSITY	ALT
19904	61	-64	37	44	-10	-27	-39.03	141.38	15.43	14.00	-54.08	2021	1433	1259	7.497E+05	1253	2.074E+08	1.970E+08	390.58
19912	59	-71	36	46	-13	-29	-39.55	141.35	15.44	14.00	-54.60	2052	1422	1265	7.335E+05	1262	2.074E+08	2.008E+08	390.28
19920	59	-70	34	46	-15	-28	-40.07	141.31	15.44	14.00	-55.12	2089	1403	1256	7.258E+05	1271	2.074E+08	2.045E+08	389.98
19928	57	-45	29	47	-16	-30	-40.59	141.28	15.45	14.00	-55.64	2116	1411	1270	7.125E+05	1267	2.074E+08	2.076E+08	389.68
19936	56	-79	26	48	-16	-34	-41.11	141.25	15.45	14.00	-56.15	2144	1425	1278	7.072E+05	1255	2.074E+08	2.106E+08	389.38
19944	55	-85	28	51	-16	-37	-41.63	141.22	15.46	14.00	-56.67	2169	1408	1267	7.009E+05	1244	2.074E+08	2.144E+08	389.08
19952	51	-87	32	49	-16	-36	-42.14	141.19	15.47	14.00	-57.19	2174	1409	1266	6.995E+05	1232	2.074E+08	2.182E+08	388.68
19960	53	-82	30	44	-16	-34	-42.66	141.15	15.47	14.00	-57.71	2203	1398	1264	6.961E+05	1220	2.080E+08	2.227E+08	388.38
19968	53	-83	14	43	-17	-32	-43.18	141.12	15.48	14.00	-58.22	2218	1404	1276	6.942E+05	1240	2.080E+08	2.273E+08	388.08
19976	52	-44	-2	46	-17	-39	-43.70	141.09	15.49	14.00	-58.74	2237	1405	1269	6.845E+05	1265	2.086E+08	2.314E+08	387.64
19984	53	-81	-7	44	-16	-52	-44.22	141.06	15.50	14.00	-59.26	2246	1414	1257	6.782E+05	1290	2.080E+08	2.356E+08	387.38
19992	54	-76	-3	43	-18	-67	-44.74	141.02	15.51	14.00	-59.77	2263	1413	1262	6.668E+05	1315	2.080E+08	2.398E+08	387.08
20000	53	-78	-1	40	-19	-65	-45.26	140.99	15.52	14.00	-60.29	2280	1408	1283	6.543E+05	1340	2.086E+08	2.439E+08	386.68
20008	51	-84	13	38	-22	-57	-45.78	140.96	15.53	14.00	-60.81	2319	1433	1310	6.423E+05	1308	2.093E+08	2.465E+08	386.38
20016	50	-81	28	33	-24	-39	-46.30	140.93	15.54	14.00	-61.32	2338	1421	1296	6.317E+05	1275	2.099E+08	2.530E+08	385.98
20024	51	-84	40	35	-27	-30	-46.82	140.90	15.55	14.00	-61.84	2356	1427	1296	6.171E+05	1242	2.105E+08	2.591E+08	385.58
20032	58	-82	47	42	-29	-27	-47.33	140.86	15.56	14.00	-62.36	2376	1419	1285	6.079E+05	1209	2.111E+08	2.652E+08	385.28
20040	67	-97	51	45	-30	-31	-47.85	140.83	15.57	14.00	-62.87	2404	1448	1269	5.984E+05	1190	2.111E+08	2.716E+08	384.98
20048	71	-99	52	57	-29	-30	-48.37	140.80	15.58	14.00	-63.39	2427	1432	1288	5.912E+05	1211	2.117E+08	2.780E+08	384.48
20056	83	-86	50	64	-27	-12	-48.89	140.77	15.59	14.00	-63.91	2436	1450	1297	5.836E+05	1233	2.123E+08	2.848E+08	384.08
20064	108	-84	54	81	-26	-13	-49.41	140.74	15.60	14.00	-64.42	2434	1482	1301	5.775E+05	1255	2.130E+08	2.917E+08	383.68
20072	135	-83	55	98	-24	-13	-49.93	140.70	15.61	14.00	-64.94	2425	1478	1304	5.713E+05	1277	2.136E+08	2.982E+08	383.38
20080	167	-70	55	122	-20	-16	-50.45	140.67	15.63	14.00	-65.45	2425	1453	1302	5.716E+05	1292	2.142E+08	3.068E+08	382.98
20088	210	-61	51	151	-16	-15	-50.97	140.64	15.64	14.00	-65.97	2401	1462	1306	5.702E+05	1302	2.148E+08	3.235E+08	382.58
20096	206	-61	52	101	-13	-18	-51.49	140.61	15.65	14.00	-66.48	2395	1466	1308	5.718E+05	1311	2.154E+08	3.402E+08	382.28
20104	300	-71	55	218	-9	-19	-52.01	140.58	15.67	14.00	-67.00	2430	1479	1309	5.540E+05	1321	2.160E+08	3.720E+08	382.08
20112	351	57	55	262	-11	-17	-52.53	140.55	15.68	14.00	-67.52	2415	1483	1301	5.715E+05	1330	2.160E+08	4.030E+08	381.64
20120		0	0	311	-13	-9	-53.04	140.51	15.70	14.00	-68.03	2421	1558	1294	5.803E+05	1328	2.173E+08	4.261E+08	381.28
20128				353	-14	-16	-53.56	140.48	15.71	14.00	-68.55	2269	1632	1286	5.792E+05	1321	2.185E+08	4.405E+08	381.00
20136	618	104	62	383	-16	-9	-54.08	140.45	15.73	14.01	-69.06	2259	1707	1285	7.296E+05	1315	2.204E+08	4.697E+08	380.68
20144	605	312	59	410	-0	-2	-54.60	140.42	15.75	14.01	-69.57	2371	1556	1275	6.473E+05	1308	2.222E+08	4.909E+08	380.08
20152	640	230	58	430	0	3	-55.12	140.39	15.77	14.01	-70.09	2328	1605	1257	6.502E+05	1302	2.228E+08	5.060E+08	379.54
20160	716	278	54	436	16	1	-55.64	140.36	15.78	14.01	-70.60	2484	1611	1236	6.283E+05	1314	2.235E+08	5.227E+08	379.18
20168	832	209	47	430	22	-0	-56.16	140.32	15.80	14.01	-71.11	2586	1664	1216	4.763E+05	1326	2.222E+08	5.261E+08	378.68
20176	761	192	39	421	20	-17	-56.68	140.29	15.83	14.01	-71.63	2660	1622	1197	5.171E+05	1338	2.210E+08	5.295E+08	378.28
20184	632	159	36	419	18	-21	-57.20	140.26	15.85	14.01	-72.14	2550	1585	1195	5.299E+05	1350	2.210E+08	5.348E+08	377.78
20192	653	179	35	434	-16	-20	-57.72	140.23	15.87	14.01	-72.65	2667	1651	1232	5.693E+05	1362	2.210E+08	5.402E+08	377.38
20200	759	158	25	447	17	-19	-58.24	140.20	15.90	14.01	-73.16	2652	1606	1275	5.448E+05	1373	2.204E+08	5.580E+08	377.00
20208	834	76	21	431	15	-18	-58.76	140.17	15.92	14.01	-73.67	2803	1606	1385	5.138E+05	1385	2.198E+08	5.758E+08	376.38
20216	814	0	21	161	20	-18	-59.28	140.14	15.95	14.01	-74.18	3079	1676	1397	6.003E+05	1397	2.185E+08	5.917E+08	375.98
20224	817	-76	42			-16	-59.80	140.11	15.98	14.01	-74.69	3693	1984	1408	5.912E+05	1408	2.173E+08	6.076E+08	375.48
20232	237	-23	42	161	20	-13	-60.32	140.08	16.04	14.01	-75.28	3693	1984	1466	5.912E+05	1466	2.136E+08	6.205E+08	374.98

Table D.1(b) Archived DE2 satellite data from orbit 8026

87

RAW DATA RETRIEVED FROM DE2 SATELLITE DATA BASE: ORBIT 8027   DAY=83015

TIME	UI	VI	WI	UN	VN	WN	LAT	LONG	LOCST	MAGLAT	LOCHT	ETEMP	ITEMP	NTEMP	STEMP	ELECDEN	PTEMP	DENSITY O	DENSITY N2	ALT
25360.	75.	11.	44.	66.	-2.	-18.	-39.46	118.55	14.00	-55.00	15.04	1518.	1516.	1954.	1255.	7.696E+05	1241.	2.099E+08	2.220E+07	309.78
25376.	61.	15.	45.	68.	-14.	-19.	-39.97	118.52	14.00	-55.60	15.04	1486.	1466.	1954.	1257.	7.836E+05	1245.	2.099E+08	2.250E+07	309.70
25384.	84.	45.	45.	67.	-20.	-16.	-40.49	118.49	14.00	-56.12	15.03	1547.	1547.	1986.	1257.	7.707E+05	1246.	2.105E+08	2.280E+07	309.40
25392.	85.	47.	47.	65.	-16.	-16.	-41.01	118.46	14.00	-56.63	15.03	1562.	1526.	2027.	1268.	7.632E+05	1265.	2.111E+08	2.326E+07	309.10
25400.	81.	46.	46.	67.	-9.	-17.	-41.53	118.42	14.00	-57.15	15.03	1586.	1562.	2059.	1271.	7.528E+05	1284.	2.111E+08	2.375E+07	308.80
25408.	79.	-18.	45.	70.	-3.	-17.	-42.05	118.39	14.00	-57.66	15.02	2027.	1959.	2096.	1271.	7.498E+05	1303.	2.117E+08	2.424E+07	308.50
25416.	81.	-20.	45.	74.	6.	-18.	-42.57	118.36	14.00	-58.18	15.02	2096.	2113.	2113.	1274.	7.401E+05	1321.	2.123E+08	2.481E+07	308.28
25424.	81.	-16.	45.	75.	5.	-18.	-43.09	118.33	14.00	-58.70	15.01	2135.	2139.	2139.	1274.	7.346E+05	1336.	2.123E+08	2.536E+07	308.00
25432.	83.	-20.	43.	74.	5.	-19.	-43.61	118.30	14.00	-59.21	15.01	2159.	2159.	2159.	1268.	7.231E+05	1343.	2.130E+08	2.595E+07	307.58
25440.	85.	-19.	42.	75.	4.	-23.	-44.13	118.26	14.00	-59.73	15.00	2185.	2185.	2185.	1277.	7.190E+05	1348.	2.136E+08	2.652E+07	307.50
25448.	87.	-20.	42.	79.	4.	-27.	-44.64	118.23	14.00	-60.24	14.99	2208.	2208.	2208.	1294.	7.150E+05	1353.	2.142E+08	2.720E+07	307.20
25456.	89.	-24.	43.	79.	7.	-27.	-45.16	118.20	14.00	-60.76	14.99	2234.	2234.	2234.	1280.	7.024E+05	1356.	2.148E+08	2.788E+07	306.60
25464.	93.	-23.	46.	79.	11.	-28.	-45.68	118.17	14.00	-61.27	14.98	2273.	2273.	2273.	1283.	6.927E+05	1361.	2.154E+08	2.883E+07	306.50
25472.	95.	-25.	45.	80.	15.	-28.	-46.20	118.14	14.00	-61.79	14.97	2284.	2284.	2284.	1297.	6.871E+05	1362.	2.160E+08	2.977E+07	306.10
25480.	98.	-26.	47.	81.	19.	-26.	-46.72	118.10	14.00	-62.31	14.97	2297.	2297.	2297.	1302.	6.795E+05	1363.	2.73E+08	3.140E+07	305.80
25488.	104.	-25.	47.	86.	23.	-29.	-47.24	118.07	14.00	-62.82	14.96	2315.	2315.	2315.	1314.	6.647E+05	1364.	2.105E+08	3.303E+07	305.60
25496.	113.	-26.	46.	89.	29.	-31.	-47.76	118.04	14.00	-63.34	14.96	2325.	2325.	2325.	1316.	6.564E+05	1365.	2.204E+08	3.640E+07	305.00
25504.	121.	-24.	48.	91.	34.	-30.	-48.28	118.01	14.00	-63.85	14.96	2339.	2339.	2339.	1316.	6.458E+05	1374.	2.160E+08	3.977E+07	304.70
25512.	127.	-22.	45.	95.	39.	-30.	-48.80	117.98	14.00	-64.37	14.95	2351.	2351.	2325.	1325.	6.309E+05	1388.	2.222E+08	4.144E+07	304.38
25520.	136.	-14.	39.	105.	40.	-33.	-49.32	117.94	14.00	-64.88	14.94	2366.	2366.	2339.	1328.	6.275E+05	1402.	2.222E+08	4.311E+07	303.90
25528.	157.	-20.	39.	120.	45.	-36.	-49.84	117.91	14.00	-65.40	14.93	2394.	2394.	2351.	1325.	6.159E+05	1417.	2.216E+08	4.405E+07	303.50
25536.	202.	1.	39.	140.	50.	-35.	-50.35	117.88	14.00	-65.92	14.93	2391.	2391.	2366.	1333.	6.099E+05	1431.	2.210E+08	4.500E+07	383.18
25544.	265.	13.	38.	167.	54.	-37.	-50.87	117.85	14.00	-66.43	14.92	2382.	2382.	2394.	1331.	5.949E+05	1463.	2.199E+08	4.560E+07	382.70
25552.	371.	16.	30.	203.	59.	-54.	-51.39	117.82	14.00	-66.95	14.91	2354.	2354.	2391.	1333.	5.848E+05	1497.	2.185E+08	4.636E+07	382.48
25560.	404.	41.	34.	248.	66.	-57.	-51.91	117.79	14.00	-67.46	14.91	2359.	2359.	2382.	1335.	5.827E+05	1531.	2.160E+08	4.667E+07	381.90
25568.	505.	83.	29.	300.	59.	-48.	-52.43	117.75	14.00	-67.98	14.90	2398.	2398.	2354.	1339.	5.816E+05	1565.	2.136E+08	4.697E+07	381.58
25576.	639.	118.	24.	363.	52.	-52.	-52.95	117.72	14.00	-68.49	14.89	2359.	2359.	2359.	1351.	5.798E+05	1589.	2.099E+08	4.708E+07	381.10
25584.	754.	143.	22.	430.	45.	-4.	-53.47	117.69	14.00	-69.01	14.88	2207.	2207.	2398.	1357.	5.647E+05	1546.	2.062E+08	4.720E+07	380.70
25592.	847.	154.	12.	497.	38.	20.	-53.99	117.66	14.00	-69.52	14.87	2364.	2364.	2359.	1367.	5.909E+05	1503.	2.012E+08	4.739E+07	380.30
25600.	976.	-1.	-1.	566.	46.	43.	-54.51	117.63	14.00	-70.04	14.85	2435.	2435.	2207.	1357.	5.665E+05	1459.	1.963E+08	4.758E+07	379.90
25608.	1077.	193.	-20.	626.	54.	51.	-55.03	117.60	14.00	-70.55	14.85	2685.	2685.	2364.	1336.	6.374E+05	1416.	1.938E+08	4.807E+07	379.44
25616.	1223.	193.	-39.	666.	61.	12.	-55.55	117.56	14.00	-71.07	14.82	2793.	2793.	2435.	1335.	5.918E+05	1402.	1.914E+08	4.856E+07	379.00
25624.	1277.	241.	-38.	674.	69.	6.	-56.07	117.53	14.00	-71.58	14.81	3614.	3614.	2685.	1341.	5.848E+05	1417.	1.895E+08	4.932E+07	378.50
25632.	1288.	177.	-27.	657.	56.	44.	-56.59	117.50	14.00	-72.10	14.79	4330.	4330.	2793.	1366.	6.026E+05	1432.	1.928E+08	5.008E+07	378.10
25640.	857.	87.	-18.	624.	20.	37.	-57.11	117.47	14.00	-72.61	14.78	4090.	4090.	3614.	1391.	5.731E+05	1440.	1.938E+08	5.167E+07	377.70
25648.	643.	-18.	43.	573.	43.		-57.63	117.44	14.00	-73.12	14.76	3633.	3633.	4330.	1424.	6.567E+05	1463.	1.944E+08	5.326E+07	377.20
25656.	-257.	-59.	76.	476.	51.		-58.15	117.41	14.00	-73.64	14.74	3500.	3500.	4090.	1505.	7.717E+05	1460.	1.951E+08	5.507E+07	376.78
25664.	-694.	-43.	127.	332.	12.		-58.67	117.38	14.00	-74.15	14.73	3972.	3972.	3633.	1534.	5.778E+05	1451.	1.895E+08	5.846E+07	376.38
25672.	-057.	76.	132.	183.	6.		-59.19	117.35	14.00	-74.67	14.71	3207.	2404.	3500.	1533.	4.751E+05	1442.	1.772E+08	6.125E+07	375.80
25680.	-1084.	-279.	98.	46.	44.		-59.70	117.31	14.00	-75.17	14.67		2021.	3972.	1540.	4.365E+05	1434.	1.704E+08	6.402E+07	375.30
25688.	-1239.	-305.	40.	-6.	37.		-60.22	117.28	14.00	-75.69	14.64		2919.	3207.	1625.	2.809E+05	1625.	1.667E+08	6.701E+07	374.90

Table D.1(c)   Archived DE2 satellite data from orbit 8027
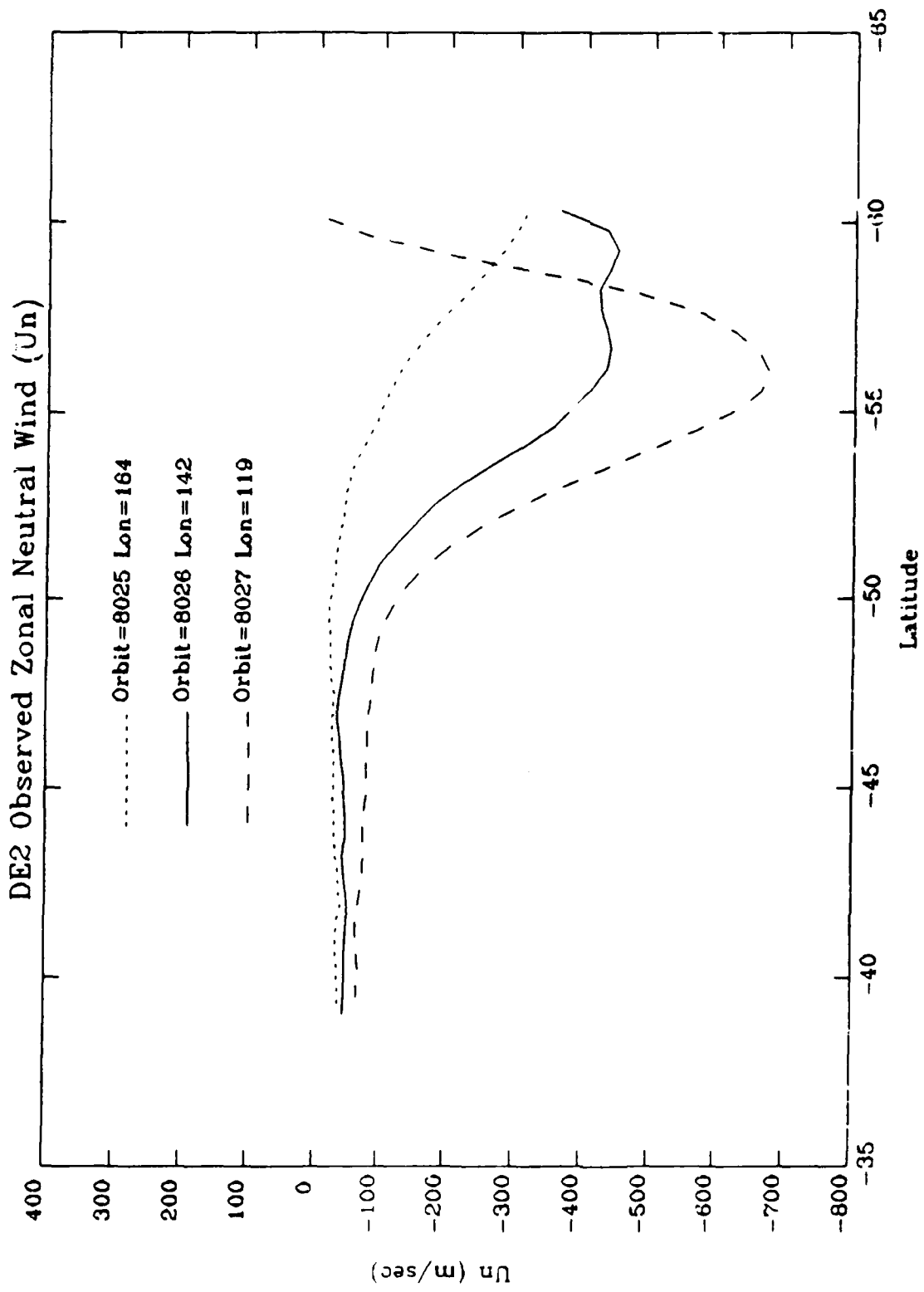
Figure D.1 Satellite-measured zonal neutral wind component

DE2 Observed Meridional Neutral Wind (Vn)
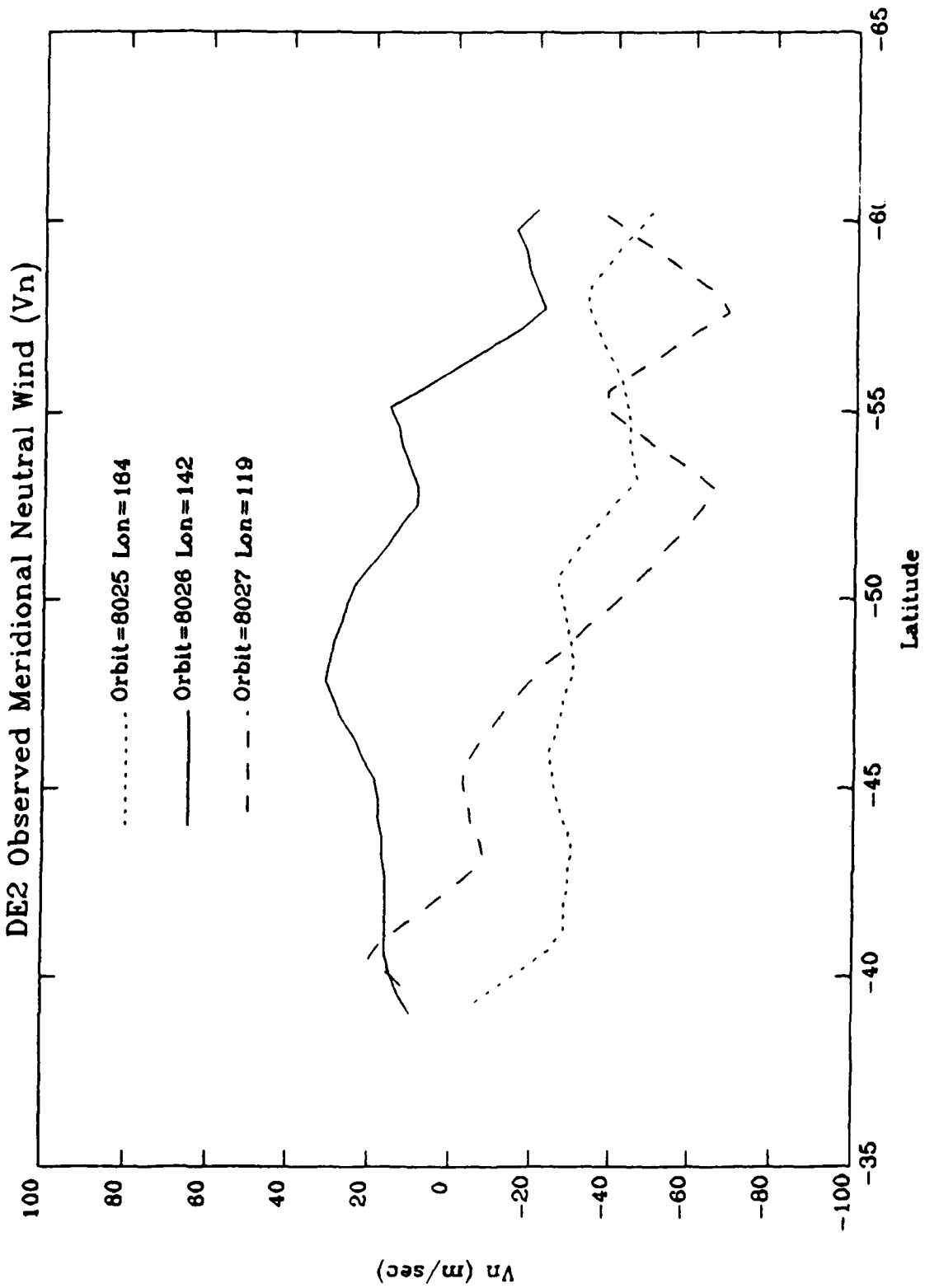
Figure D.2 Satellite-measured meridional wind component

DE2 Observed Meridional Ion Wind (Vi)
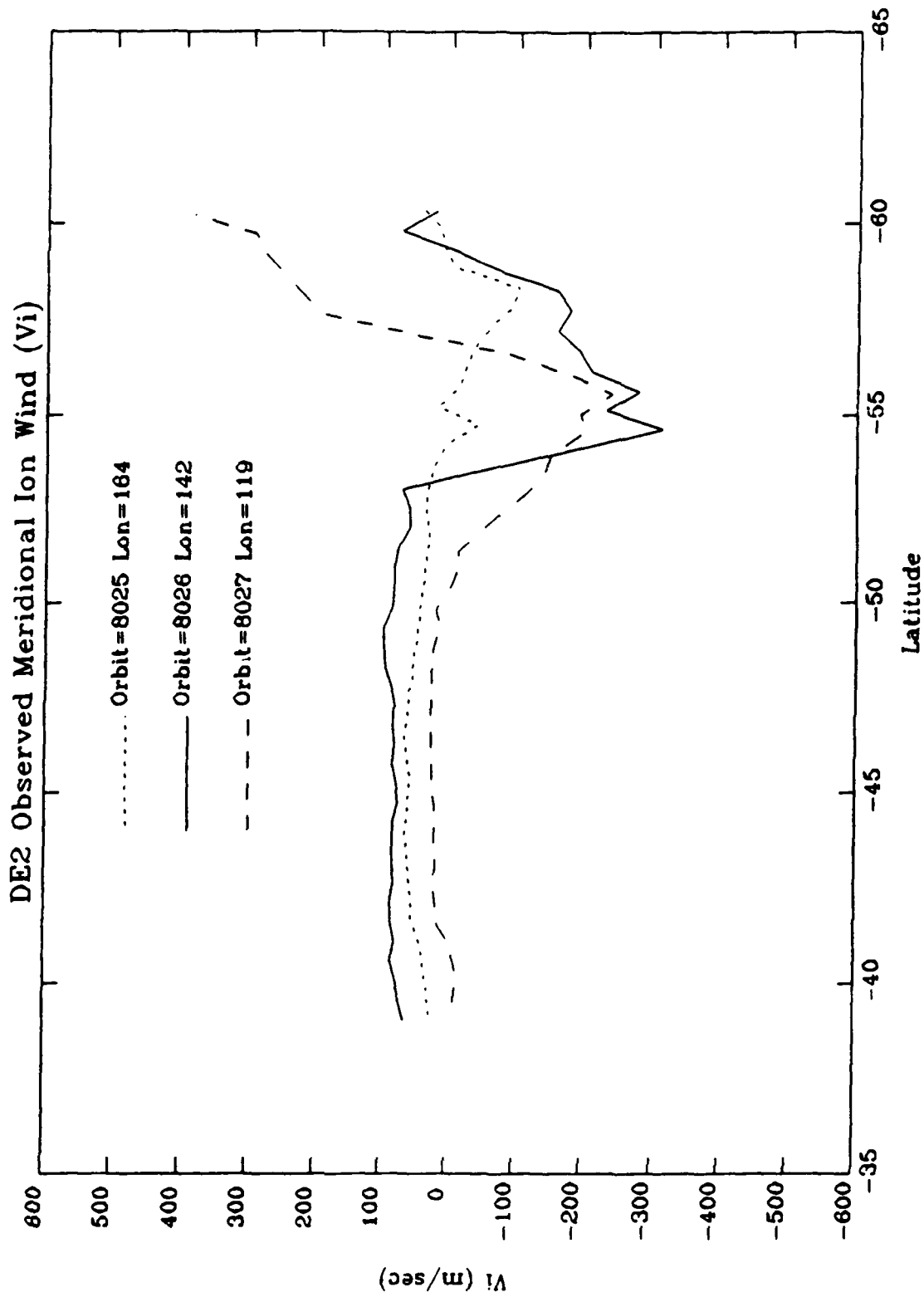
Figure D.3 Satellite-measured meridional ion drift velocities

91
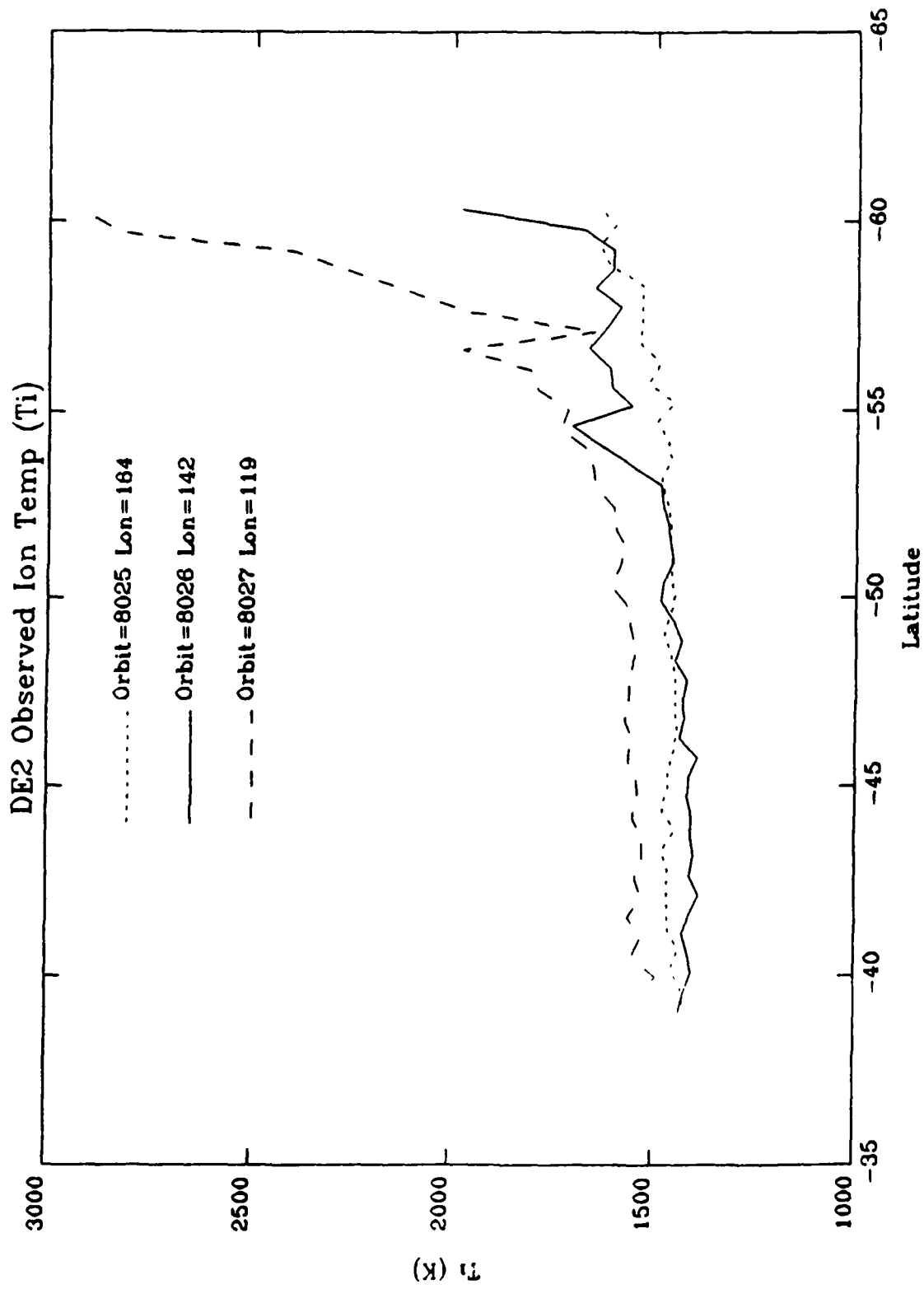
Figure D.4 Satellite-measured ion temperature
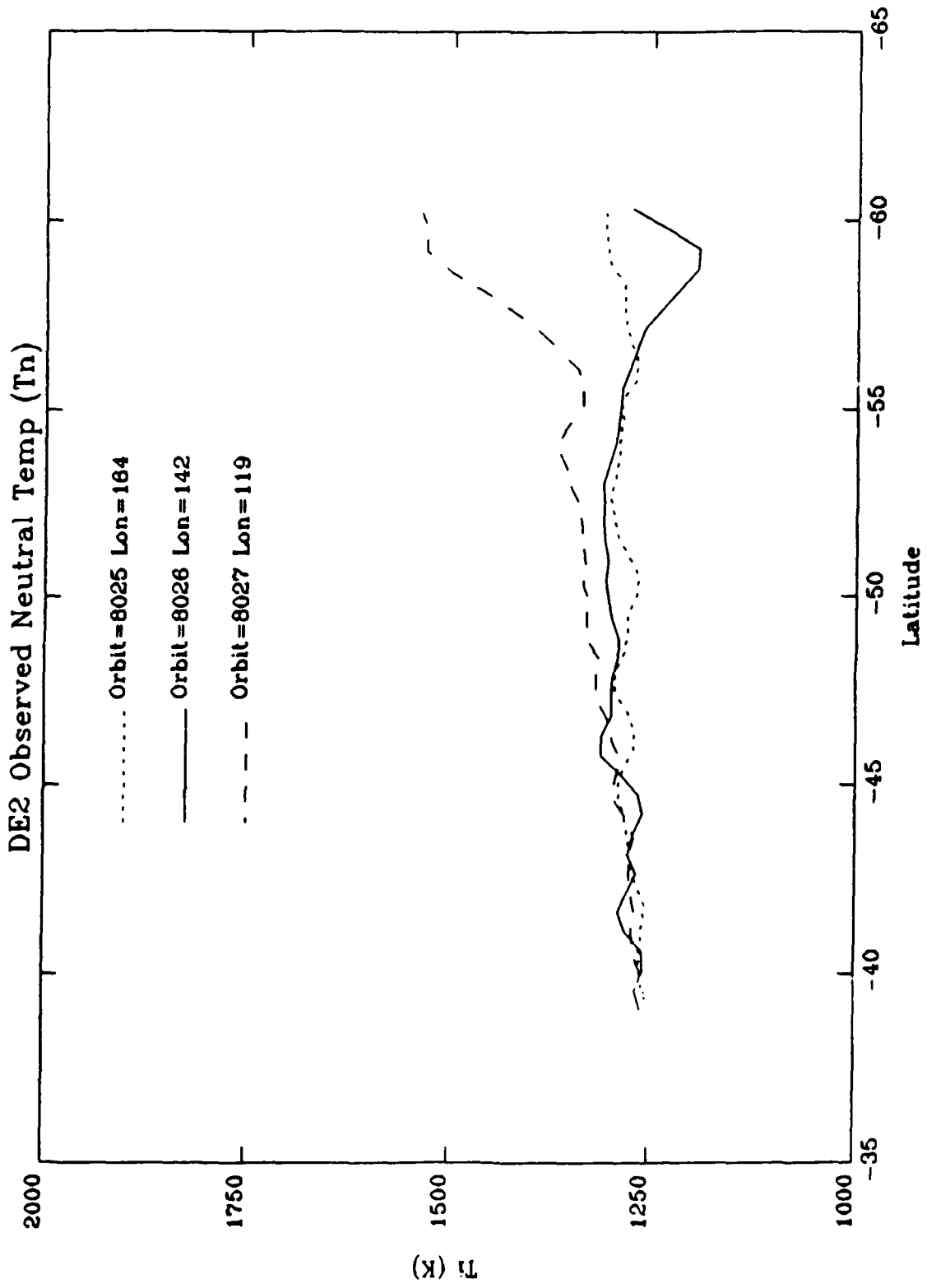
Figure D.5 Satellite-measured neutral temperature
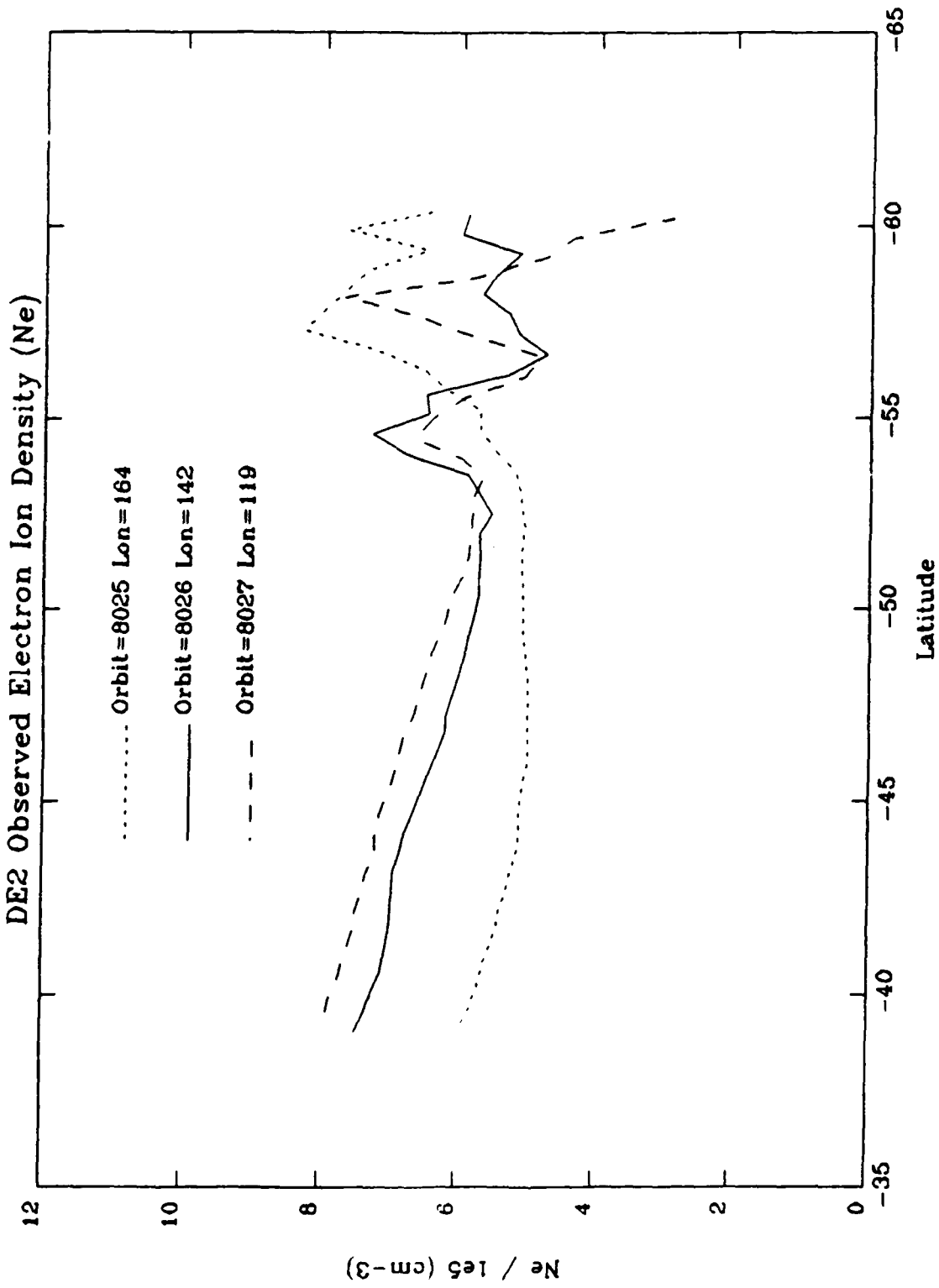
Figure D.6 Satellite-measured ion density
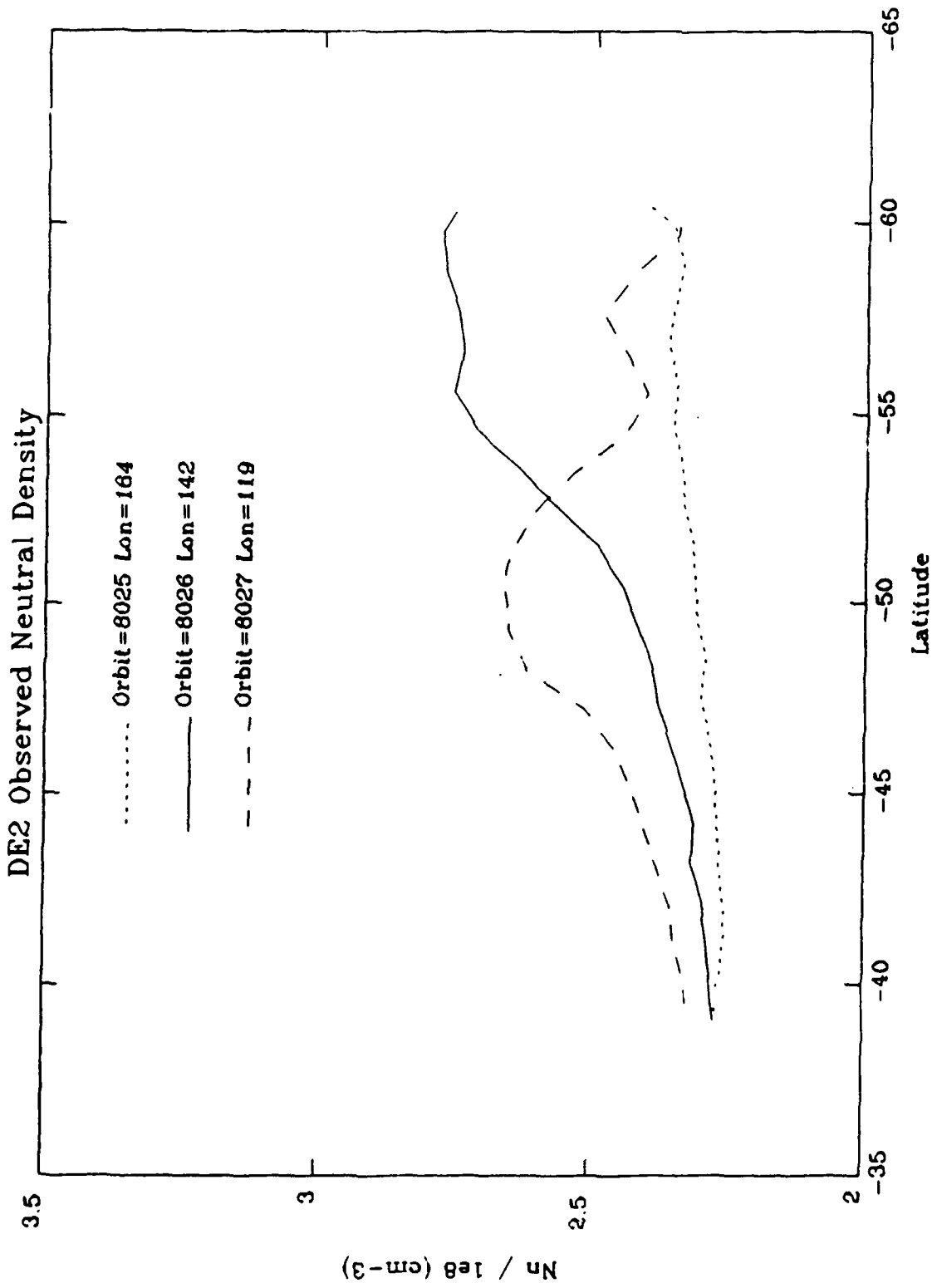
Figure D.7 Satellite-measured neutral density (O + N$_2$)

References

Banks, P. M., and G. Kockarts, *Aeronomy*, New York, 1973

Dickinson, R. I., E. C. Ridley, A three-dimensional general circulation model of the atmosphere, *J. Geophys. Res., 86,* 1499-1512, 1981

Greenberg, L. H., *Discoveries in Physics for Scientists and Engineers*, W. B. Saunders Co, Toronto, 1975

Holton, J. R., *An Introduction to Dynamic Meteorology,* Academic Press, New York

Killeen, T. L., R. G Roble, An analysis of the high-latitude thermospheric wind pattern calculated by a thermospheric general circulation model , *J. Geophys. Res., 89,* 7509-7522, 1984

Killeen, T. L., R. G. Roble, N. W. Spencer, A computer model of global thermospheric winds and temperatures, *Adv. Space Res*, 7 ,(10)207-(10)215, 1987